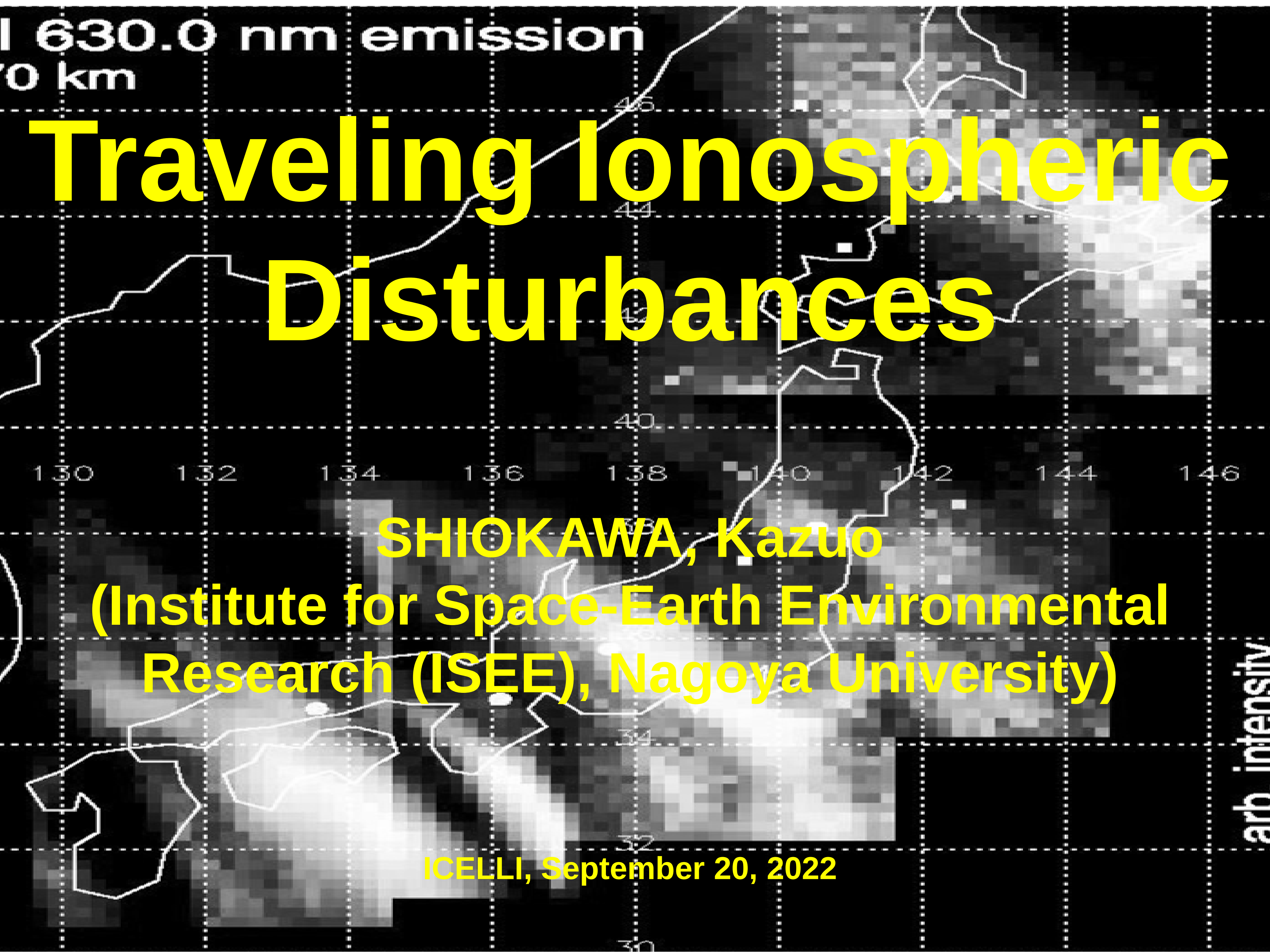

Traveling Ionospheric Disturbances

SHIOKAWA, Kazuo
(Institute for Space-Earth Environmental Research (ISEE), Nagoya University)

ICELLI, September 20, 2022

Categories of traveling ionospheric disturbances

large, medium, small

TABLE 1. Properties of Atmospheric Gravity Waves as Manifested by TID's

Nomenclature	Horizontal Velocity, m/s	Period	Wavelength	Possible Sources	Remarks
'Large scale'	400–1000	30 min to 3 hours	≲1000 km	'Polar regions . . . during geomagnetic storms' [*Francis*, 1975]	Propagate equatorward
'Medium scale'	1000–250	15 min to ≃1 hour	'several hundred km . . .'	'auroral sources are felt to play an important role' [*Francis*, 1975]	Their dominant propagation direction is from the 'winter polar regions'
'Small scale'	≃300–3000*	peak at 3.5 and 4.5 min (2–5 min)		'severe convective activity [*Georges*, 1973]	Seasonal occurrence peak in the summer

*Note that the lower atmospheric sound speed is ≃300 m/s.

Hunsucker (Rev. Geophys., p293, 1982)

Source of traveling ionospheric disturbances

- **Gravity waves from the lower atmosphere**
  - tropospheric convection
  - jet wind streak (stratosphere/mesosphere)
  - typhoon, earthquake/tsunami, volcanic eruption
  - secondary gravity waves by gravity wave dissipation

- **Gravity waves from auroral energy input**
  - Joule heating
  - Lorentz force

- **Ionospheric instabilities**
  - Perkins instability
  - E-F coupling instability

Source of traveling ionospheric disturbances

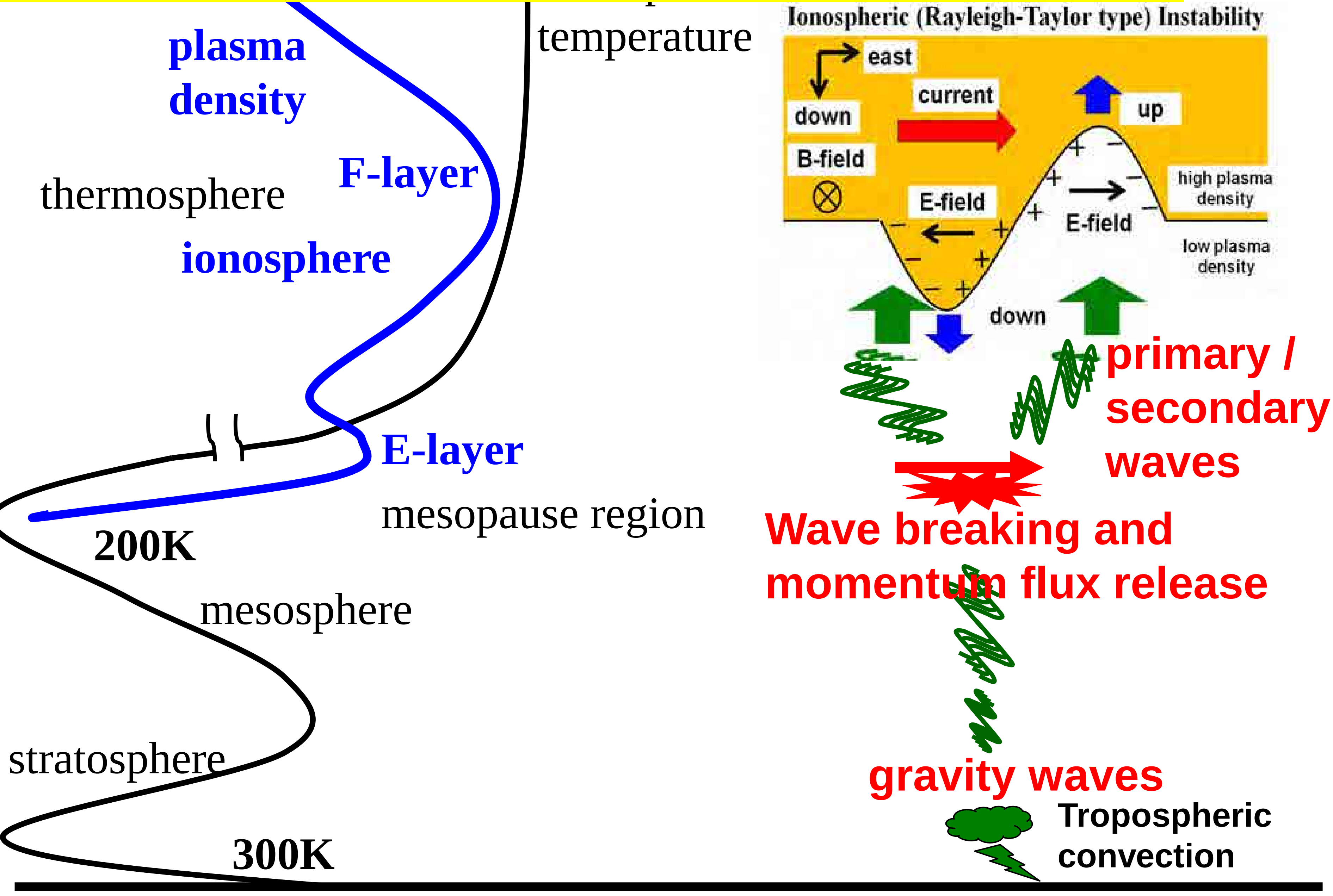

Oberheide et al. (PEPS, 2015)

Source of traveling ionospheric disturbances

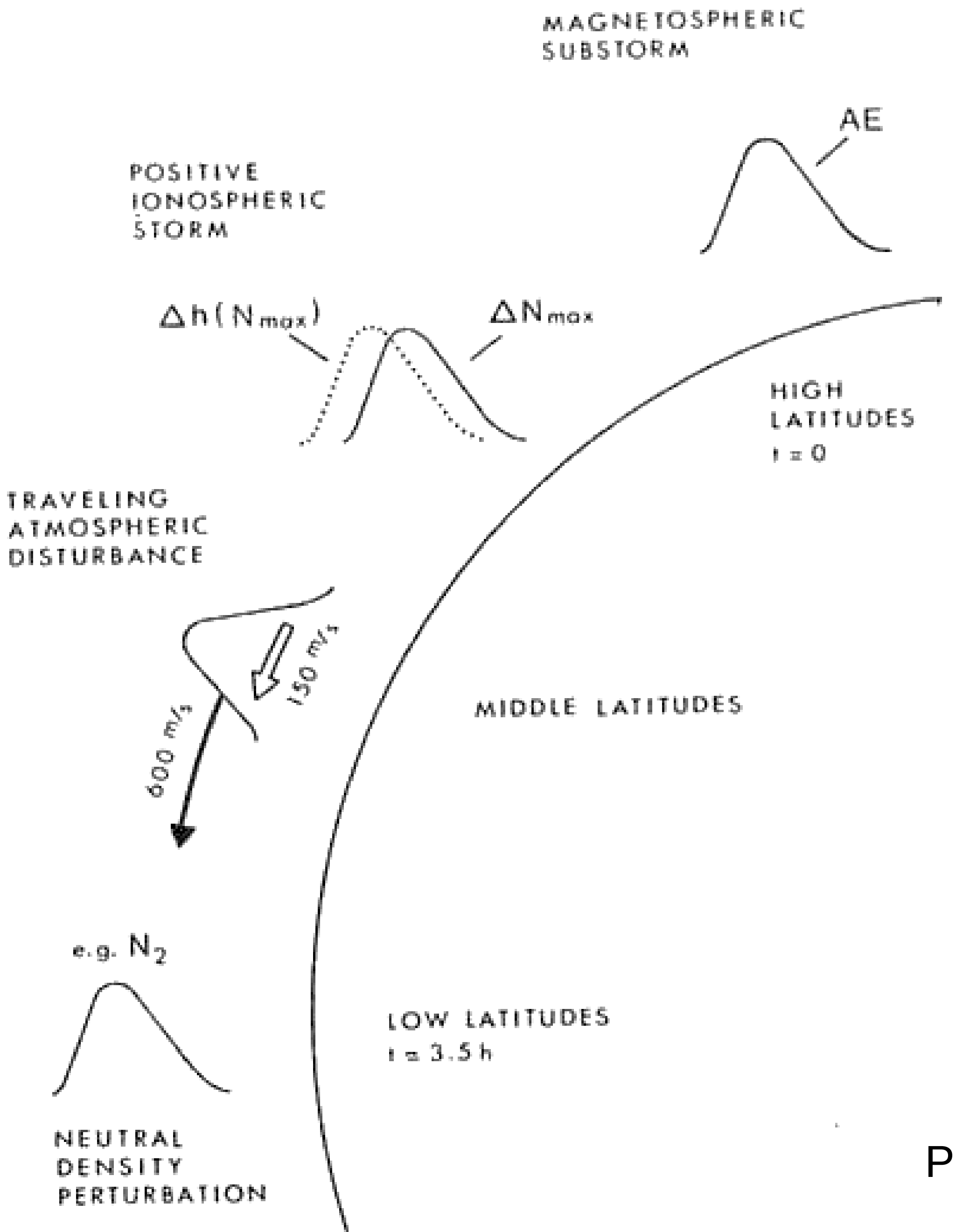

Prolss [JGR, 1993]

atmospheric waves from below

ionosphere

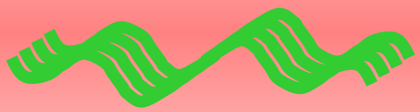

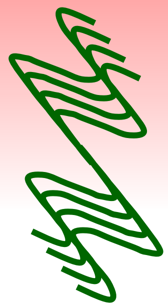

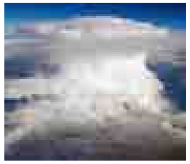

sound waves: **period <5 min**

compressional, local

gravity waves (regional): **5min - several hours**

shear type, regional

tides (global): **6 hours – 1 day**

shear type, global (earth size, resonance)

planetary waves (global): **a few days – 16 days**

shear type, global, Corioli’s force

Sound waves and gravity waves

Dynamic variation of the ionosphere associated with Tohoku Earthquake/Tsunami

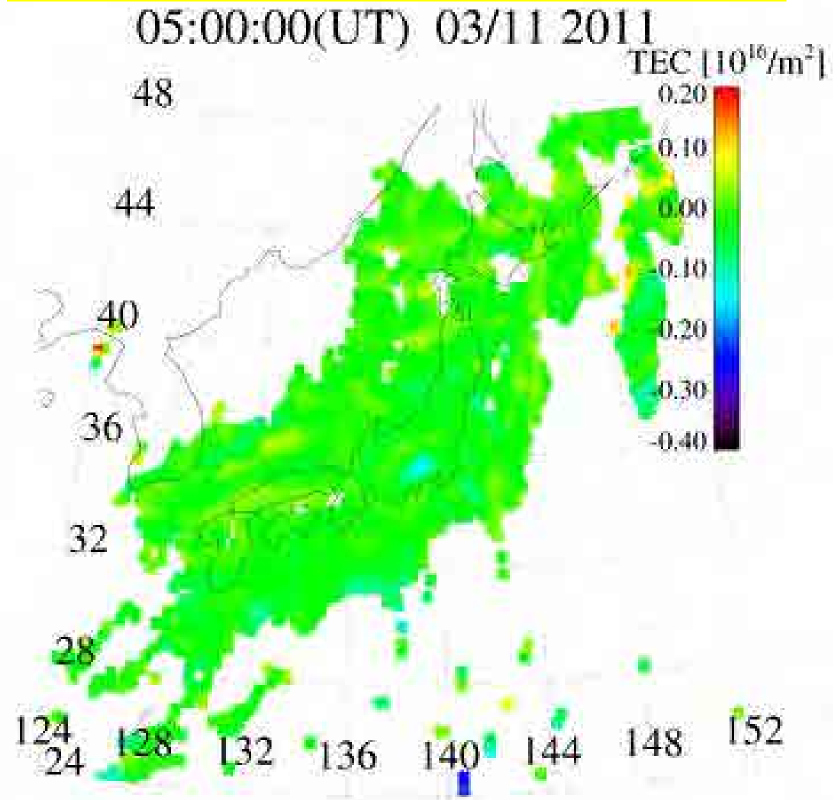

Tsugawa et al. (EPS, 2011)

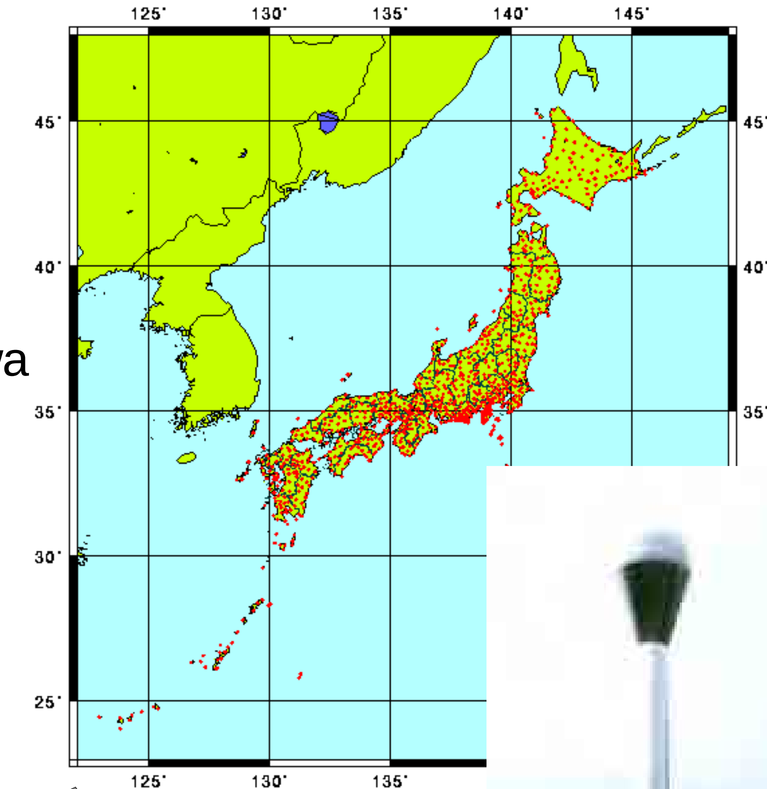

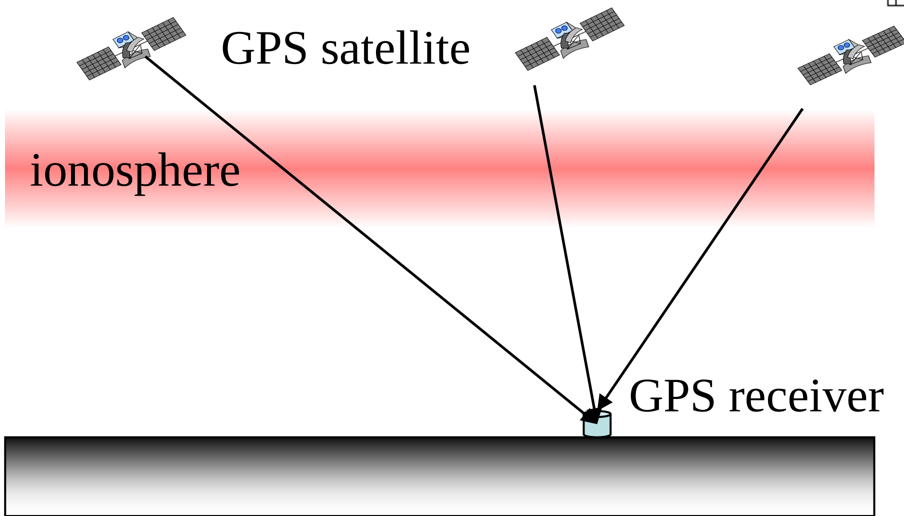

TEC perturbation after the Tonga volcanic eruption

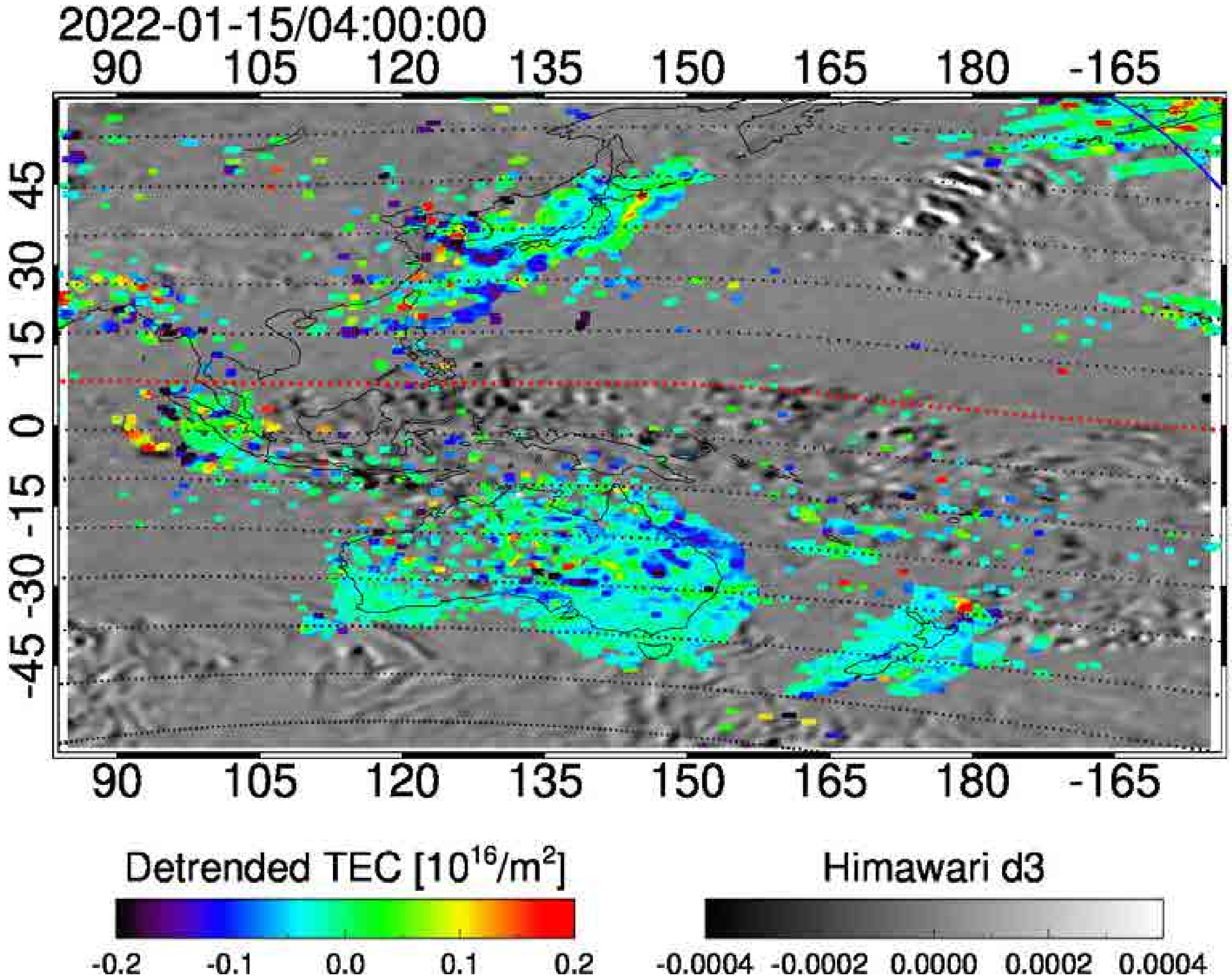

[Shinbori et al., Earth Planets and Space, 2022]

TEC perturbation after the Tonga volcanic eruption

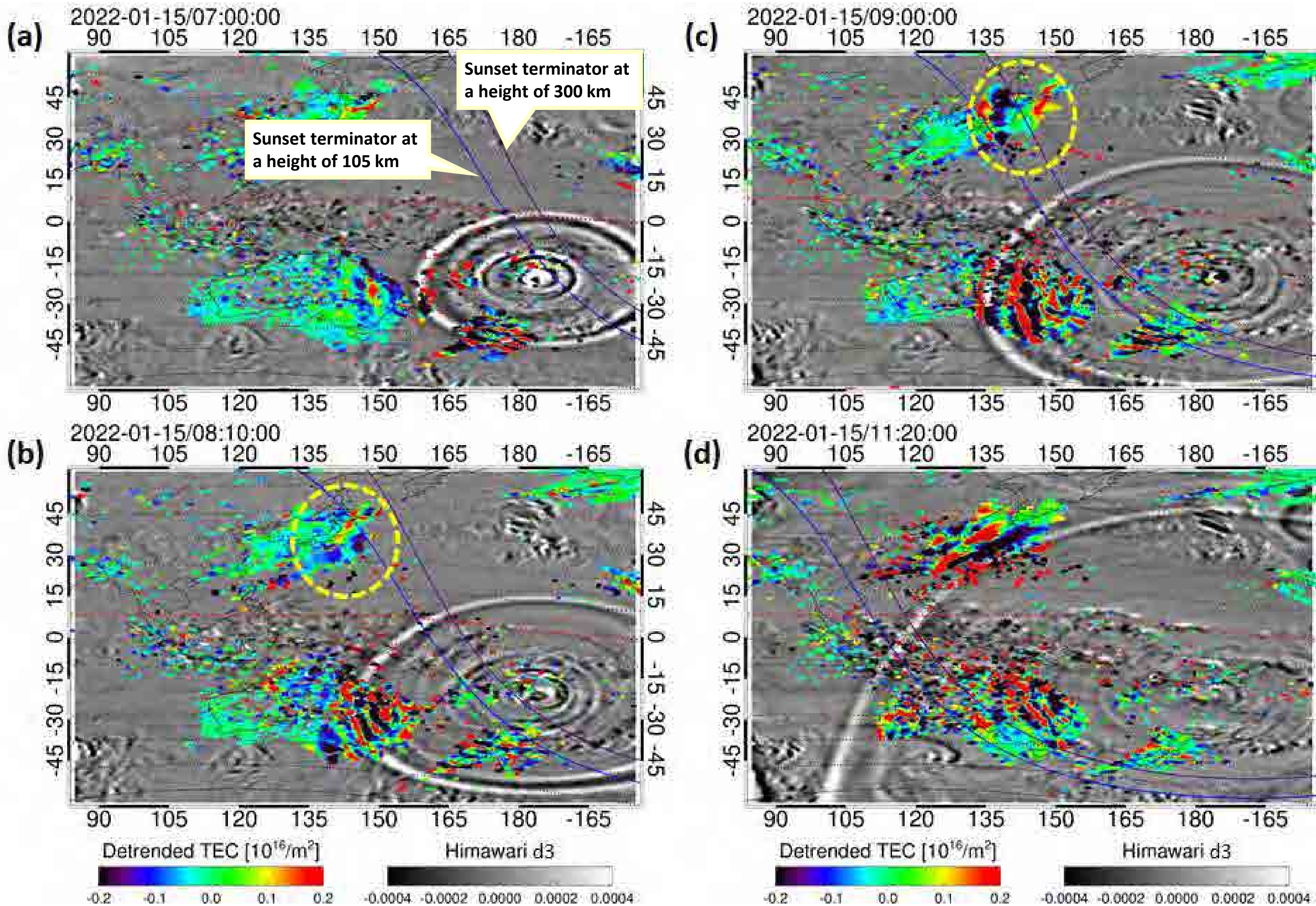

[Shinbori et al., Earth Planets and Space, 2022]

Scenario of TEC and electric field perturbations in the ionosphere triggered by the Tonga volcanic eruption

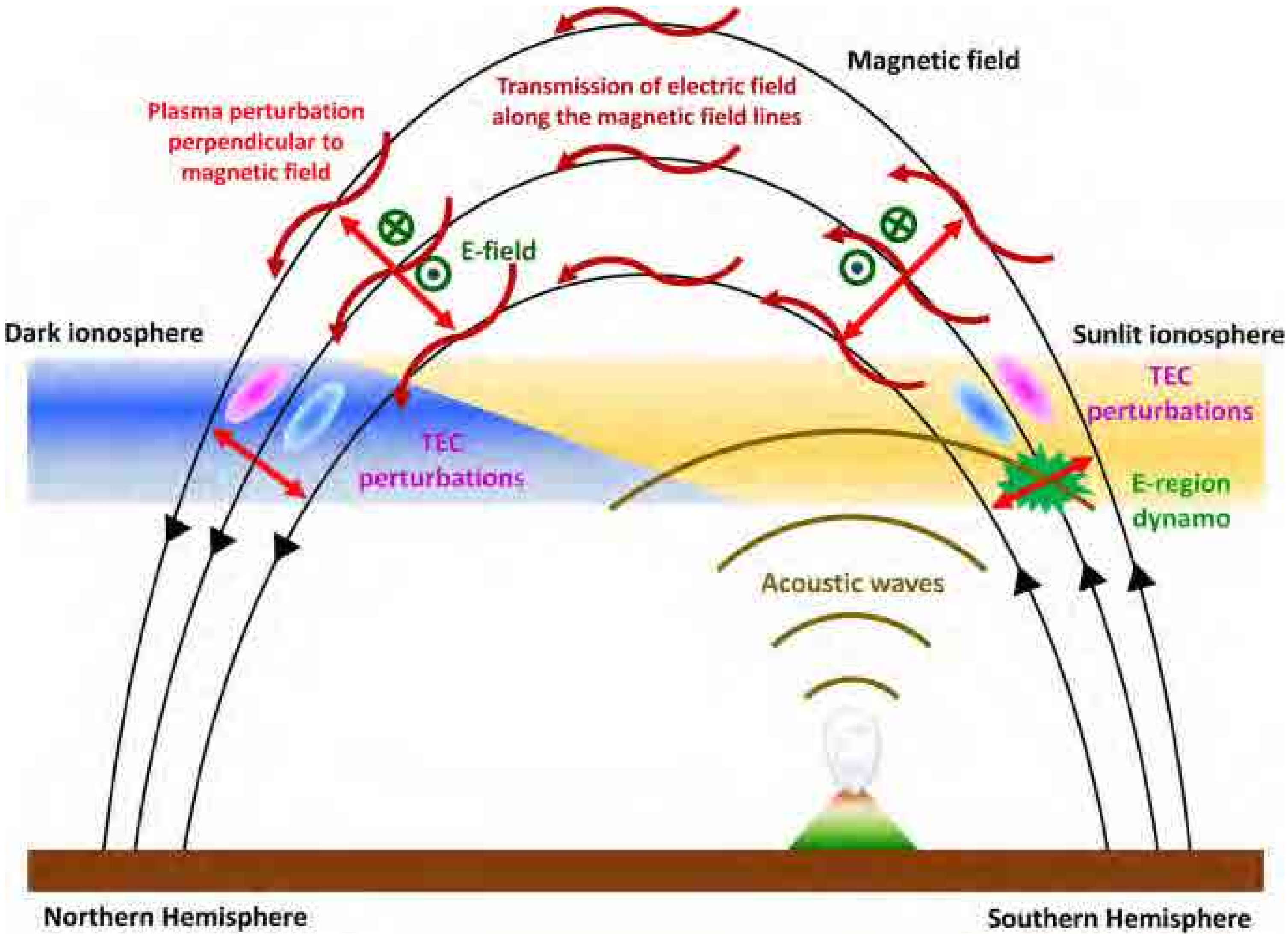

[Shinbori et al., Earth Planets and Space, 2022]

Large-scale traveling ionospheric disturbances (LSTIDs)

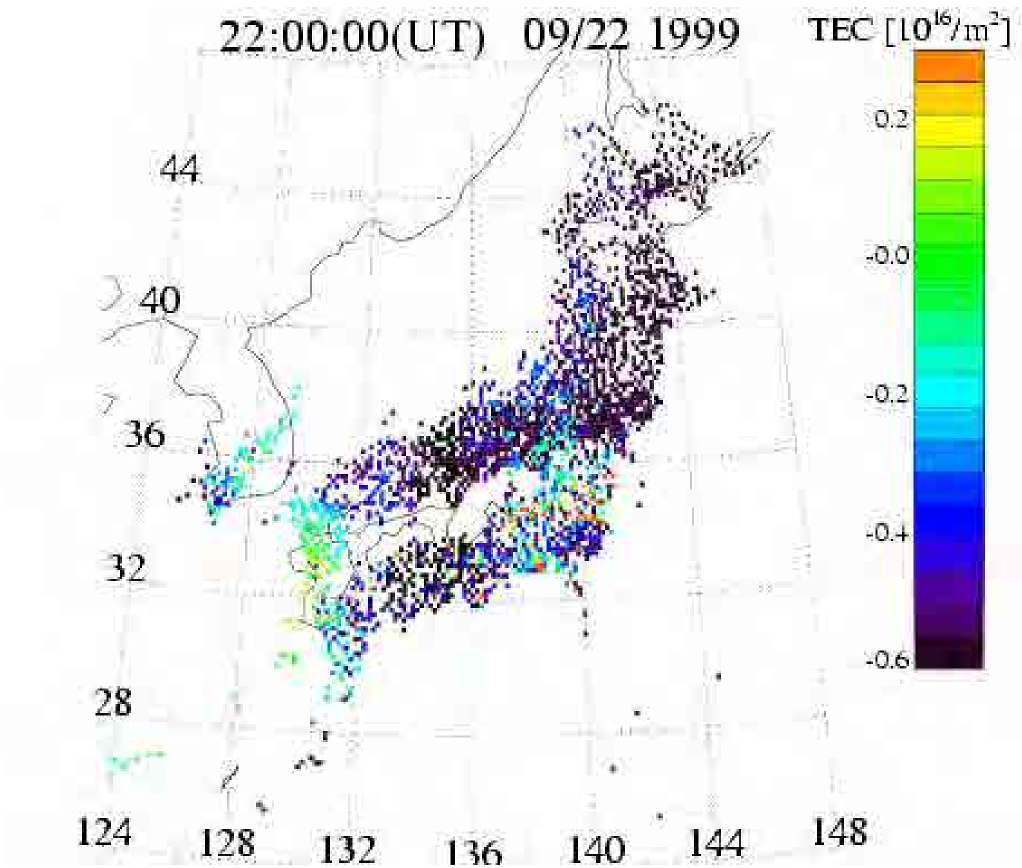
22:00:00(UT) 09/22 1999
TEC [10^16/m^2]
0.2
-0.0
-0.2
-0.4
-0.6
44
40
36
32
28
124
128
132
136
140
144
148

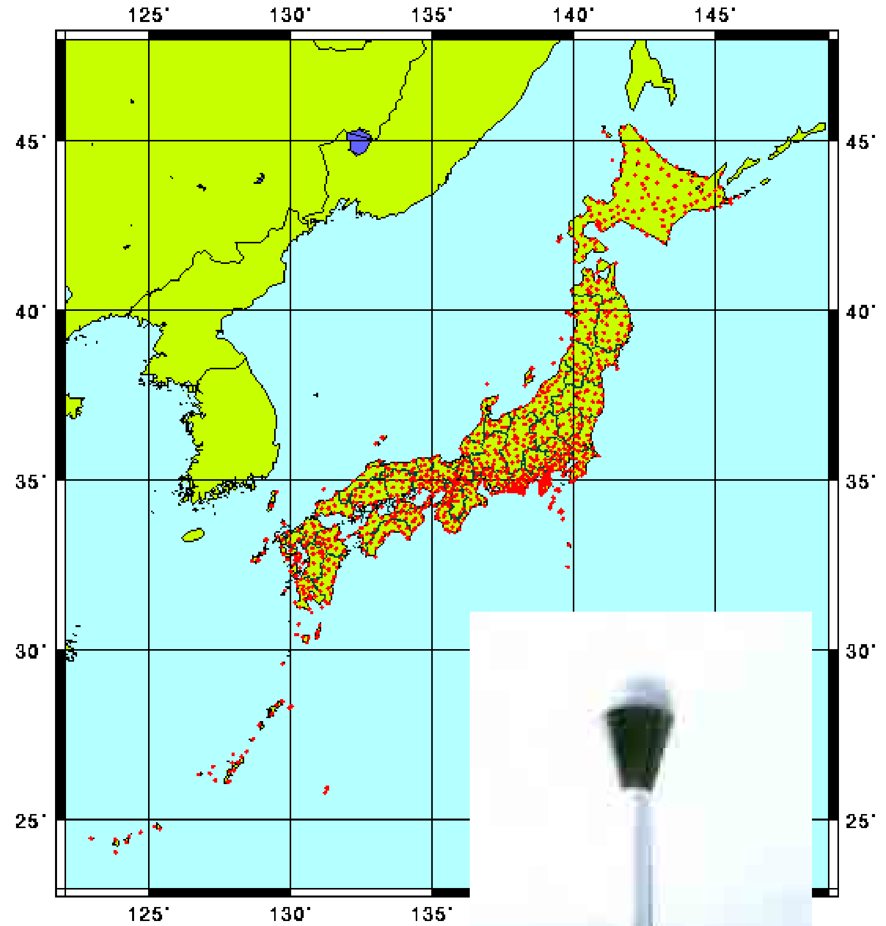
125°
130°
135°
140°
145°
45°
40°
35°
30°
25°

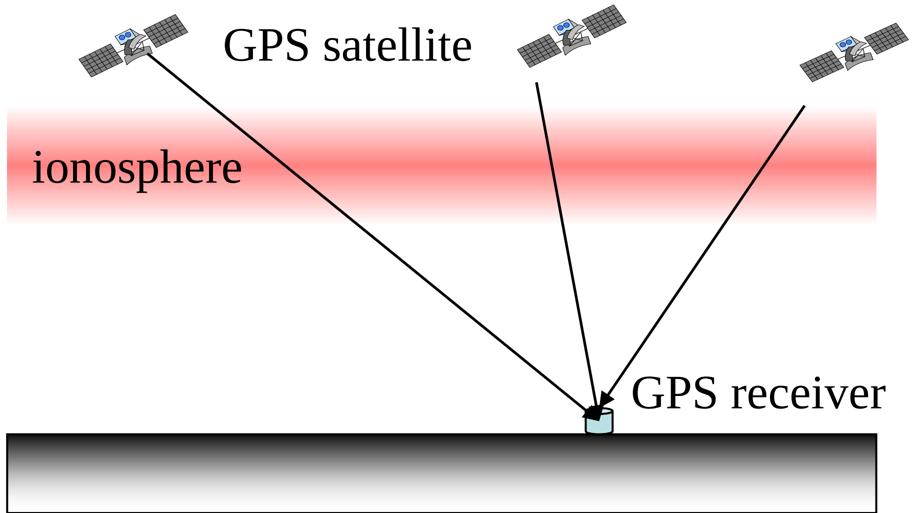
GPS satellite
ionosphere
GPS receiver

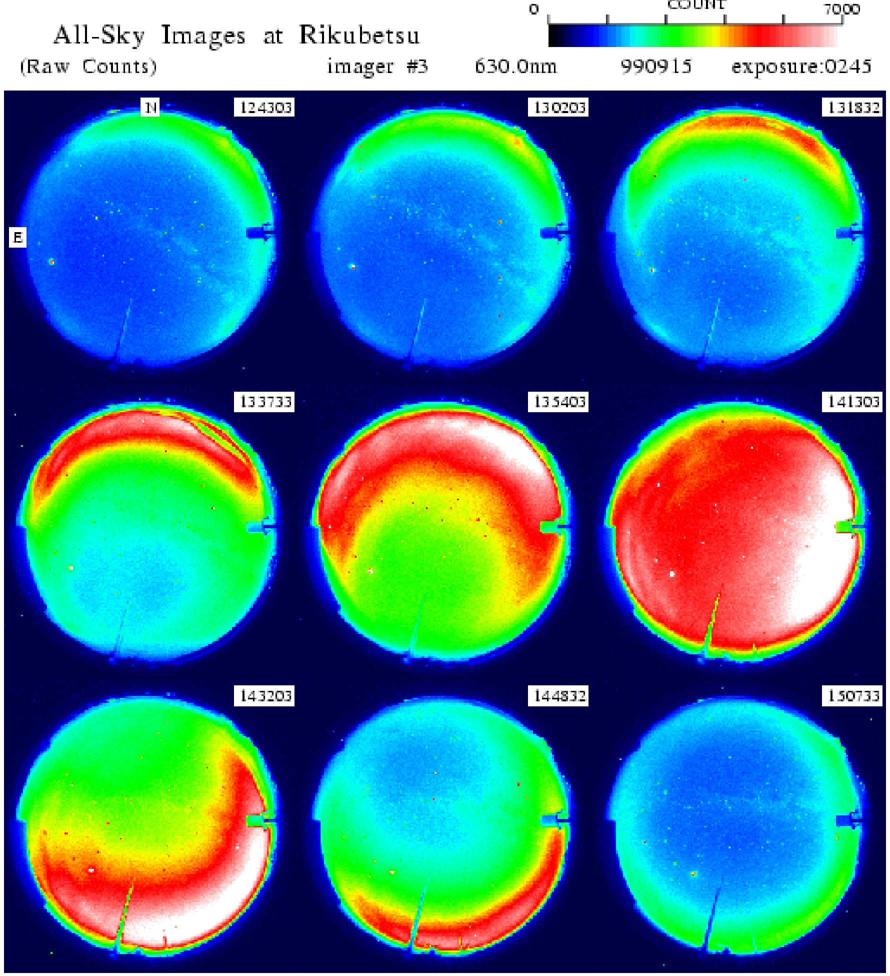

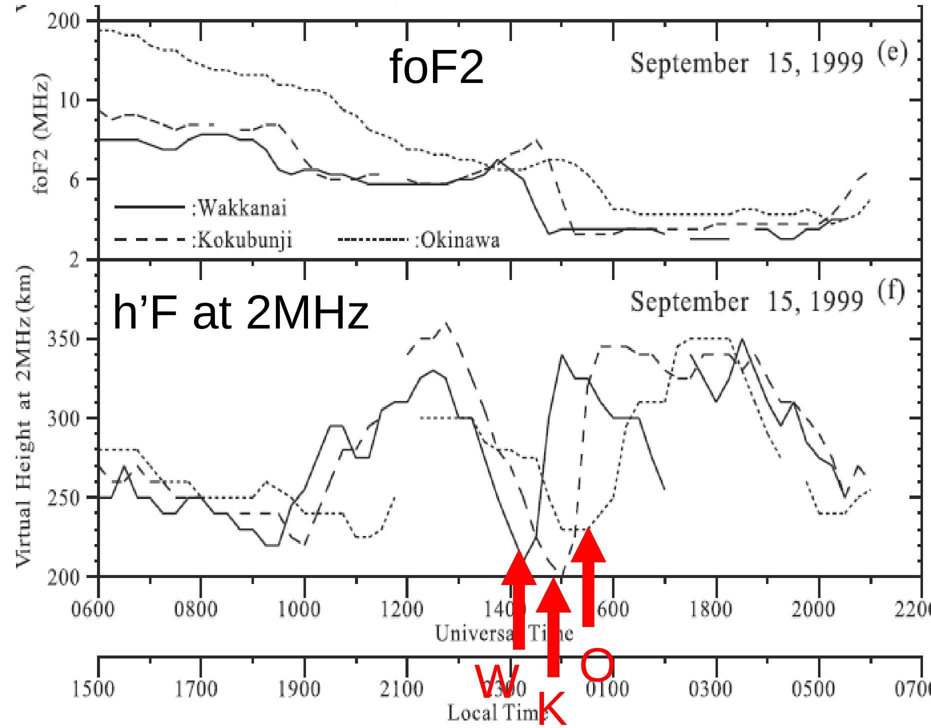

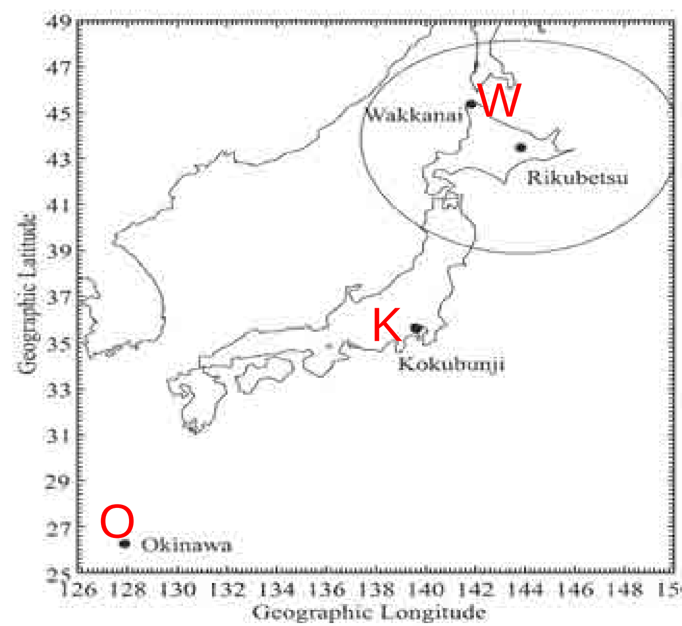

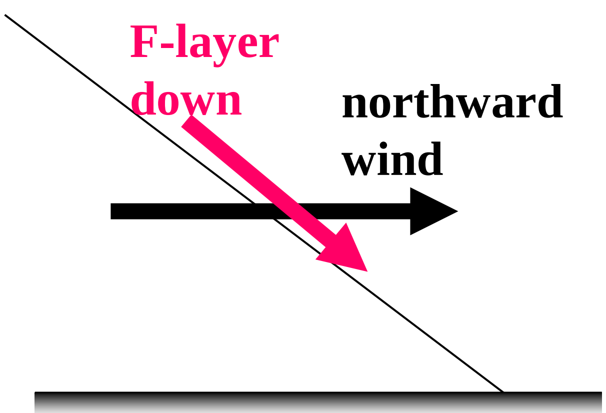

Shiokawa et al. [JGR, 2002]

$$O^+ + O_2 \longrightarrow O_2^+ + O$$

$$O_2^+ + e \longrightarrow O(^1D) + O$$

$$O(^1D) \longrightarrow O(^3P) + h\nu_{630.0nm}$$

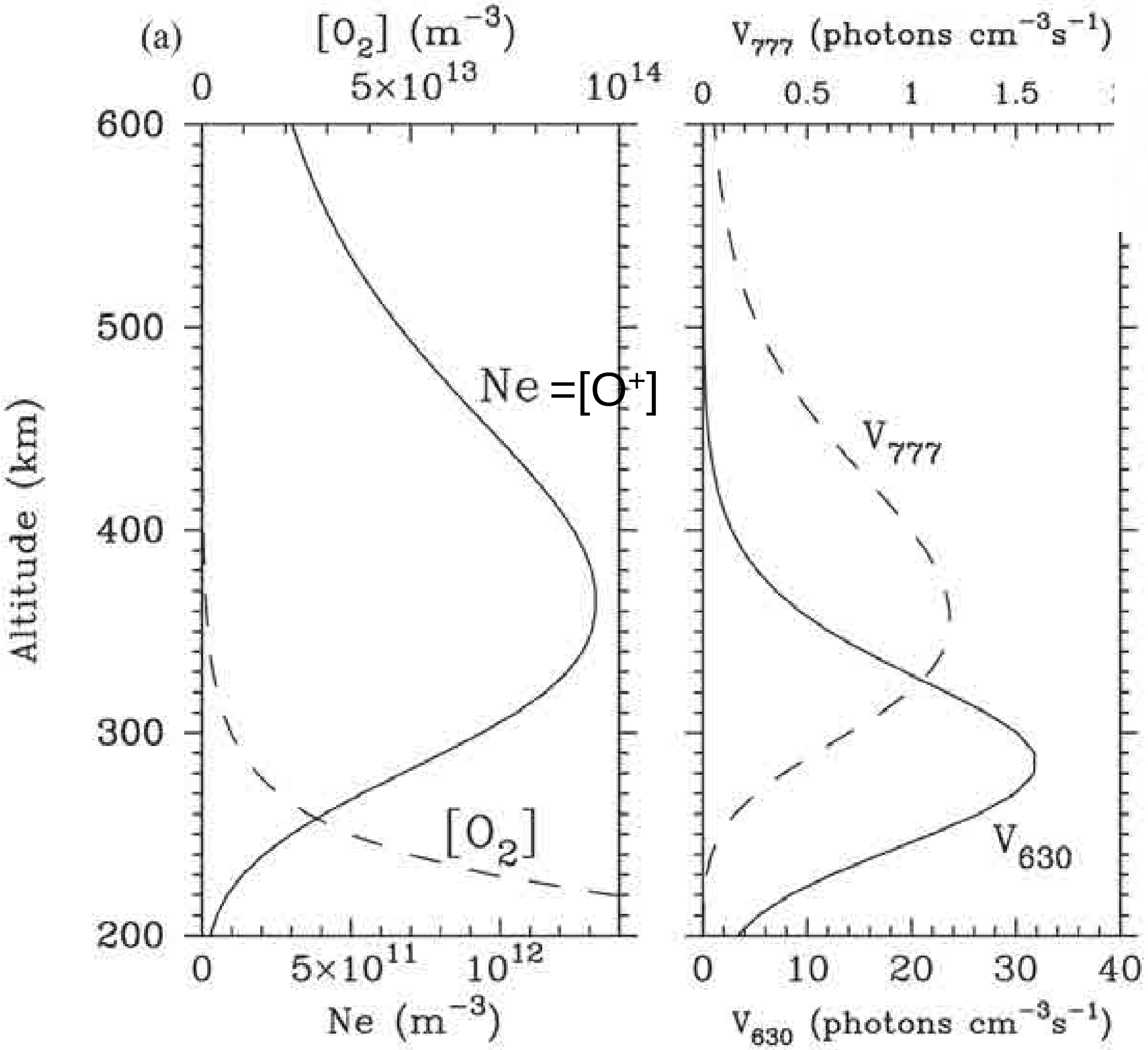

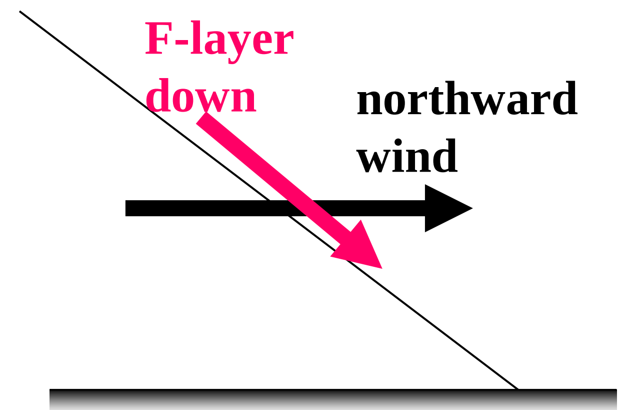

Shiokawa et al.
[JGR, 2003]

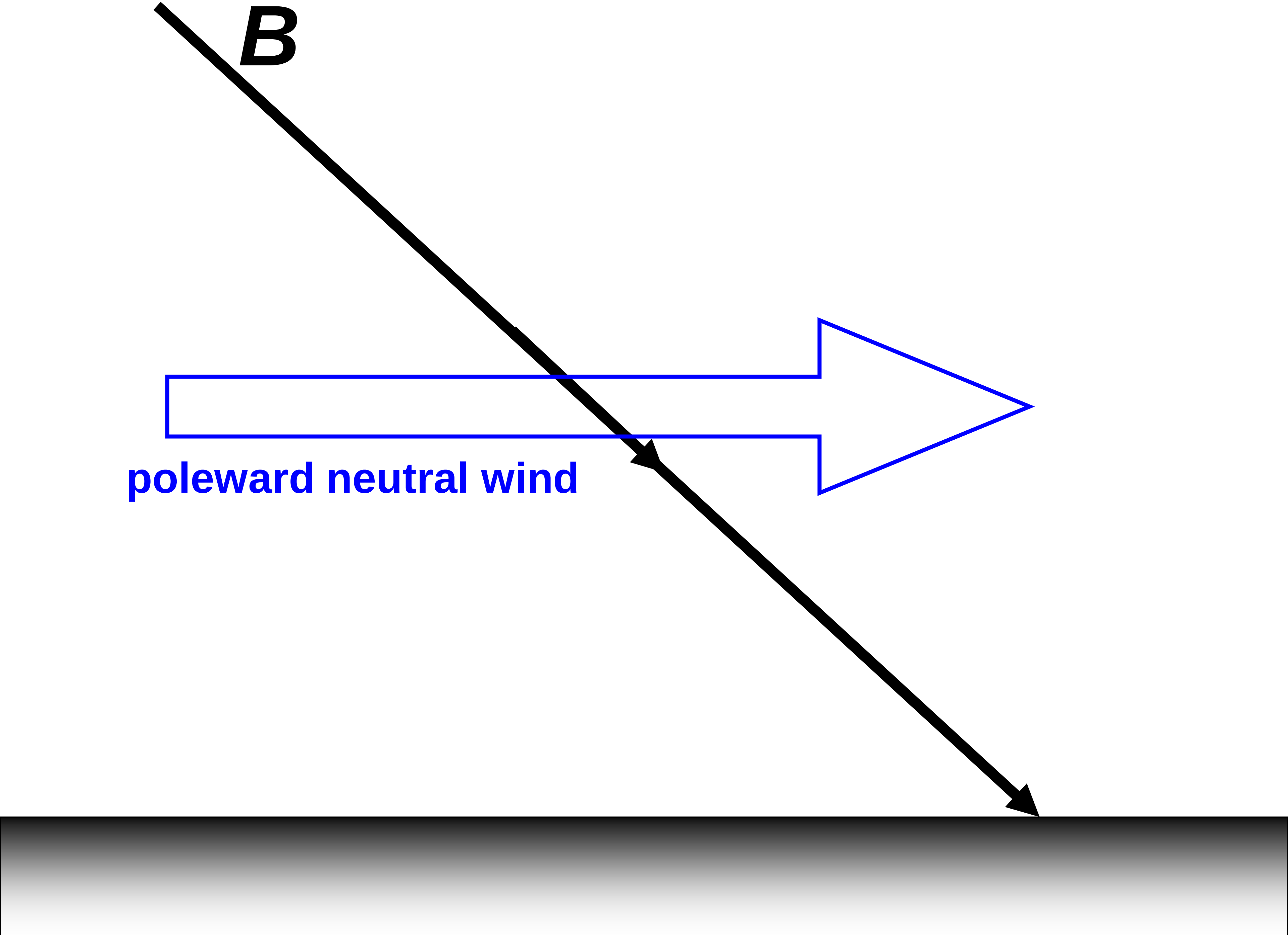
B
poleward neutral wind

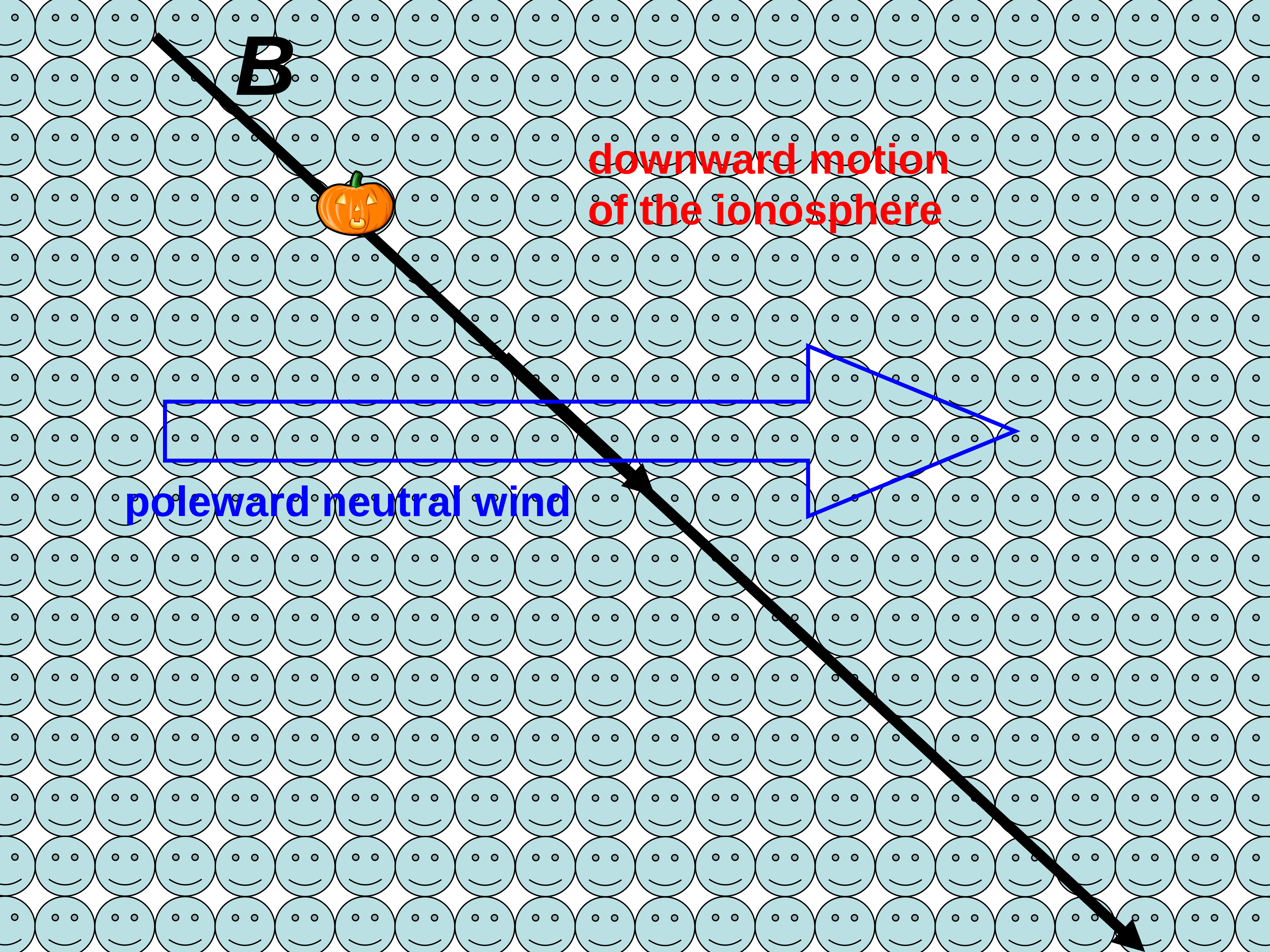
B
downward motion
of the ionosphere
poleward neutral wind

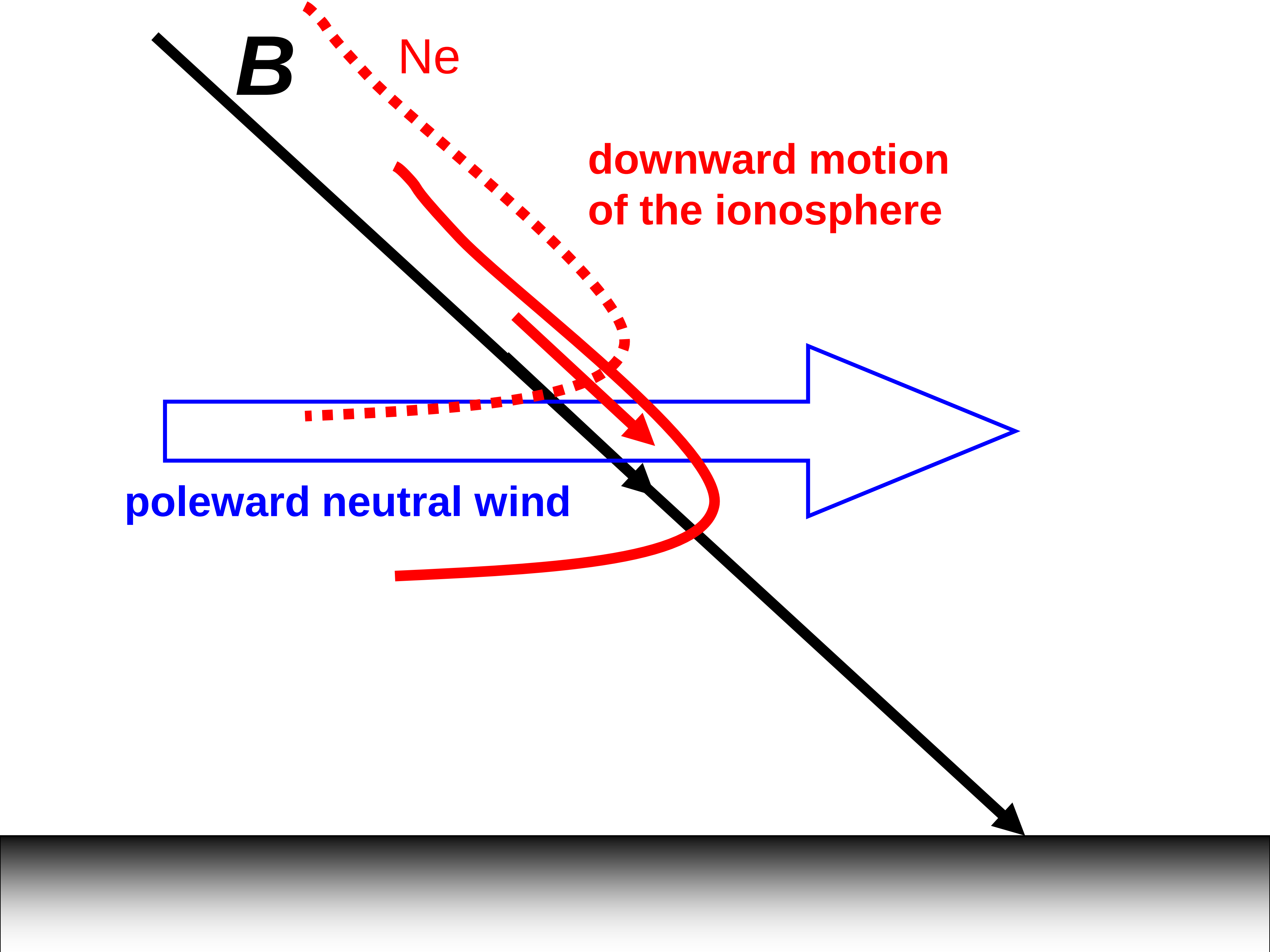
B
Ne
downward motion
of the ionosphere
poleward neutral wind

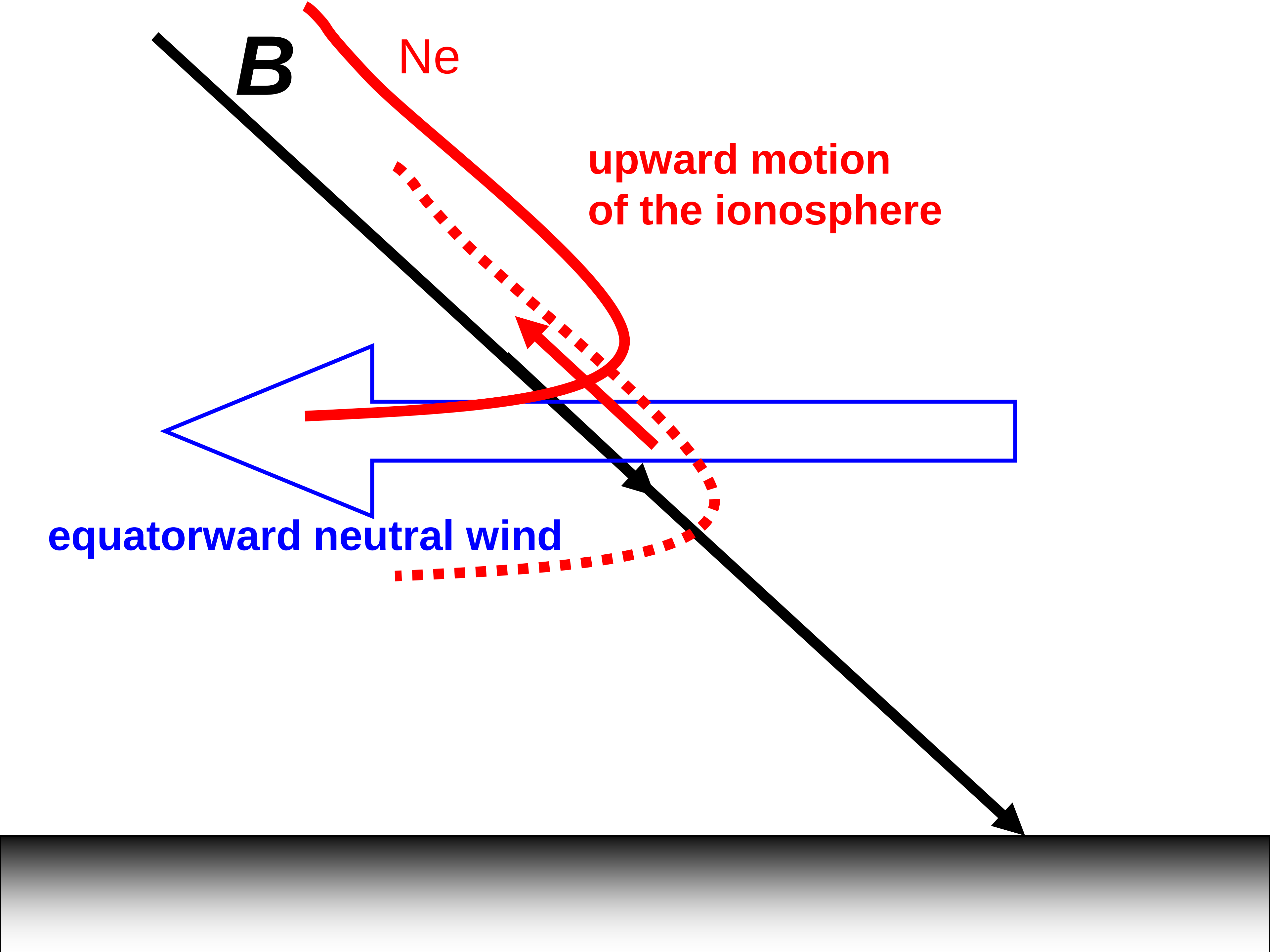
B
Ne
upward motion
of the ionosphere
equatorward neutral wind

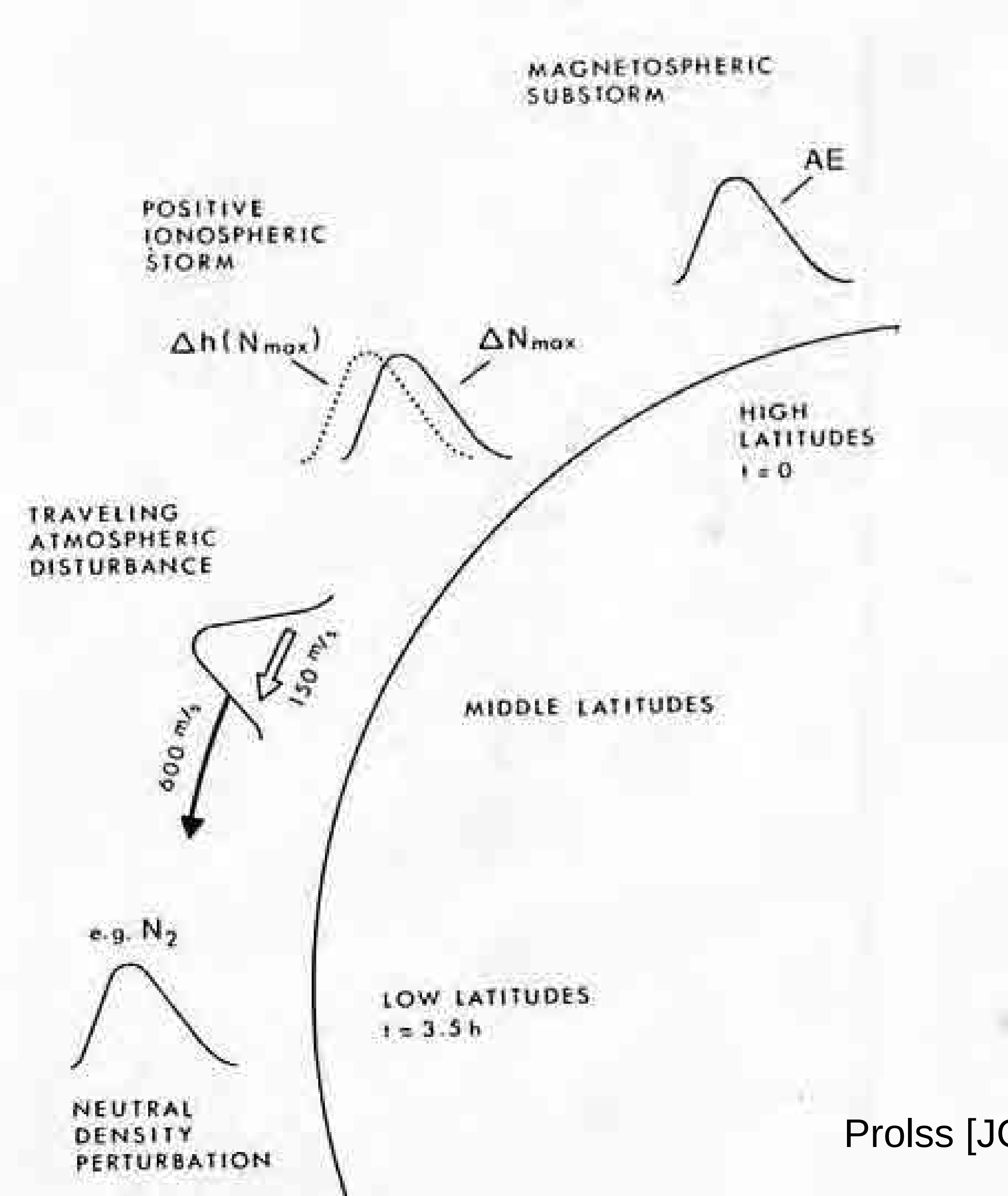

Prolss [JGR, 1993]

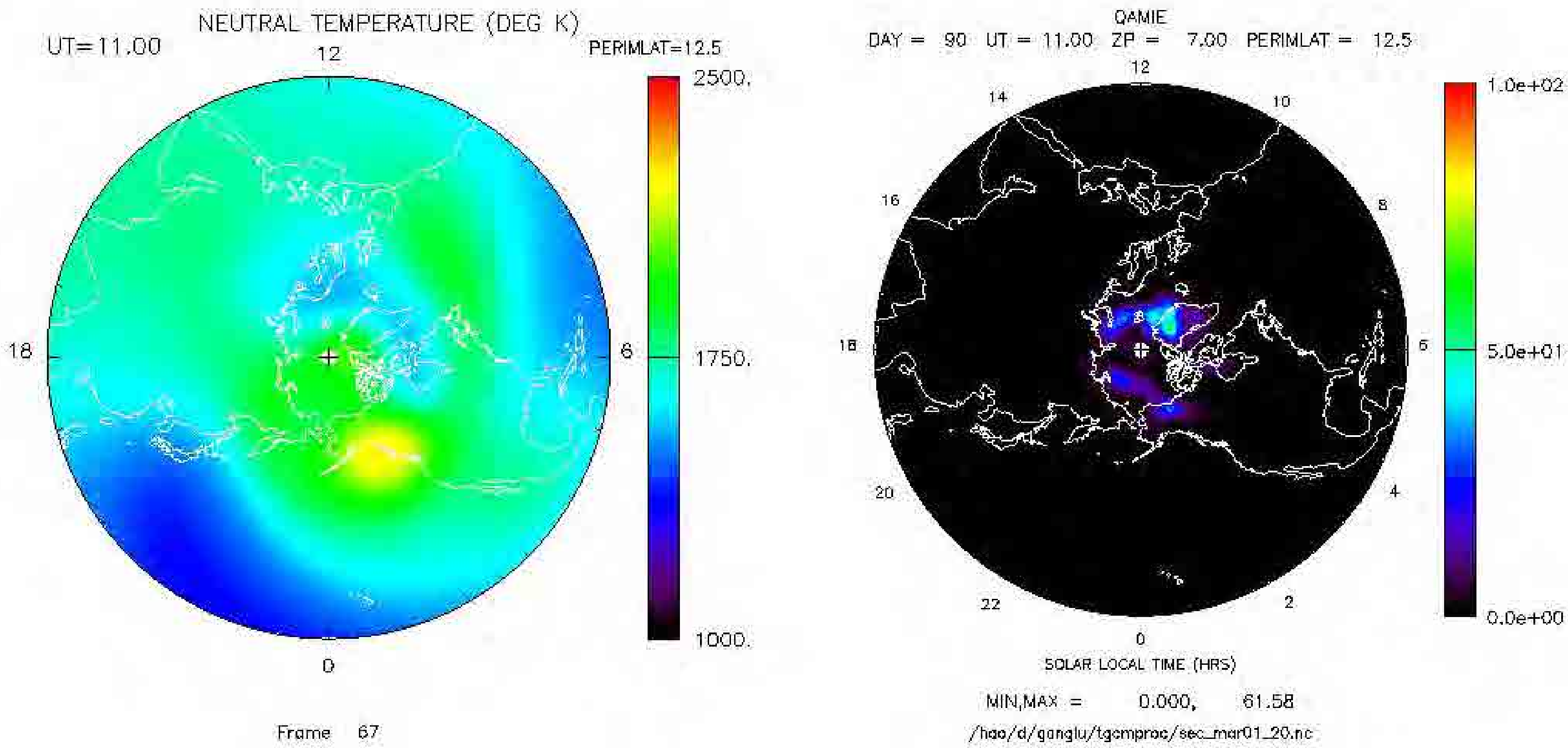

Shiokawa et al. [JGR, 2007]

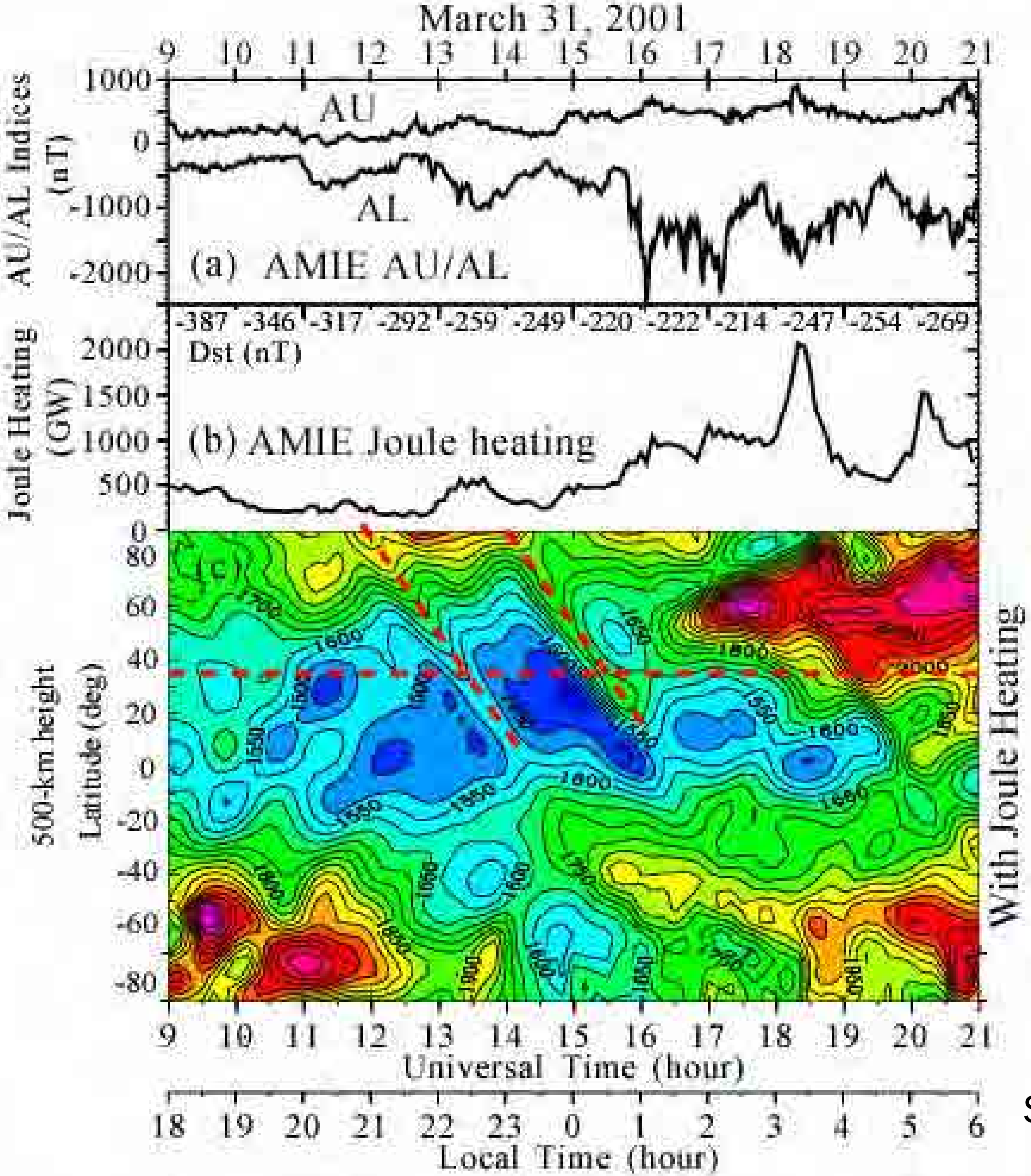

phase speed: ~1100 m/s

impulsive JHs → TADs

continuous JH → global heating

no conjugacy

wave-wave interaction?

Shiokawa et al. [JGR, 2007]

Brightness wave from midnight temperature maximum

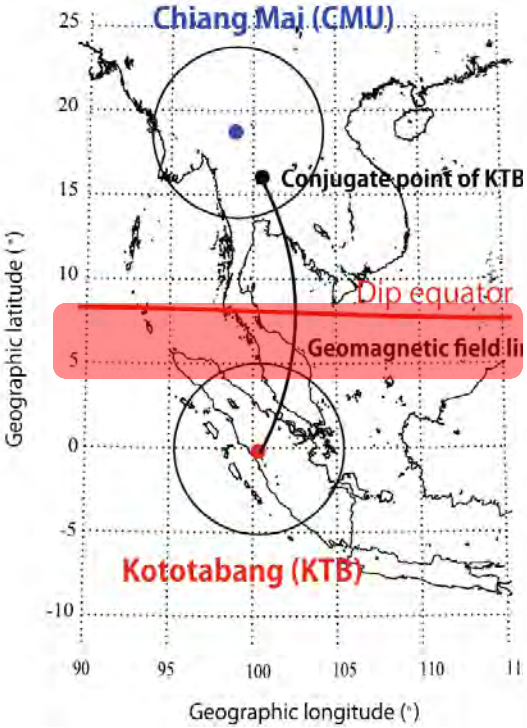

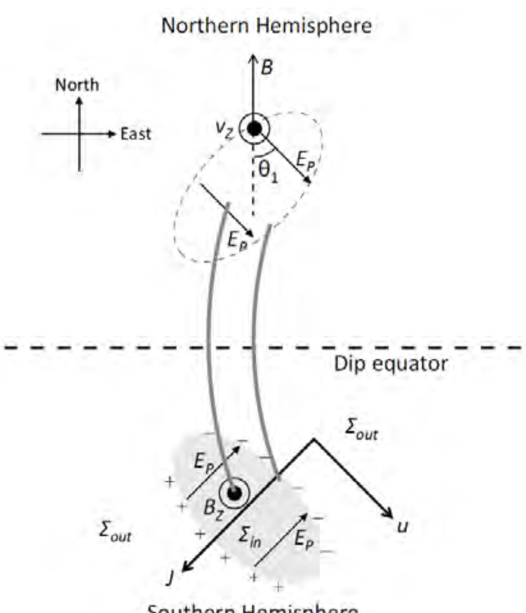

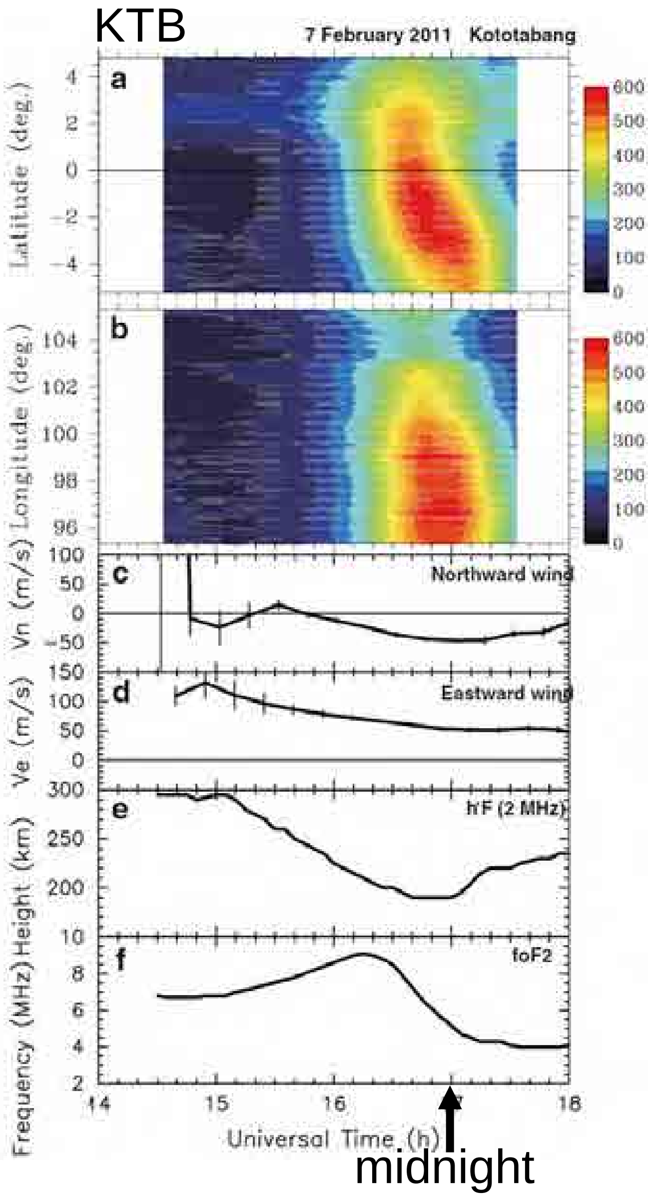

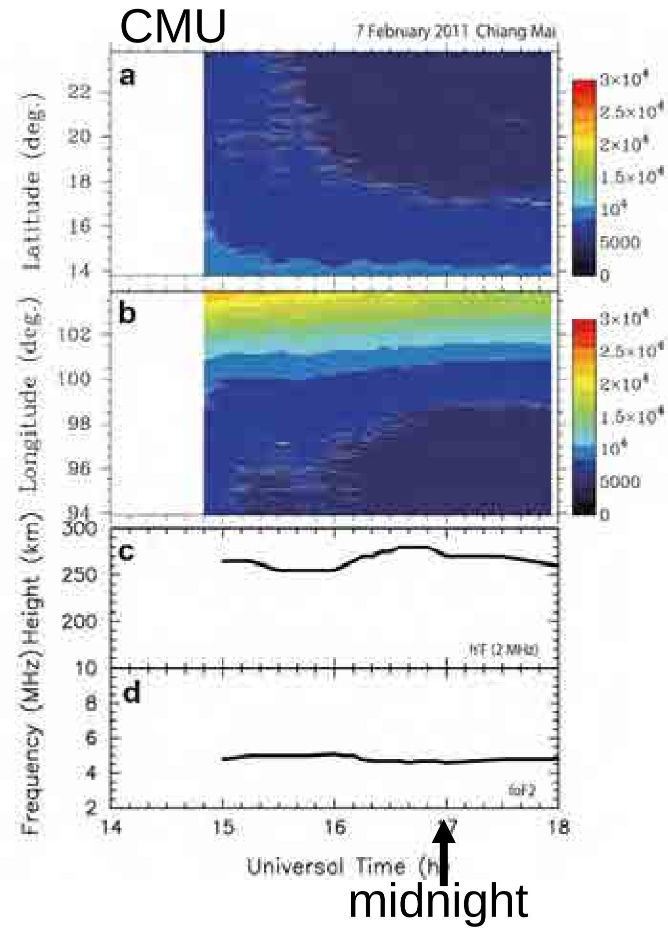

Fukushima *et al. Earth, Planets and Space* (2017) DOI 10.1186/s40623-017-0698-z

Source of traveling ionospheric disturbances

- **Gravity waves from the lower atmosphere**

  tropospheric convection
  jet wind streak (stratosphere/mesosphere)
  typhoon, earthquake/tsunami, volcanic eruption
  secondary gravity waves by gravity wave dissipation

- **Gravity waves from auroral energy input**

  Joule heating
  Lorentz force

- **Ionospheric instabilities**

  Perkins instability
  E-F coupling instability

Medium-scale traveling ionospheric disturbances (MSTIDs)

Nightime Medium-Scale Traveling Ionospheric Disturbances (MSTIDs)

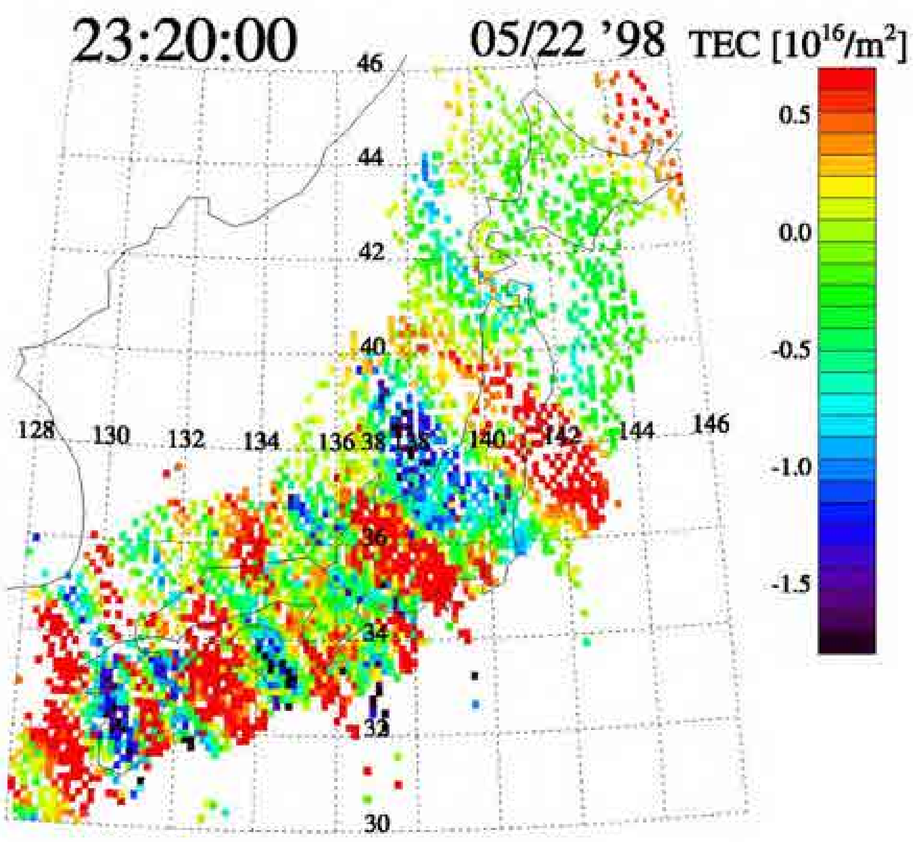

Saito et al. (GRL, 2001)

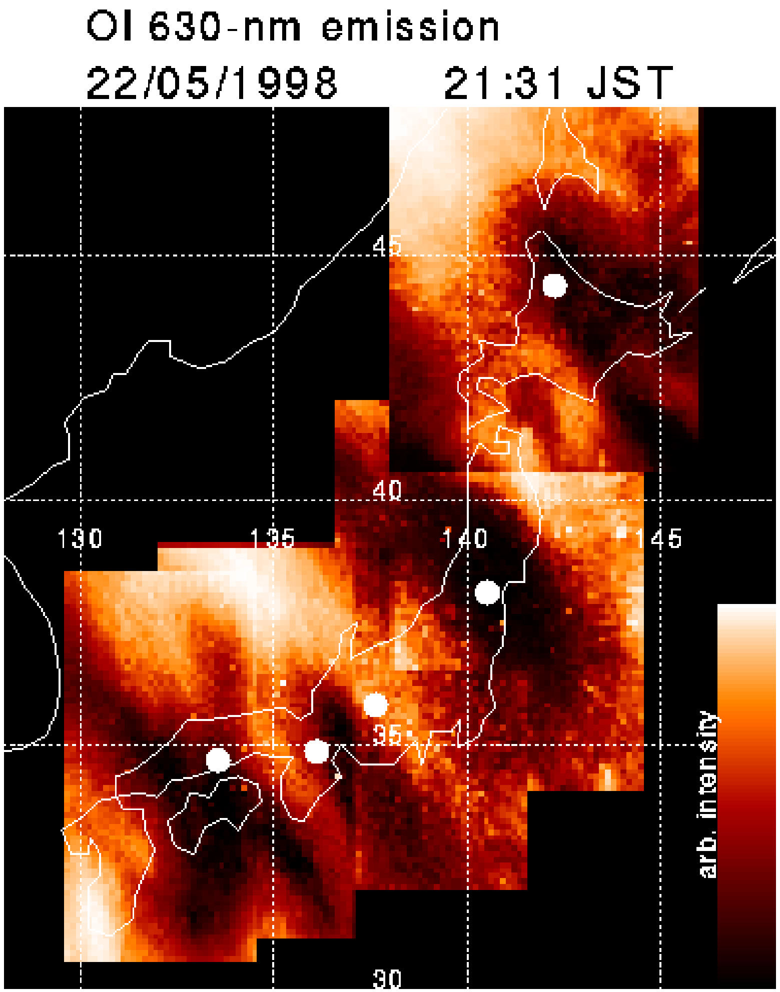

Kubota et al.(GRL, 2000)

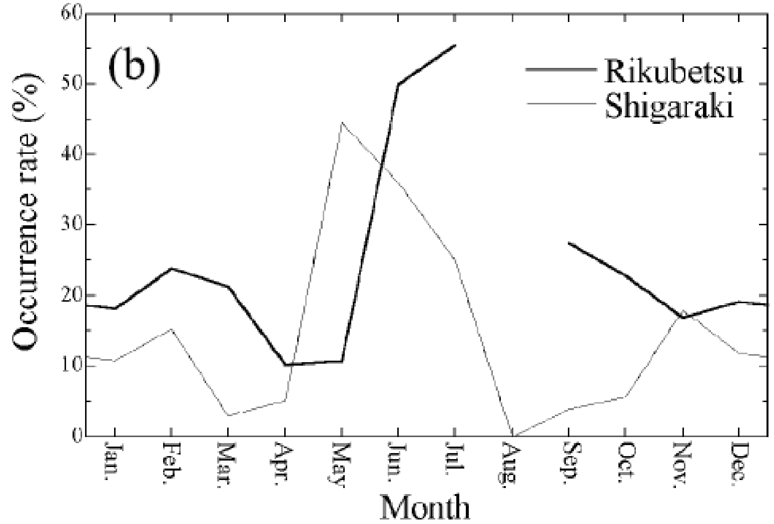

Shiokawa et al. (JGR, 2003a)

MSTID statistics at Shigaraki and Rikubetsu

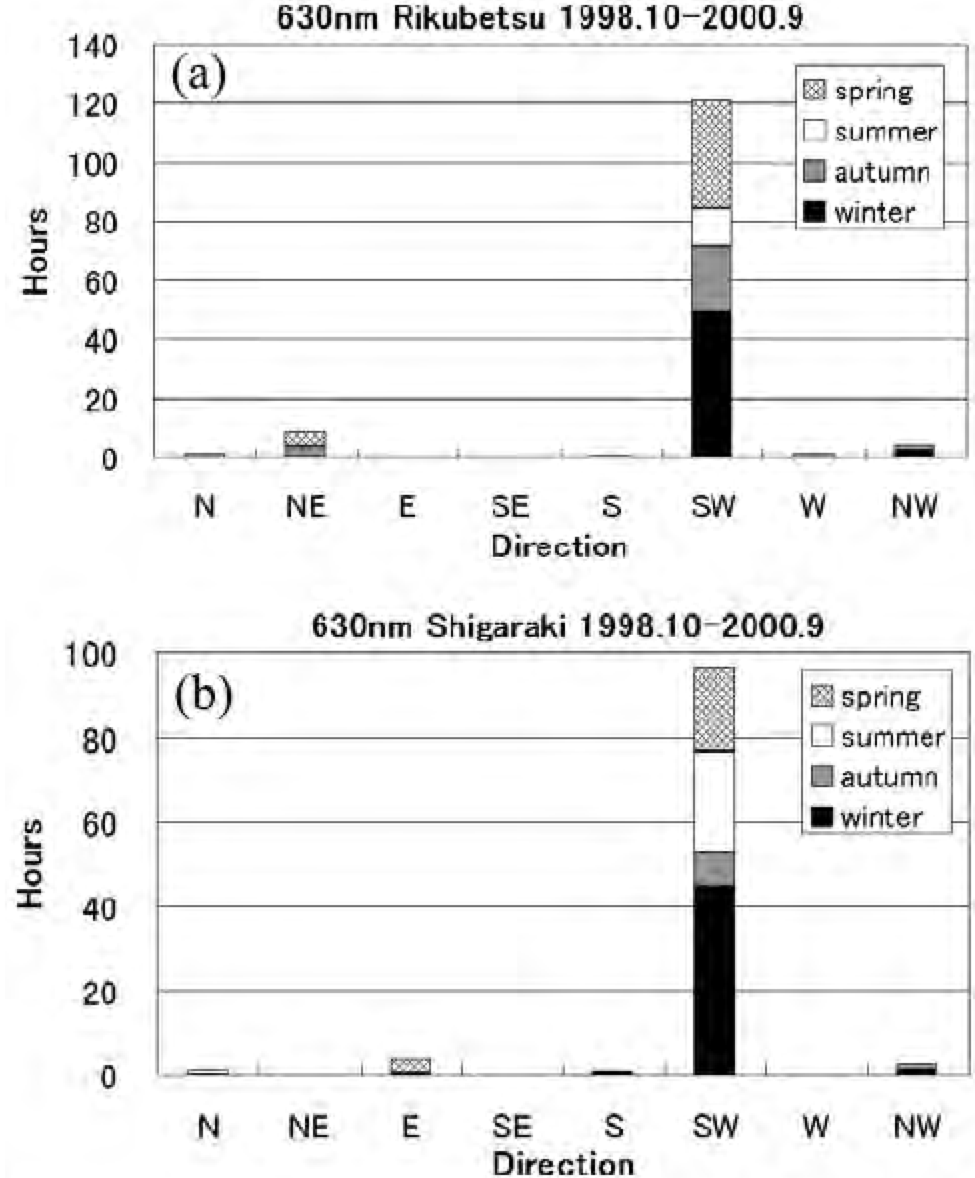

Figure 6. Directions of MSTID propagation (in total hours for each season) observed in the 630-nm airglow images at (a) Rikubetsu and (b) Shigaraki.

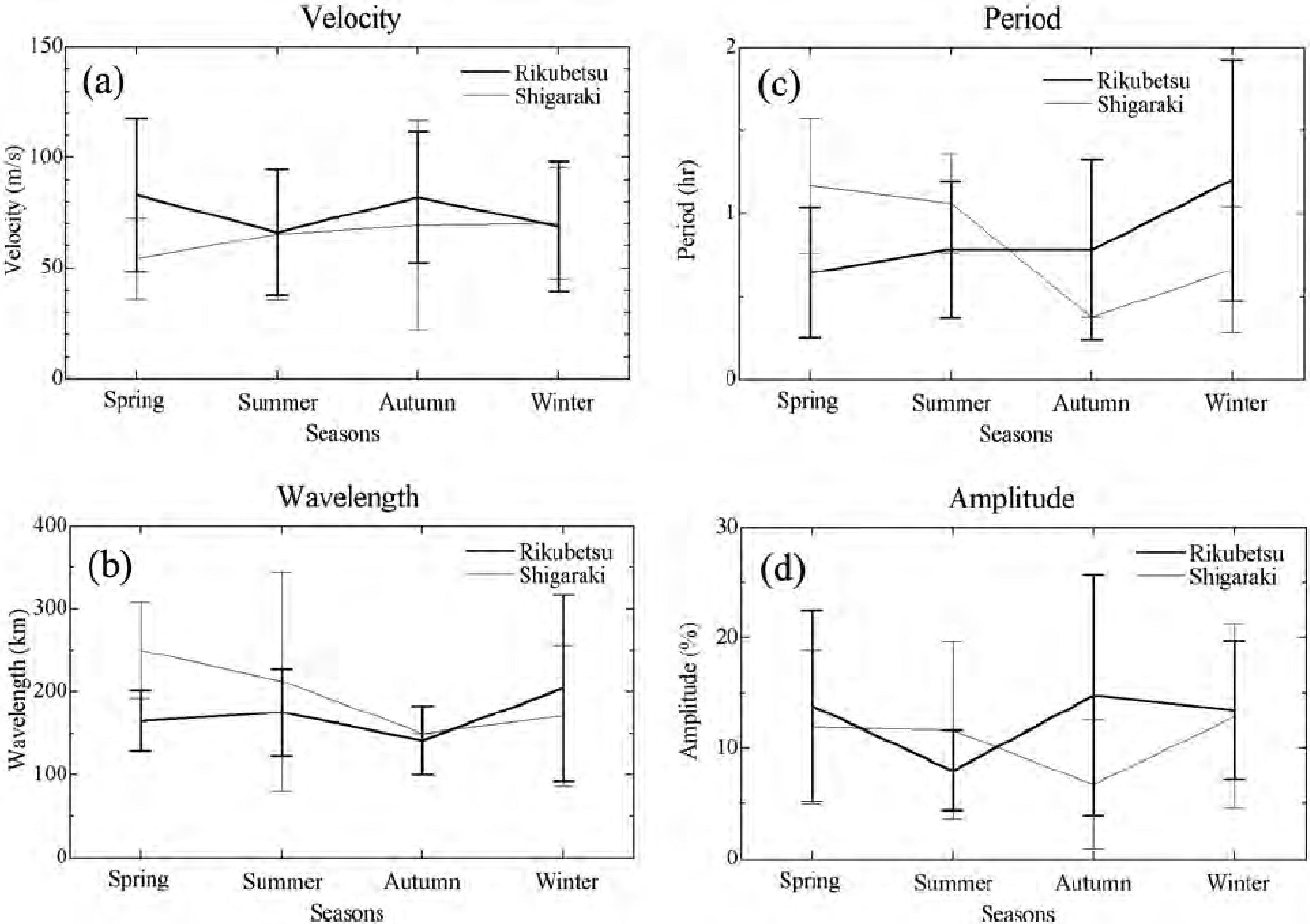

Shiokawa et al. (JGR, 2003a)

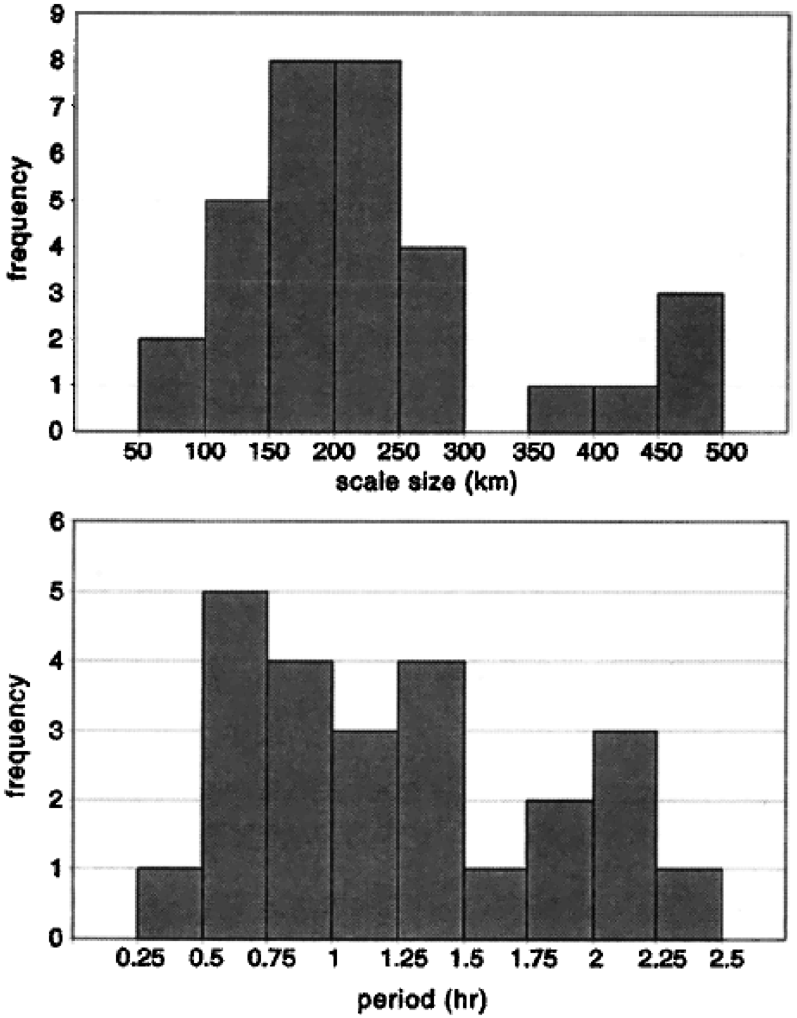

Figure 8. Histogram of ZTID (top) scale sizes and (bottom) periods. Data from Hawaii, Puerto Rico, and Ithaca are included.

Garcia et al. (JGR, 2000)

MSTID statistics at Arecibo, Puerto Rico

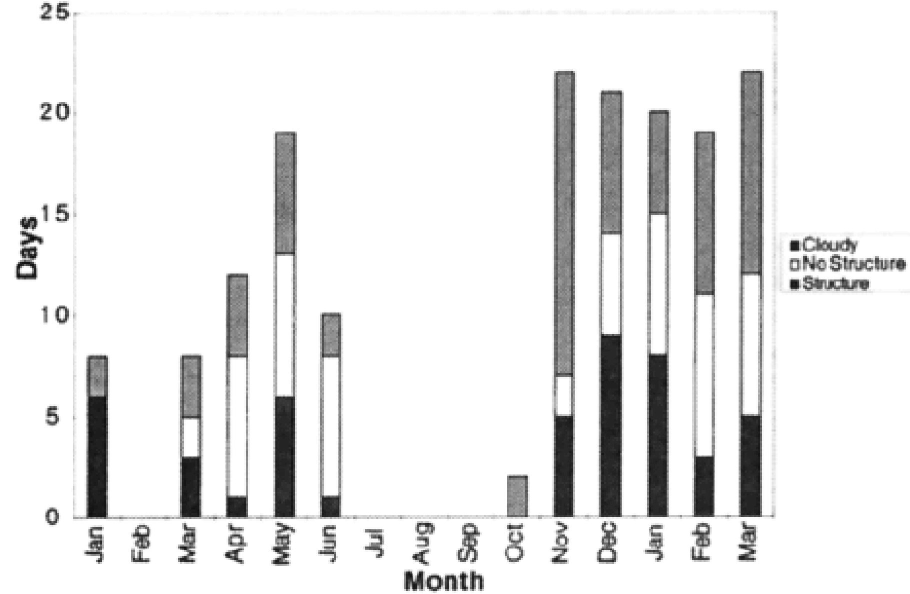

Figure 3. Occurrence of thermospheric events in the 630.0 nm emission over Arecibo by month (1997-1998.2). A
tent struc
a sequence
the camer
were less t
vations.

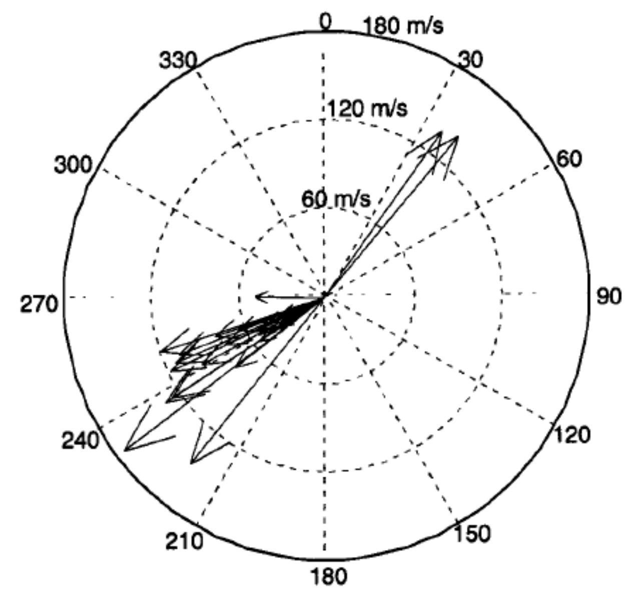

Figure 7. A compass plot of the velocities of the airglow structures observed.

daytime & nighttime MSTIDs

Daytime and nighttime MSTIDs

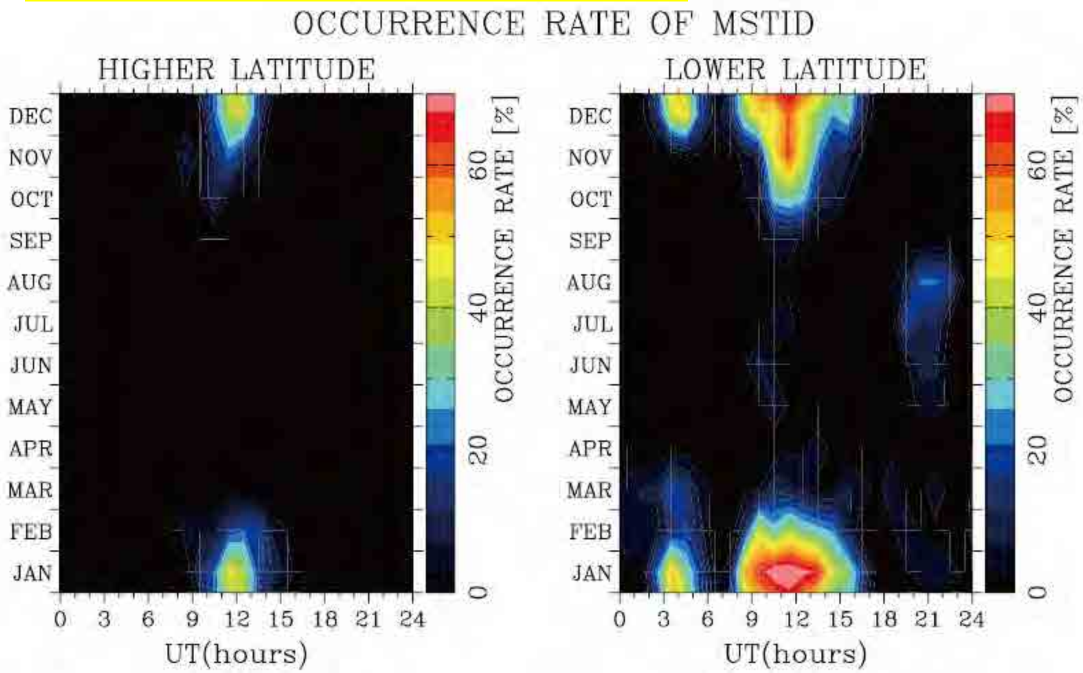

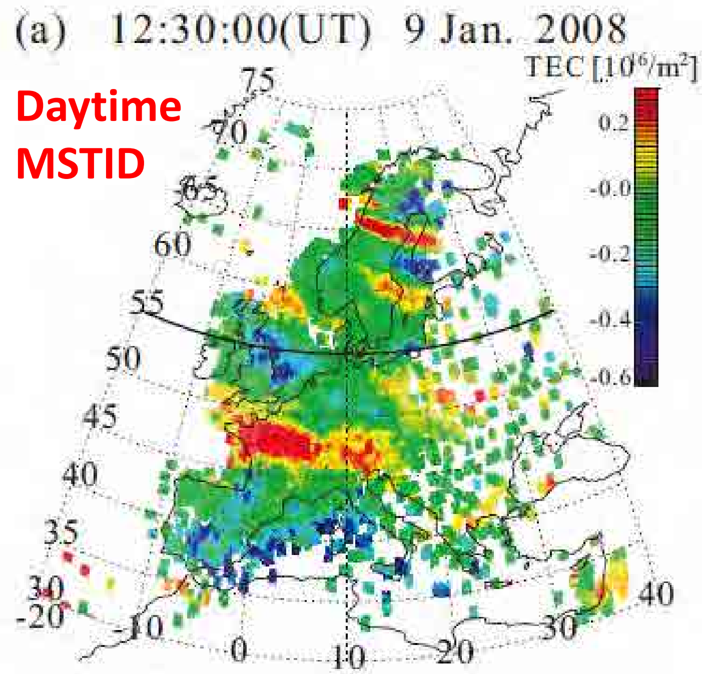

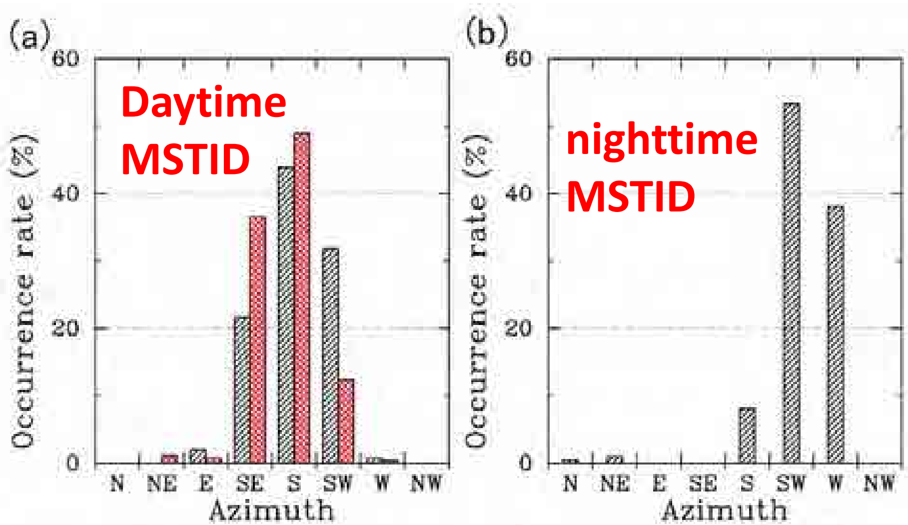

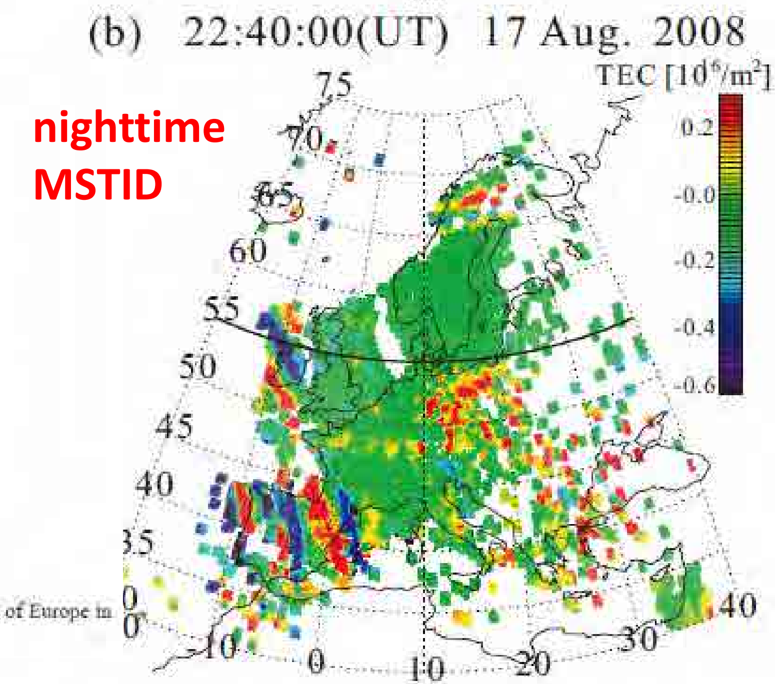

Fig. 4. Propagation direction of the **(a)** daytime and **(b)** nighttime MSTIDs at (red) higher and (black) lower latitude regions of Europe in 2008. Note that the nighttime MSTIDs were not observed in the higher latitude region.

Otsuka et al. (AnnGeo, 2013)

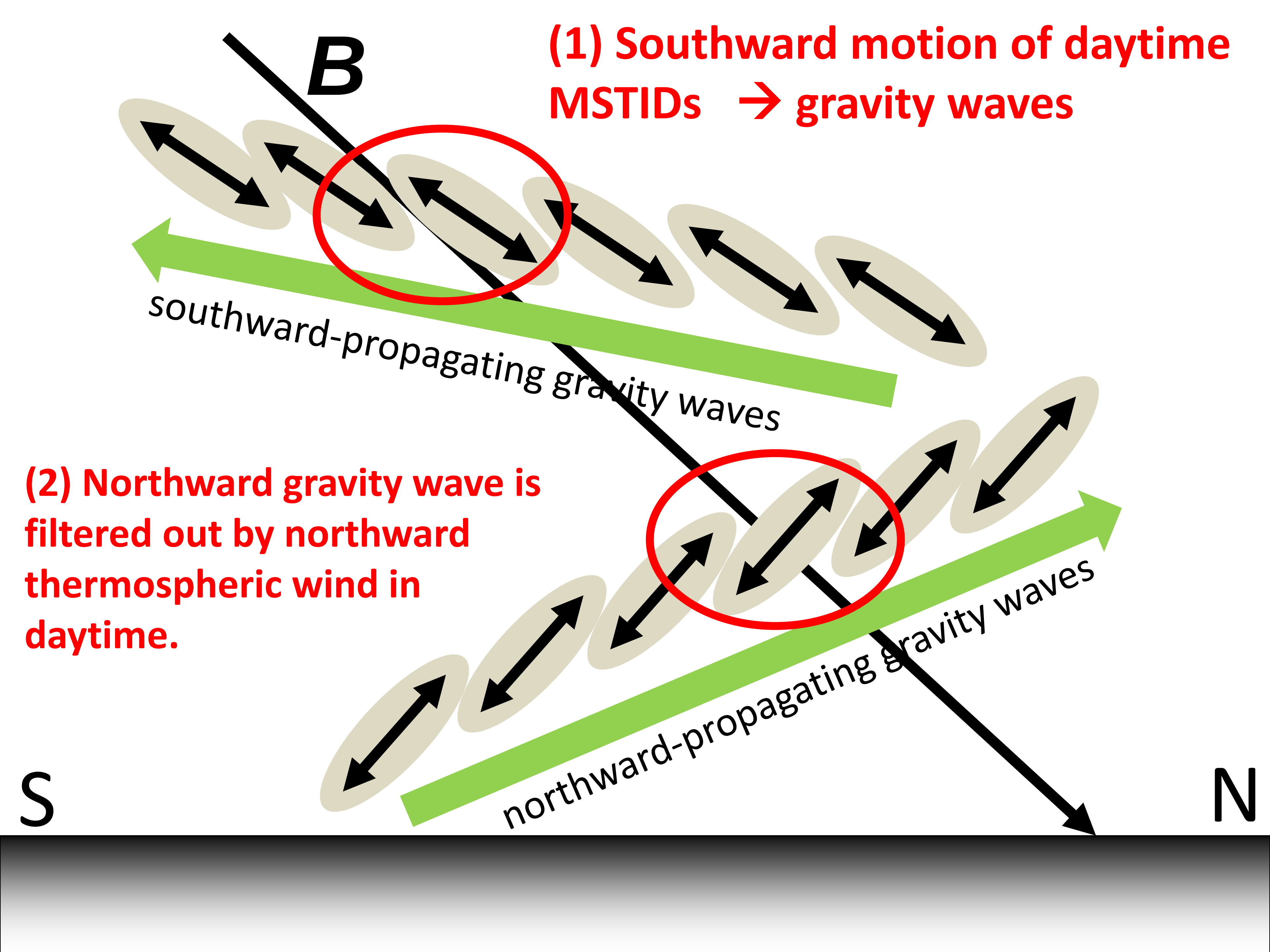
(1) Southward motion of daytime MSTIDs → gravity waves
B
southward-propagating gravity waves
(2) Northward gravity wave is filtered out by northward thermospheric wind in daytime.
northward-propagating gravity waves
S
N

Miyoshi et al. (JGR, 2018): MSTID simulation by the GAIA model → Equatorward-moving daytime MSTIDs are caused by wind-filtering effect by daytime poleward wind.

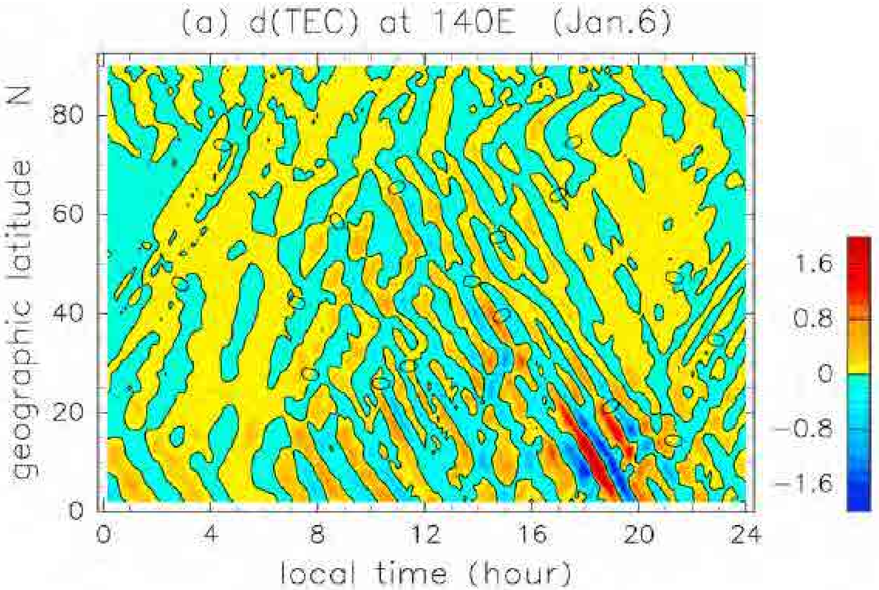

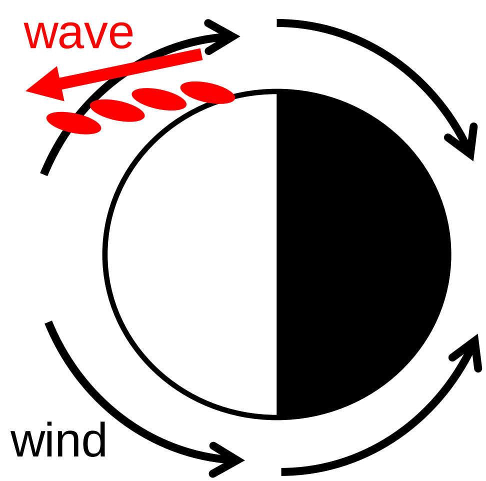

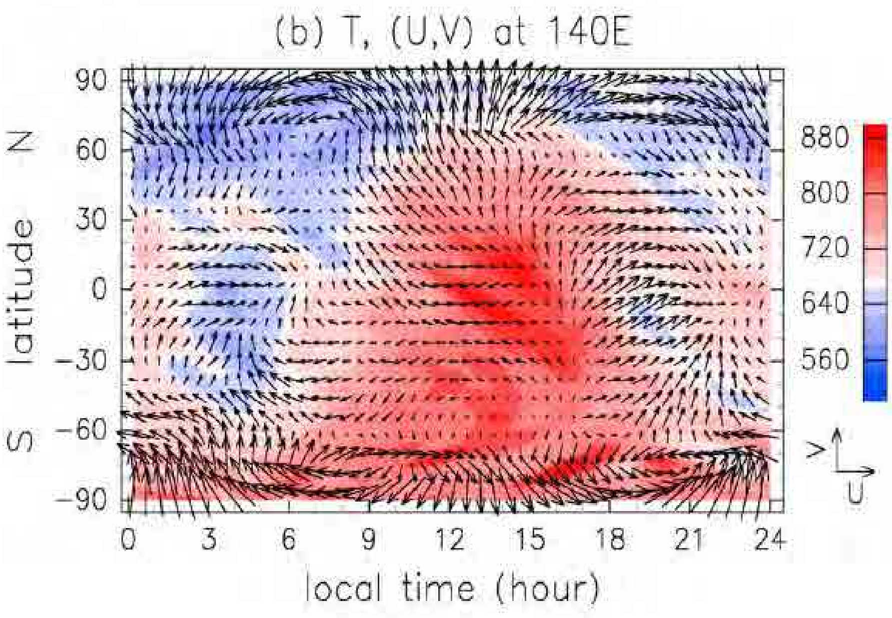

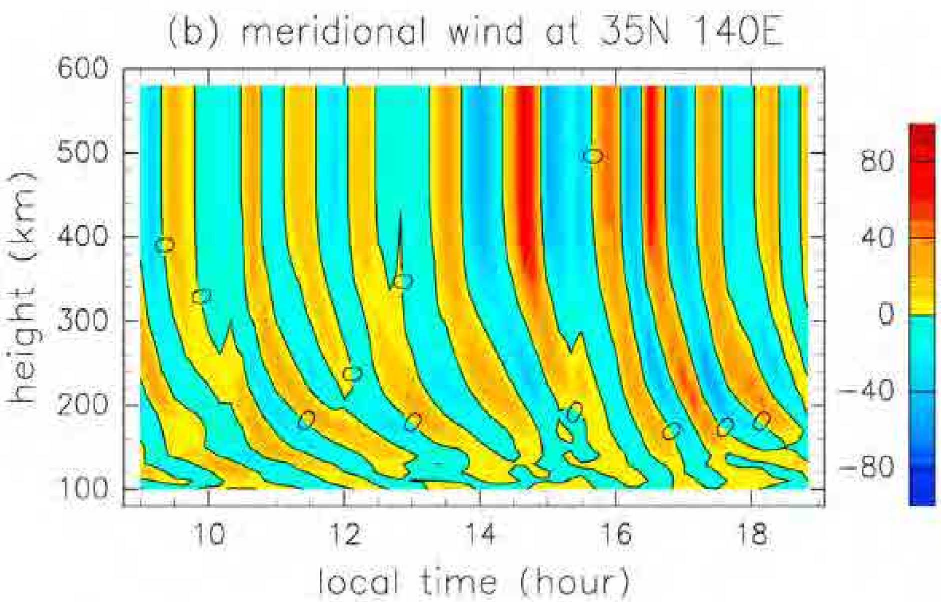

Generation mechanism of nighttime MSTIDs at middle latitudes

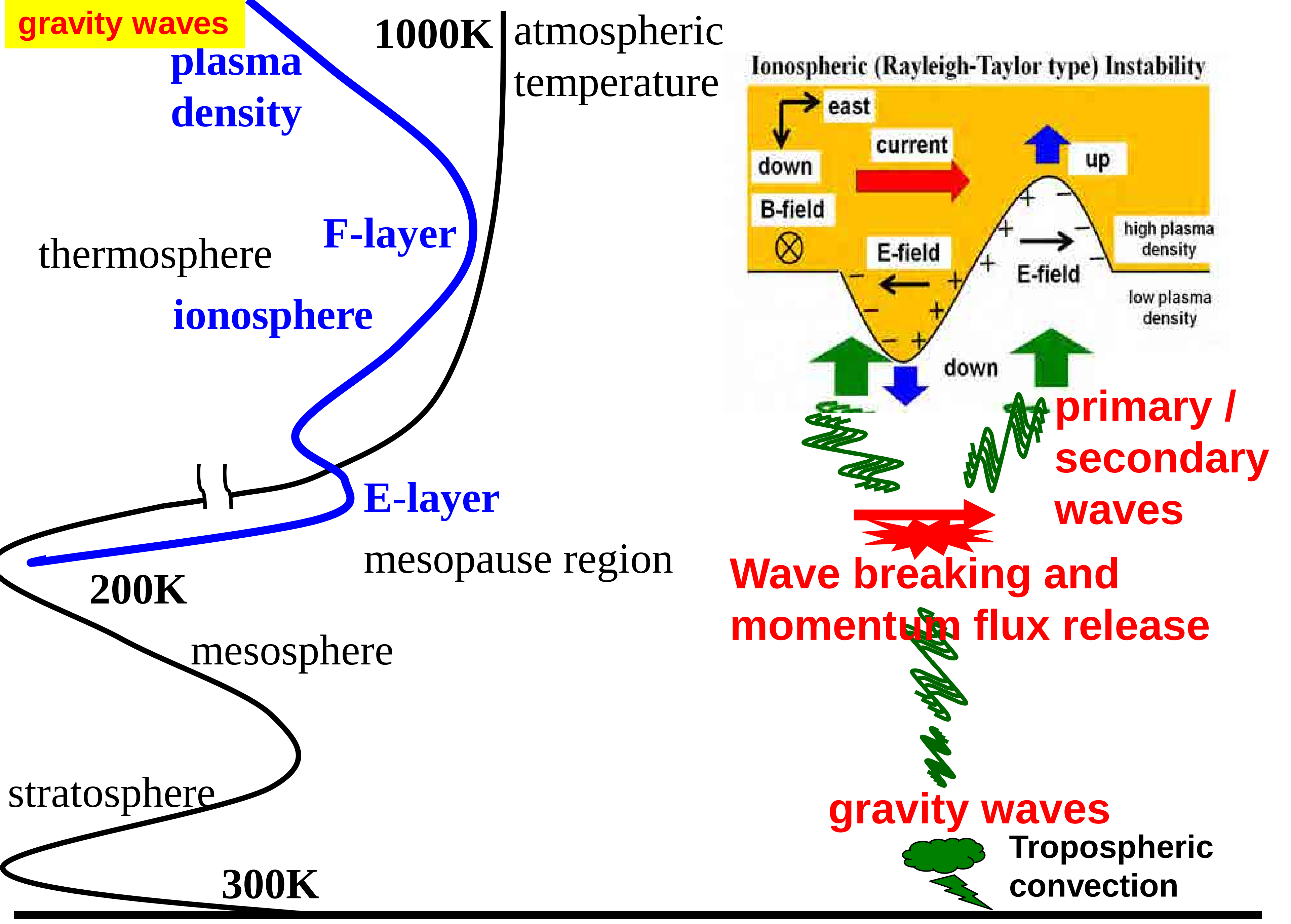
gravity waves
plasma density
1000K
atmospheric temperature
Ionospheric (Rayleigh-Taylor type) Instability
east
down
current
up
B-field
E-field
E-field
high plasma density
low plasma density
down
thermosphere
F-layer
ionosphere
primary / secondary waves
E-layer
mesopause region
Wave breaking and momentum flux release
200K
mesosphere
stratosphere
gravity waves
Tropospheric convection
300K

1. Ionospheric Perkins Instability

Possible cause of MSTIDs

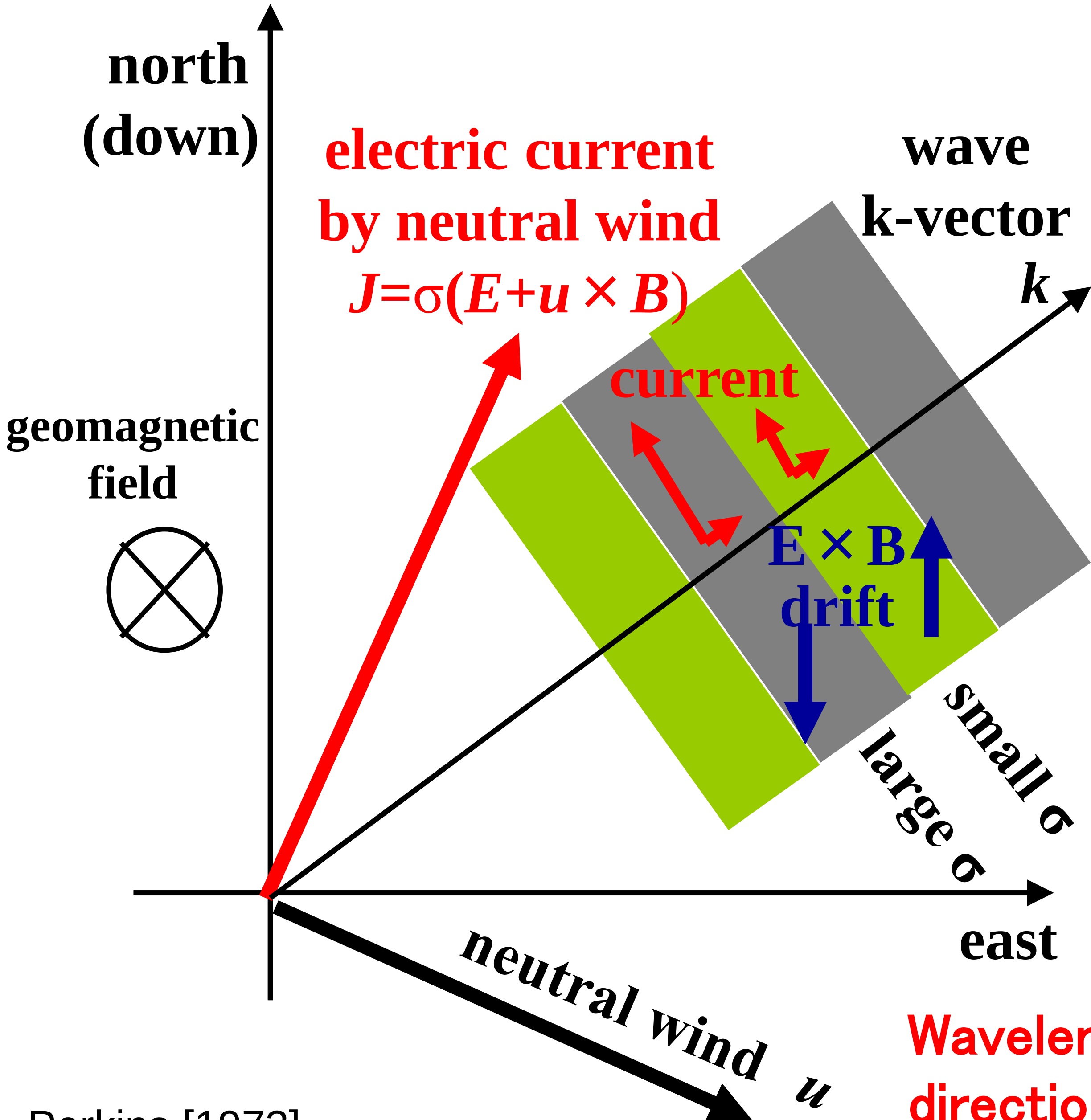

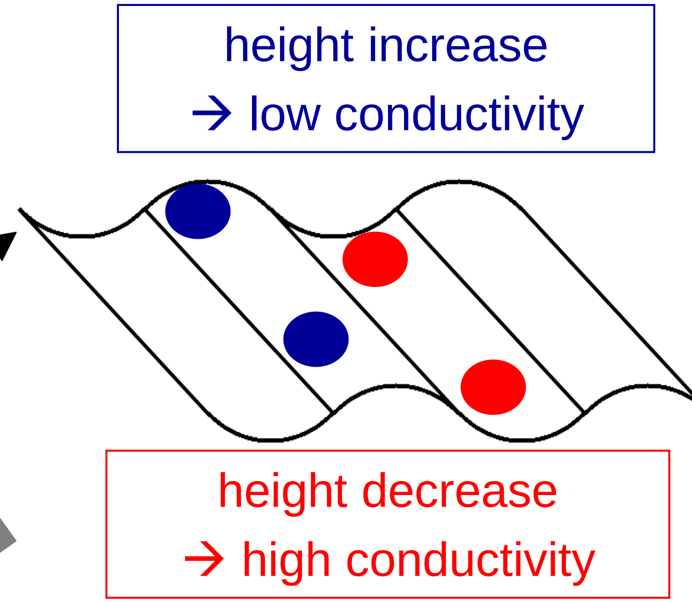

height increase
→ conductivity decrease
→ upward ExB drift
→ further height increase
(similar to the Rayleigh–Taylor type instability)

Wavelength and propagation direction are arbitrary.

Perkins [1973]

Possible cause of MSTIDs

2. Gravity waves

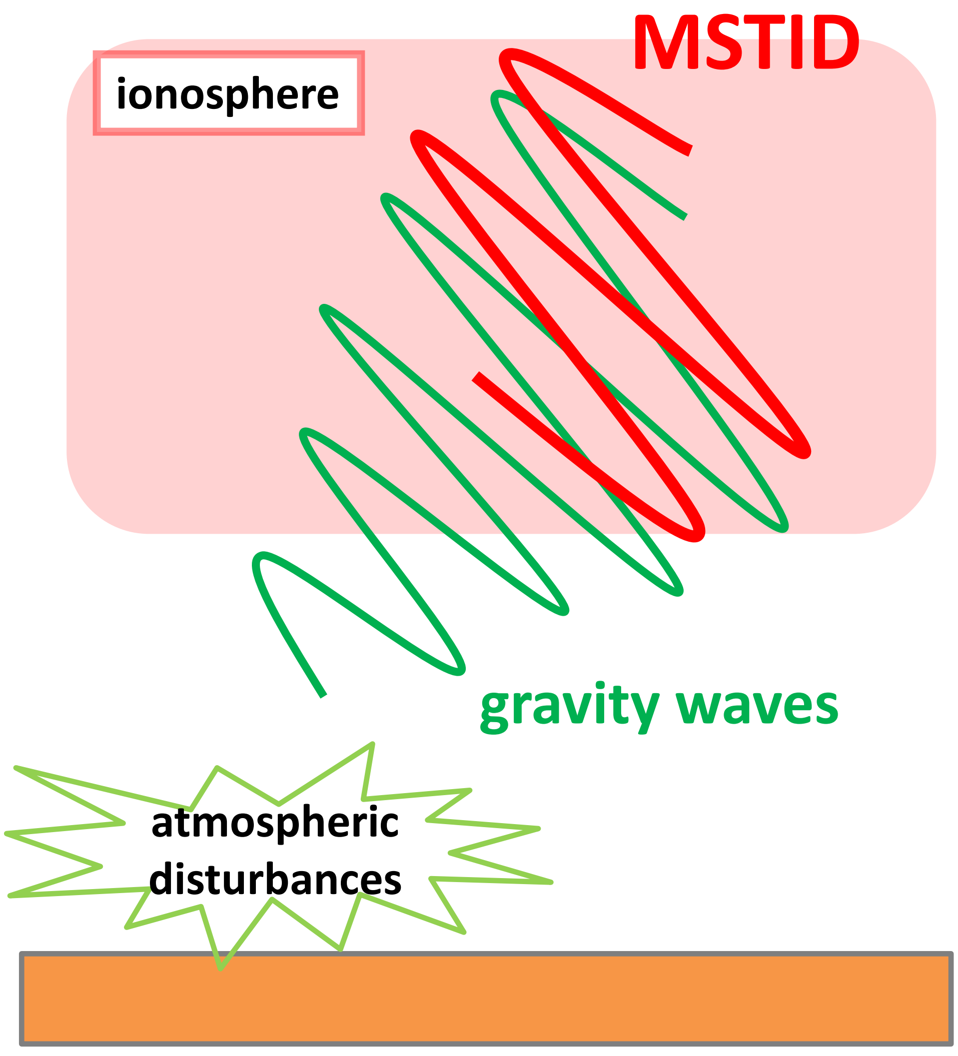

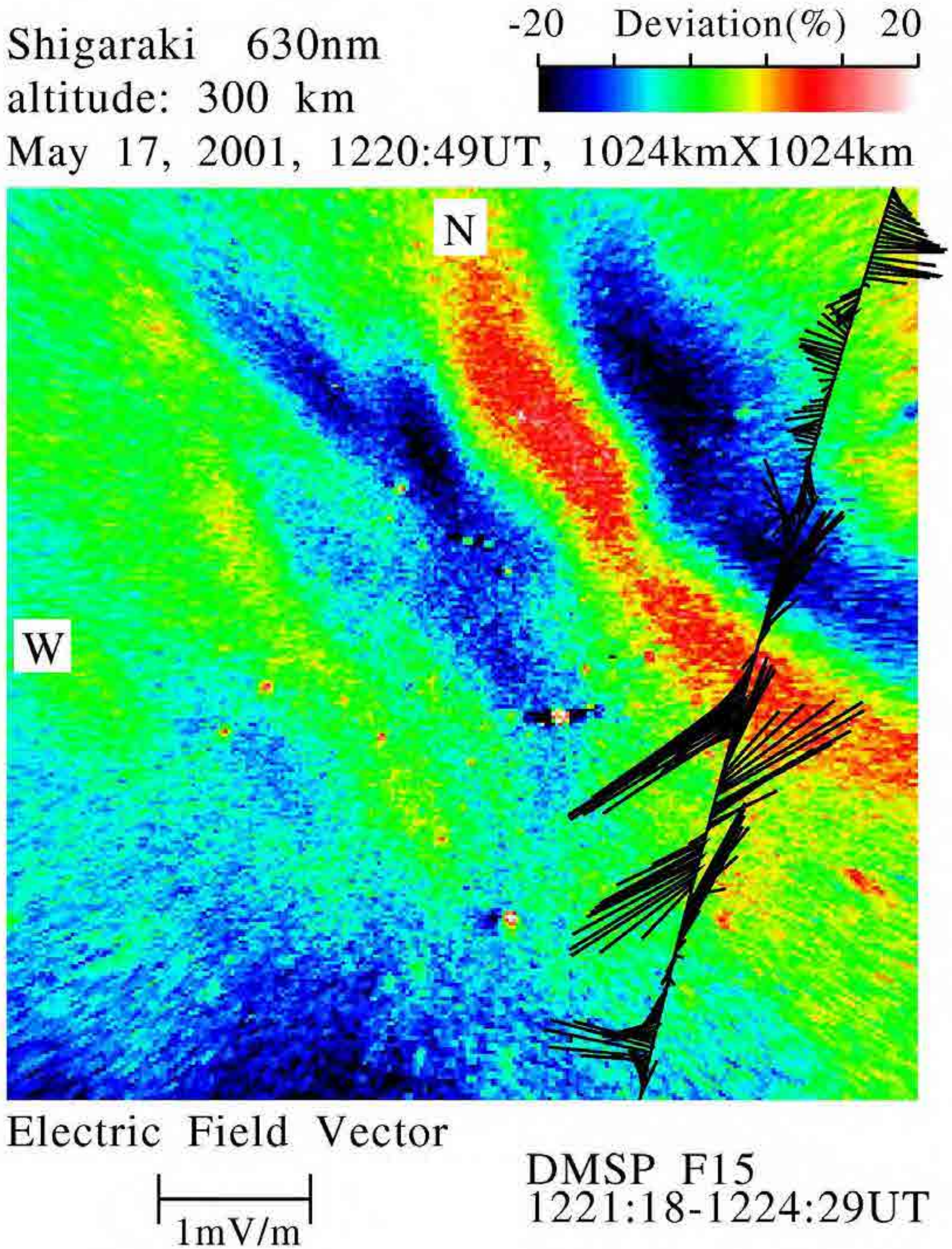

Actually, a DMSP satellite crossed above this MSTID and observed oscillating E-field with an amplitude of ~1 V/m

Shiokawa et al. (JGR, 2003b)

Table 1. Observed and Estimated Parameters of the MSTIDs Observed at Shigaraki on 17 May 2001

	1221 UT	1321 UT	1421 UT	1521 UT
Wavelength λ_h (imager)	230 km	230 km	204 km	273 km
Apparent phase velocity c (imager)	50 m/s	50 m/s	50 m/s	38 m/s
α[a] (imager)	216°	208°	201°	193°
Northward wind (FPI[b])	−78 m/s	−83 m/s	−82 m/s	−116 m/s
Eastward wind (FPI[b])	55 m/s	58 m/s	35 m/s	20 m/s
Southwestward wind U (FPI[b])	17 m/s	18 m/s	34 m/s	69 m/s
Vertical wavelength λ_z[c]	23.9 km	23.2 km	11.5 km	22.4 km
θ^*[d]	37°	37°	23°	6°
Growth rate	1.4×10^{-6} s^{-1}	7.3×10^{-6} s^{-1}	1.9×10^{-6} s^{-1}	-2.0×10^{-6} s^{-1}

[a]Angle between the wave k-vector (southwestward) and the geomagnetic east.
[b]Fabry-Perot interferometer.
[c]Estimated from dispersion relation of gravity wave.
[d]Angle between the direction of $\mathbf{E_0} + \mathbf{U} \times \mathbf{B}$ and the geomagnetic east.

Shiokawa et al. (JGR, 2003b)

Growth rate
$$\gamma = \frac{g \sin^2 I}{\langle \nu_{in} \rangle H_n} \frac{\sin\alpha \sin(\theta^* - \alpha)}{\cos\theta^*} \quad (10)$$

where g, $\langle \nu_{in} \rangle$, H_n, and θ^* are the acceleration of gravity, height-integrated ion-neutral collision frequency, scale height of the neutral atmosphere, and the angle between geomagnetic east and the direction of $\mathbf{E_0} + \mathbf{U} \times \mathbf{B}$. $\mathbf{E_0}$ is the background electric field.

Growth rate＝10^{-6}(/s) , it takes 10^{6}(s) ~ 10 days to grow
→ Linear growth rate is too small for the Perkins instability

Otsuka et al. (JGR, 2007)

Simultaneous observation of Es layer and MSTID

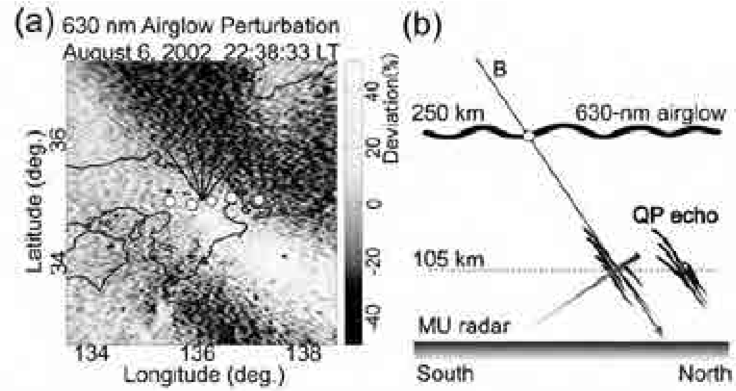

Figure 4. (a) Two-dimensional maps of 630-nm airglow intensity observed with an all-sky imager at Shigaraki, Japan, at 2238 LT on 6 August 2002. Locations of radar beams in the *E* region FAI measurements with the MU radar are shown by solid lines. Five white circles indicate the locations where the geomagnetic field line connecting to the FAI at an altitude of 105 km pierces through the airglow layer at an altitude of 250 km. (b) Geometry of MU radar and airglow observations in the meridional-altitude plane. Airglow layer of 630 nm is assumed to exist at 250-km altitude. Open circle indicates location connected to the QP echo region at 105-km altitude by the geomagnetic field line.

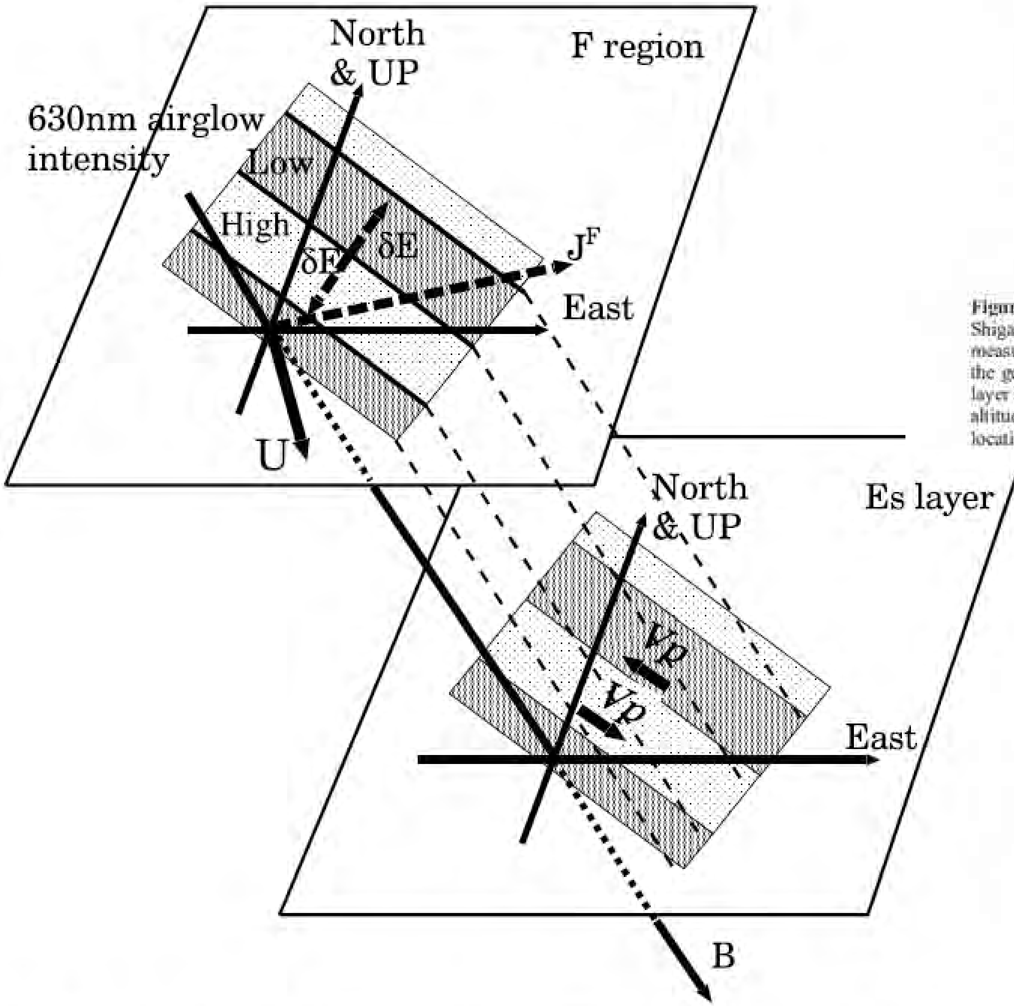

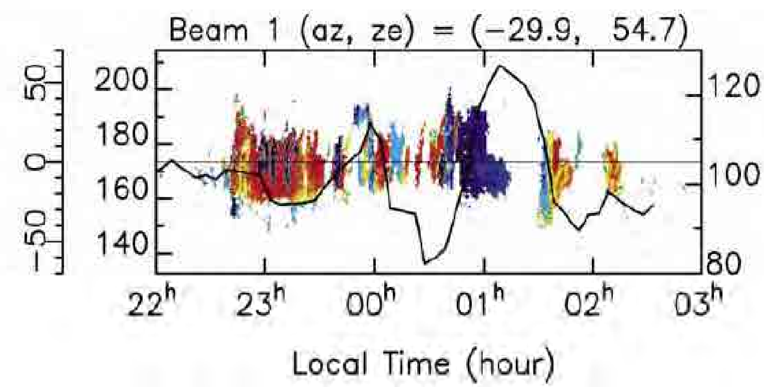

Figure 7. Schematics of observational results of (top) MSTID and (bottom) *E* region FAI obtained from airglow and MU radar measurements on the night of 6 August. Top: Airglow perturbations caused by the MSTID have a wavefront aligned from northwest to southeast and propagate southwestward. Neutral wind (**U**) blows south-southeastward. Pedersen current ($\mathbf{J}^F$) and polarization electric field (δE), which are expected from the above observations, are also displayed in the figure. Bottom: Drift velocity (V_p) of the FAI is southeastward (northwestward) at the region connected to the high (low) airglow intensity region by the geomagnetic field (**B**).

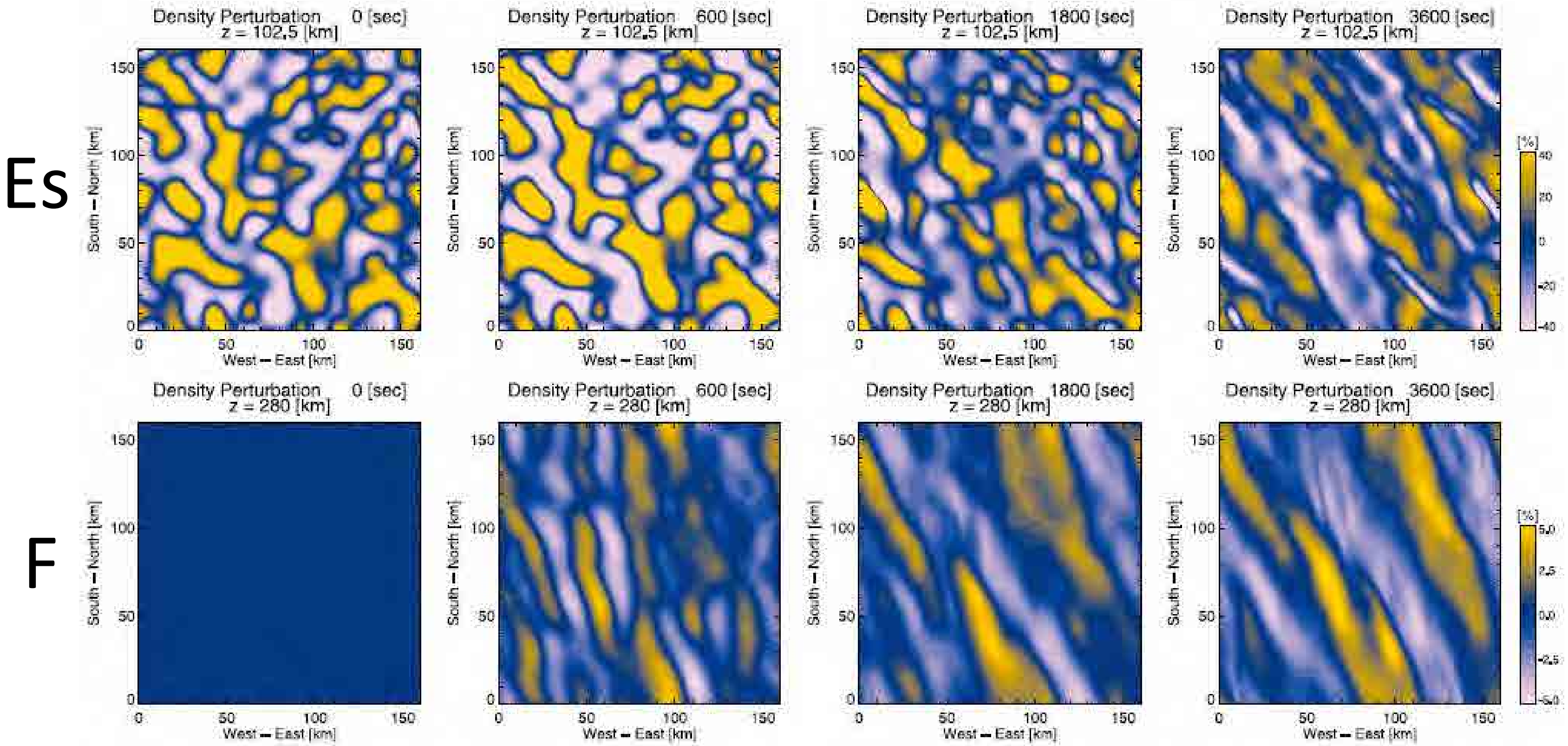

Figure 11. Plasma density perturbation at altitudes of (top) 102.5 and (bottom) 280 km at $t = 0$, 600, 1800, and 3600 s in case RP1. The top images are shifted along the meridional direction so that the same coordinate points are connected by **B**.

Yokoyama et al. (JGR, 2009) Simulation of coupling between E and F layers

- **Es layer creates the seed of instability, and Perkins in F-region amplify it to create MSTIDs**
- **The southward neutral wind in the Es layer makes everything propagate southward.**

scale length. We conclude that (1) the E_s-layer instability plays a major role in seeding NW-SE structure in the F region, and the Perkins instability is required to amplify its perturbation; (2) the rotational wind shear in the E region produces southwestward phase propagation of the NW-SE structure in both the E and F regions; and (3) the coupling process has a significant effect on the scale of the E_s-layer perturbation rather than the growth rate of the E_s-layer instability.

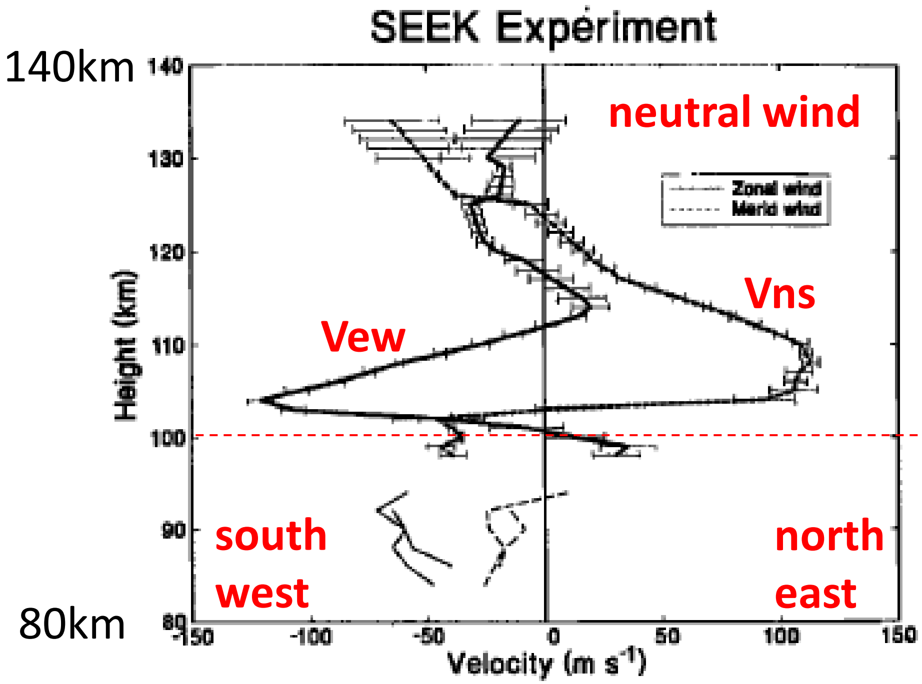

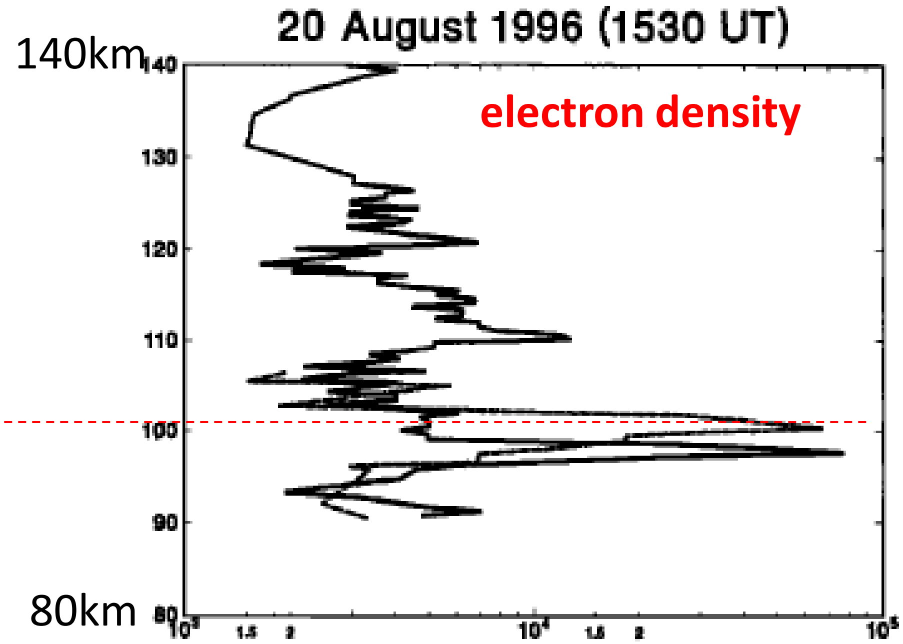

Figure 2. Chemical release wind profile on August 1996, at 1530 UT. The zonal wind is shown as the hea solid line and the meridional wind profile as the hea dashed line. The Yamagawa medium frequency radar wind profiles are shown as as the thin lines. Each curve represents a 15 minute average.

Figure 4. Electron density profiles (cm^{-3}) versus altitude (km ... line) por

Larsen et al. (GRL, 1998)

Es layer observation by SEEK rocket campaign

The Es layer is made by tidal wind shear to collect ions in the shear region. The wind becomes southward at the center of the Es layer.

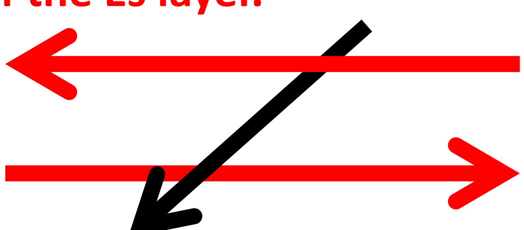

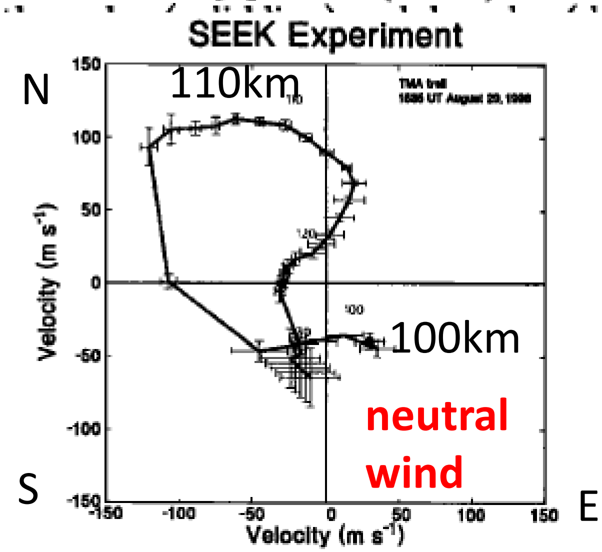

Figure 3. Hodograph of the winds obtained from the chemical release. The altitudes are shown at 10 km intervals above and to the left of the corresponding points.

Inter-hemispheric coupling through nighttime MSTIDs at middle latitudes

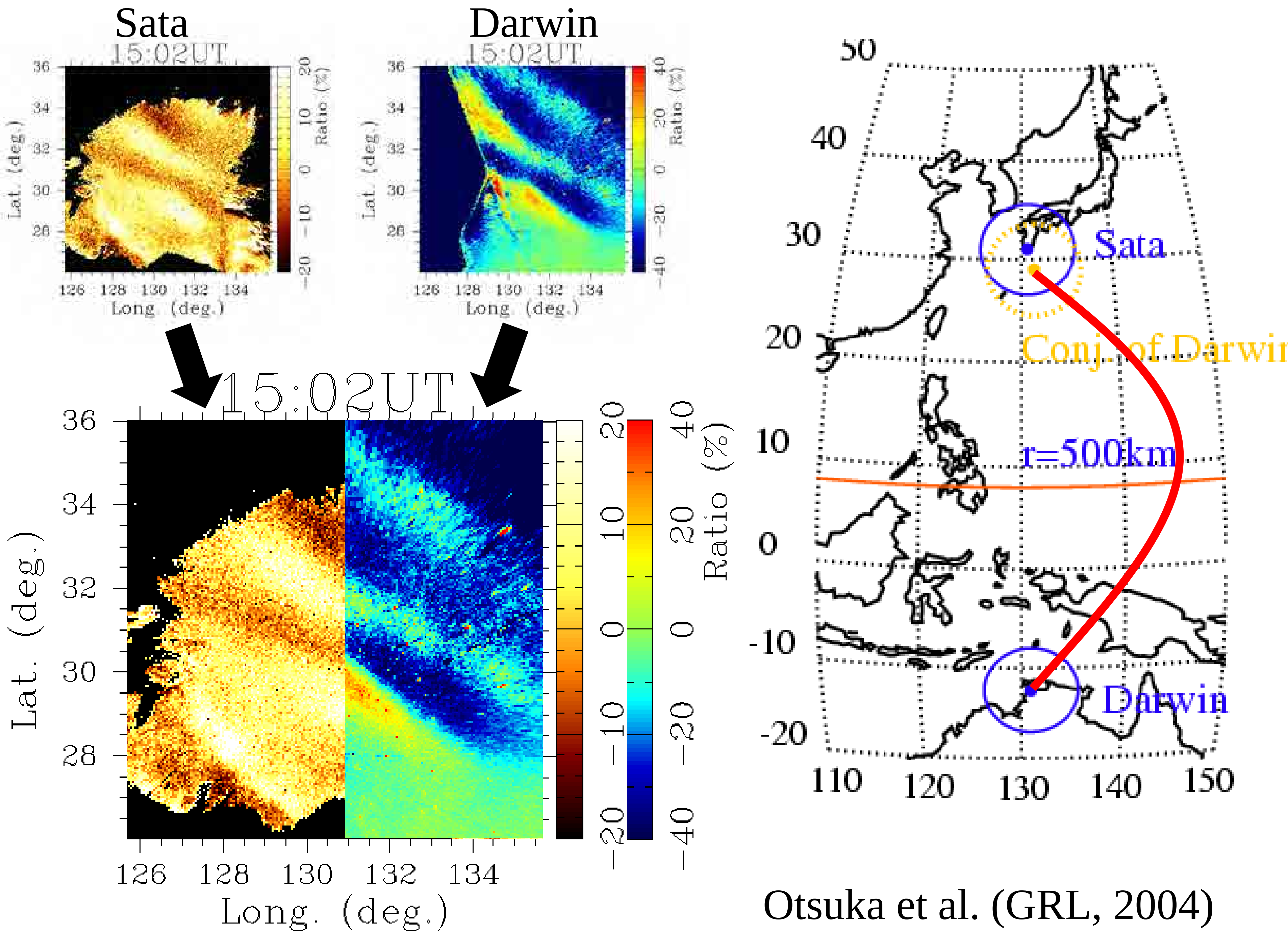

Otsuka et al. (GRL, 2004)

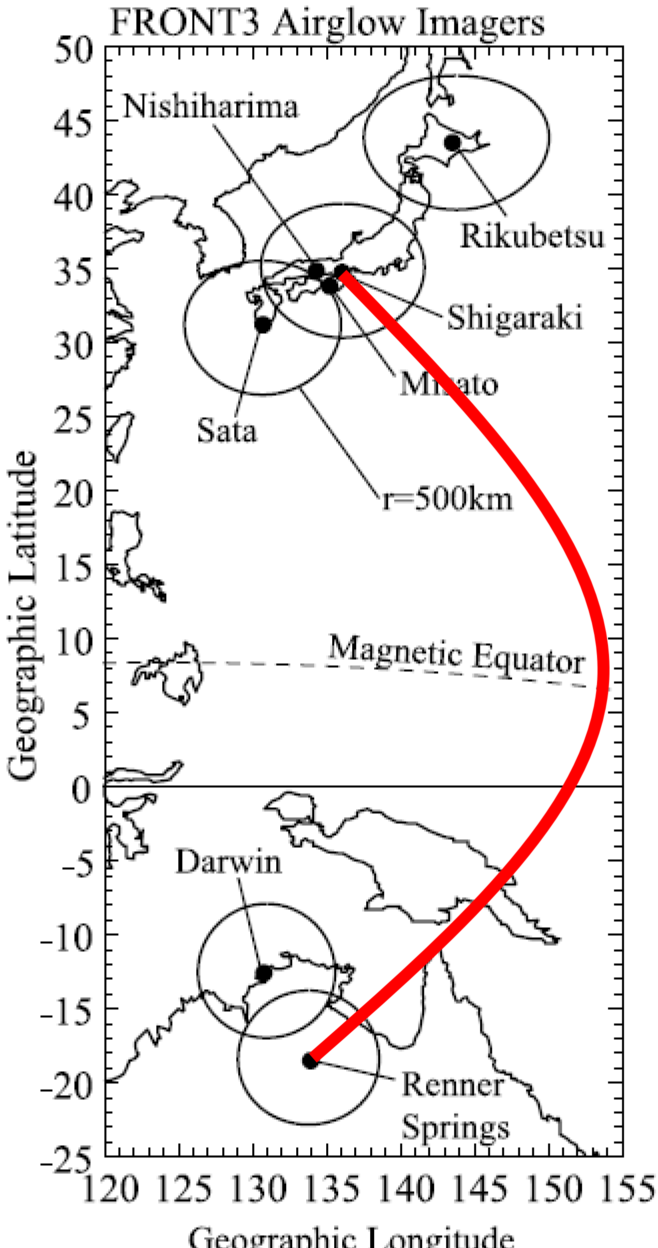

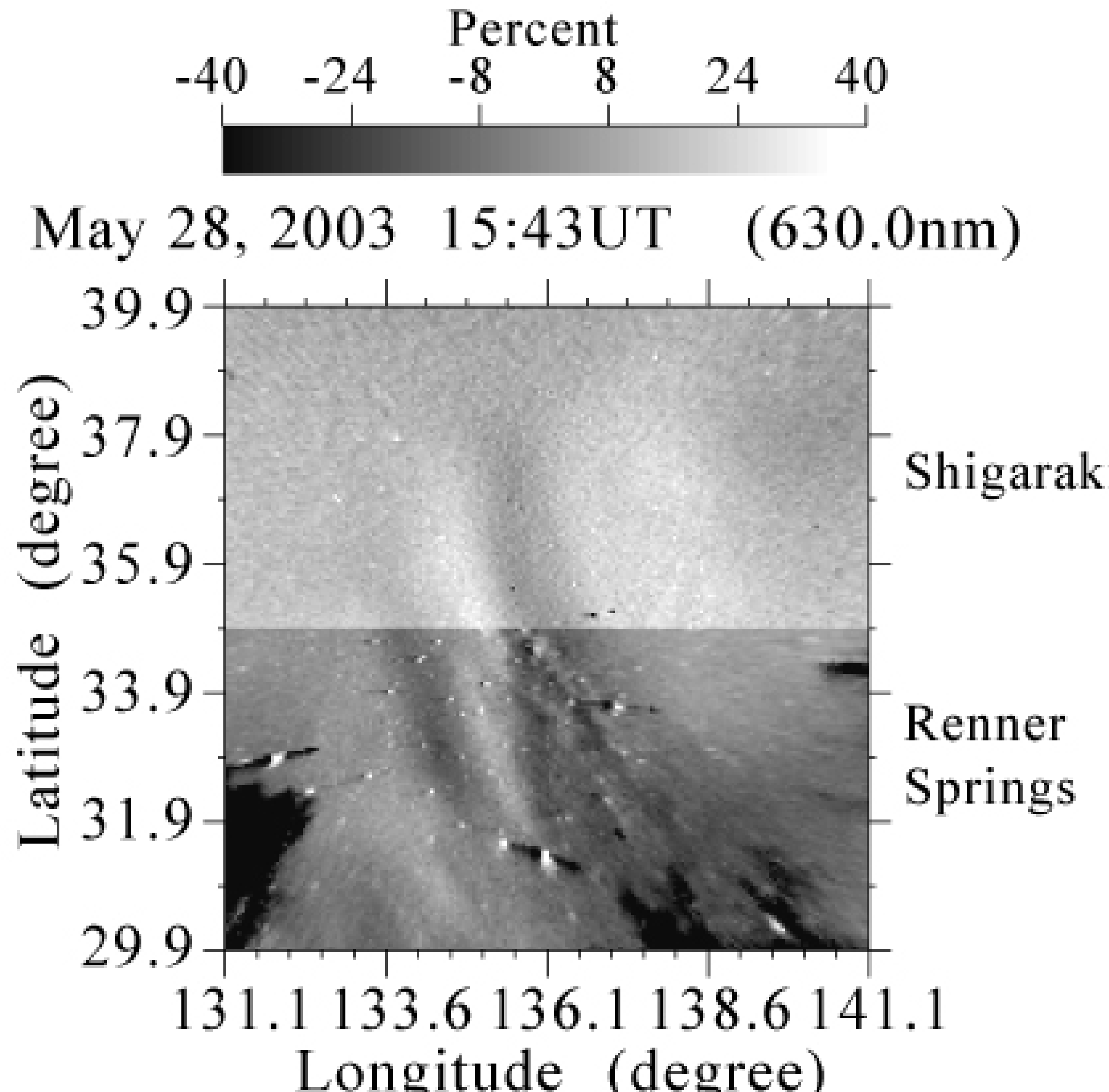

Shiokawa et al. (JGR, 2005)

conjugate FPIs+ imagers + radars + satellites + ionosondes + GPS receivers

= coupling processes (E and F layers and two hemispheres)

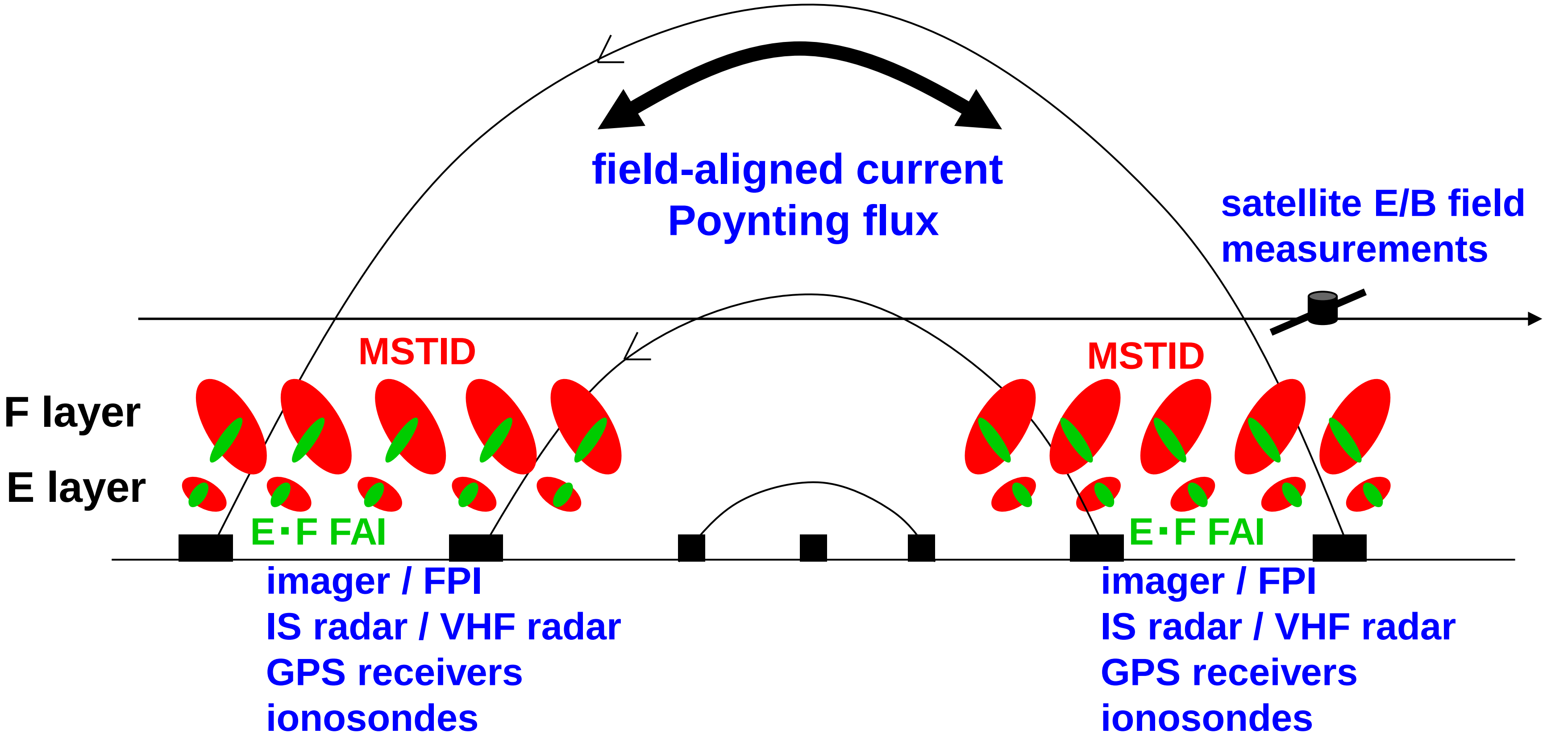

Narayanan et al. (JGR, 2018)

When the Electrified MSTIDs are observed by airglow imagers, Es layer is active at least one of the two hemispheres. Es layer is the dominant controlling factor of the generation of nighttime MSTIDs.

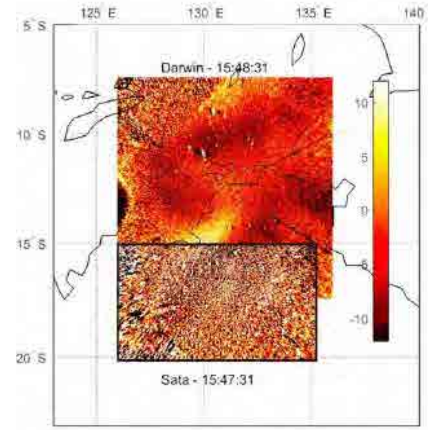

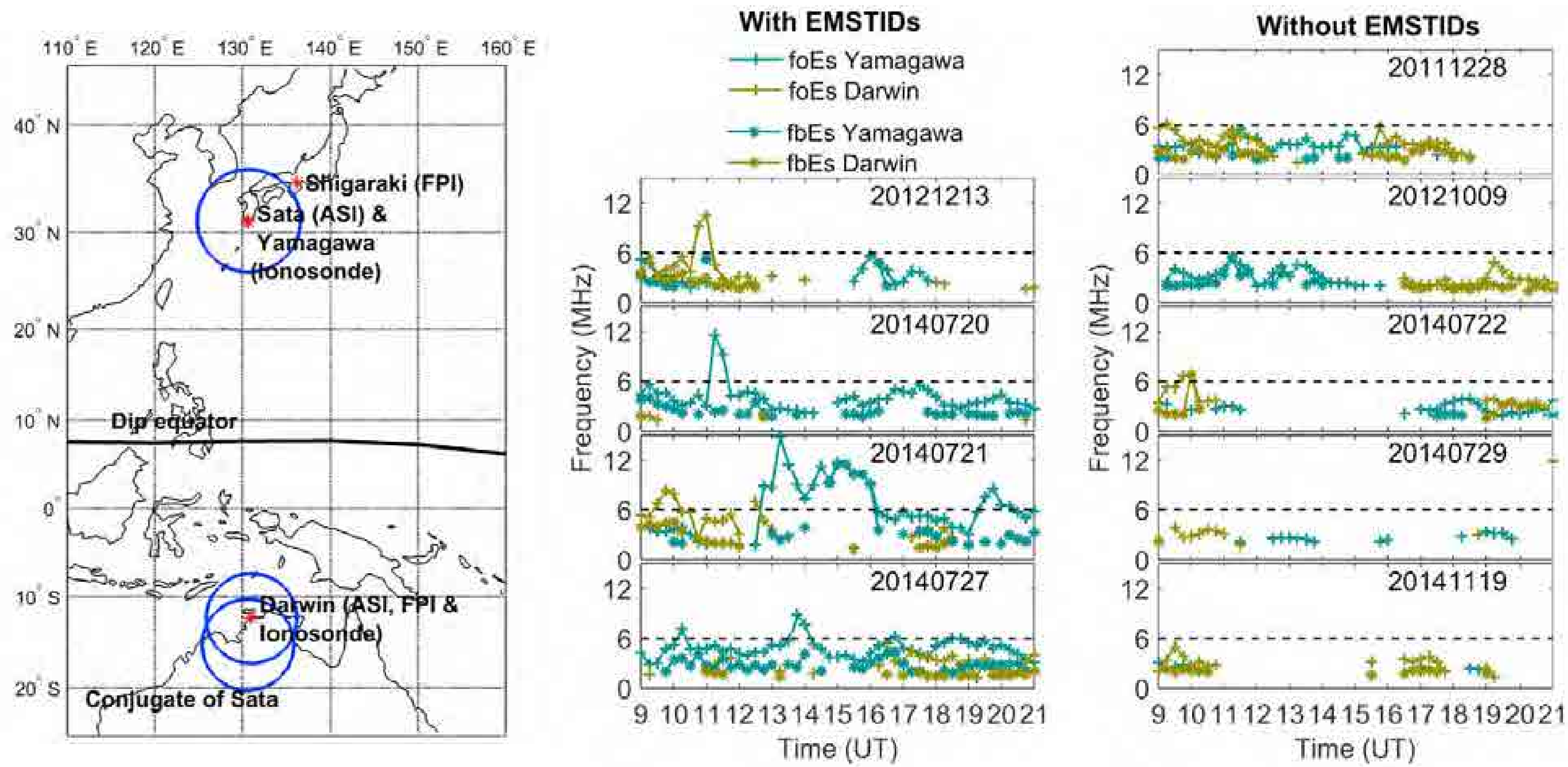

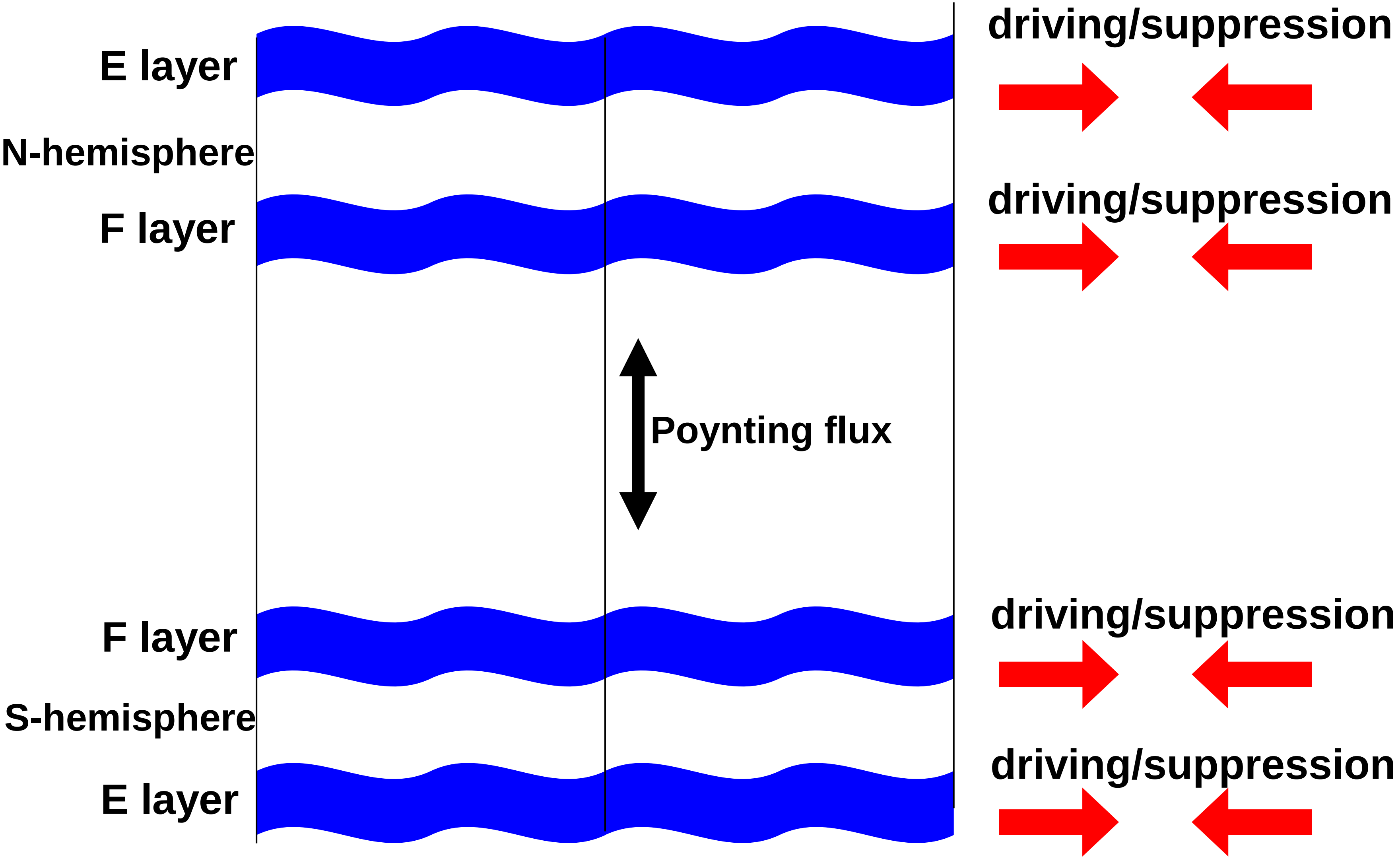

E layer
N-hemisphere
F layer
driving/suppression
driving/suppression
Poynting flux
F layer
S-hemisphere
E layer
driving/suppression
driving/suppression

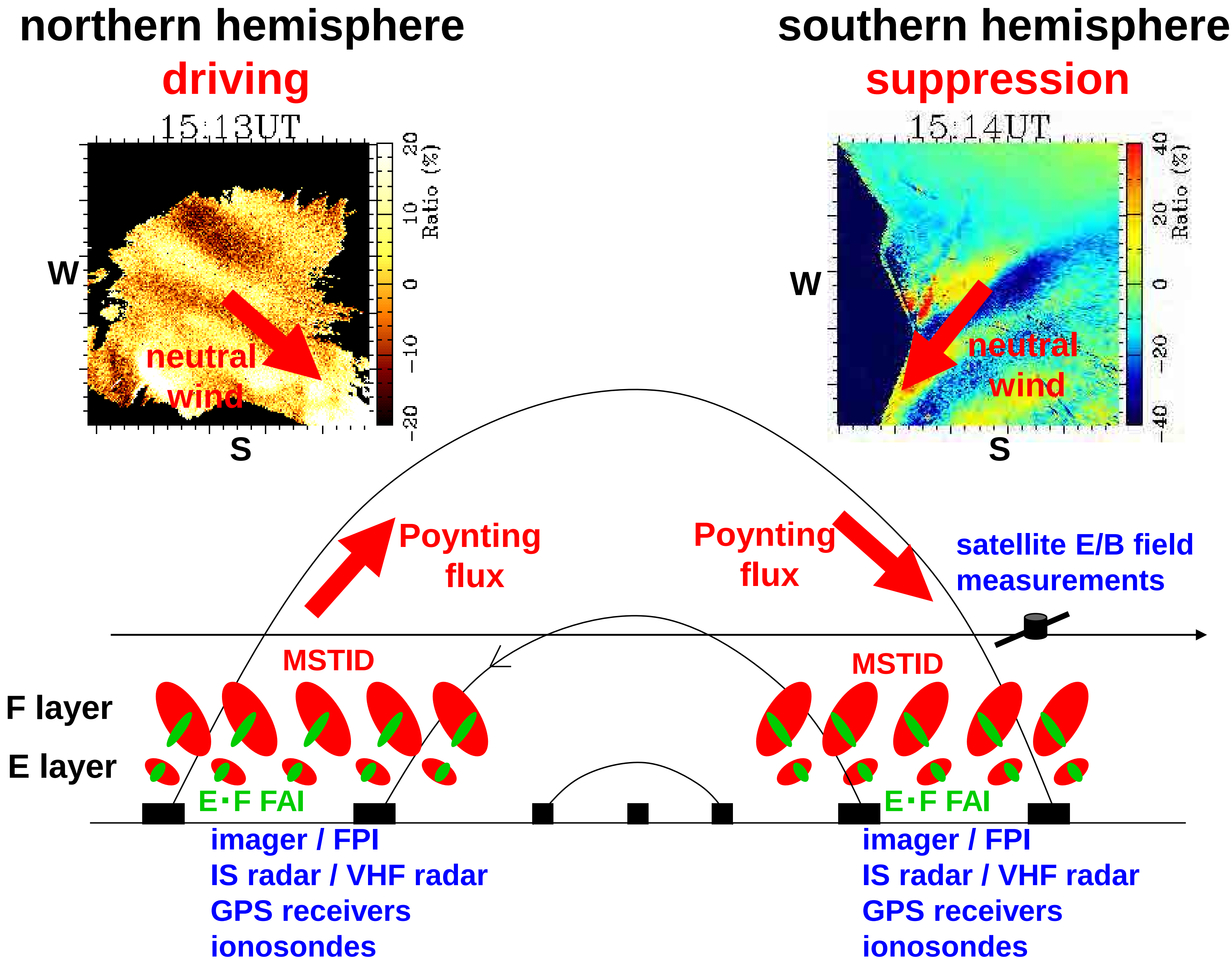
northern hemisphere
driving
15:13UT
20
10
0
−10
−20
Ratio (%)
W
S
neutral wind
southern hemisphere
suppression
15:14UT
40
20
0
−20
−40
Ratio (%)
W
S
neutral wind
Poynting flux
Poynting flux
satellite E/B field measurements
MSTID
MSTID
F layer
E layer
E·F FAI
E·F FAI
imager / FPI
IS radar / VHF radar
GPS receivers
ionosondes
imager / FPI
IS radar / VHF radar
GPS receivers
ionosondes

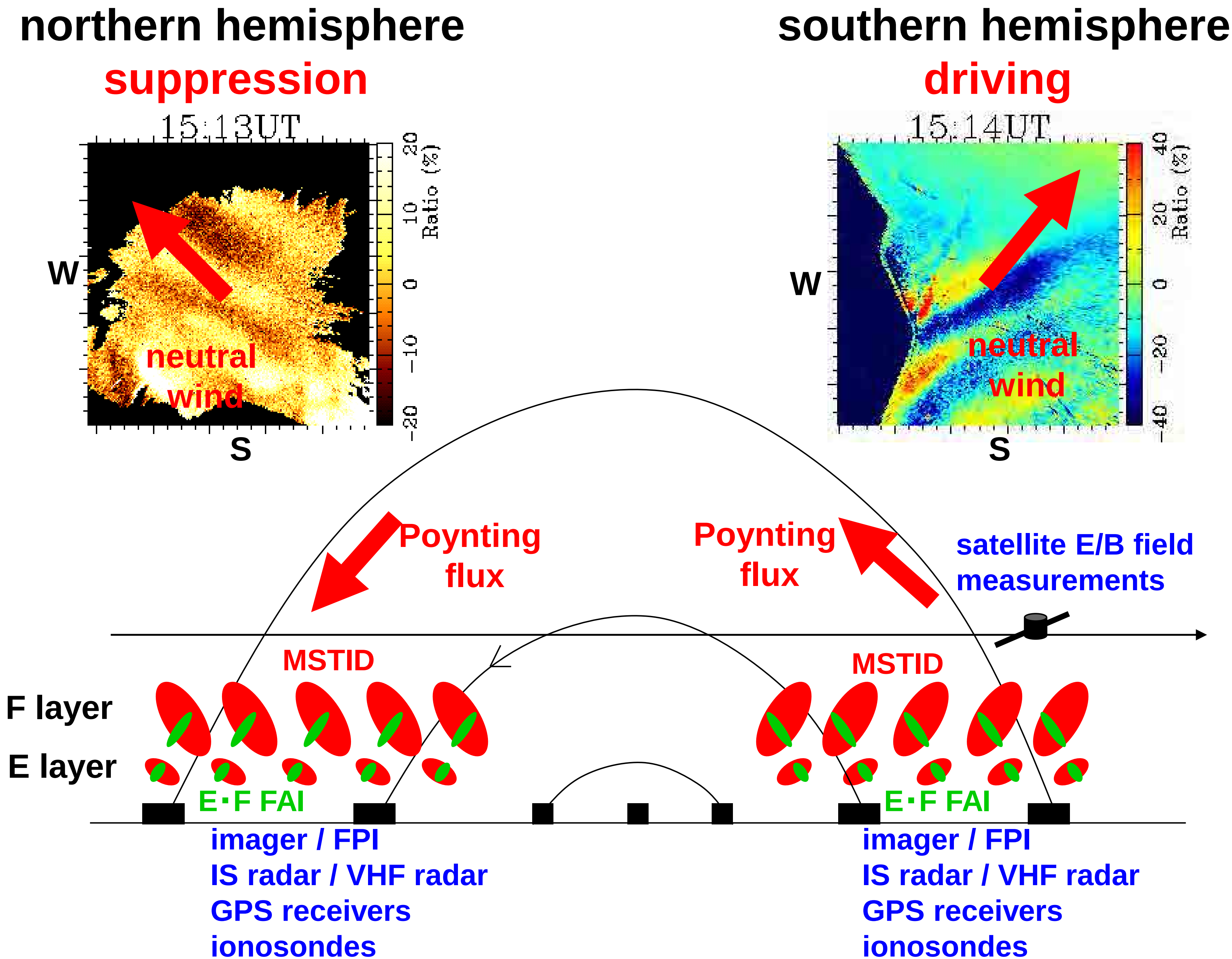

northern hemisphere
suppression
15:13UT
W
S
neutral wind
Ratio (%)
20
10
0
−10
−20
southern hemisphere
driving
15:14UT
W
S
neutral wind
Ratio (%)
40
20
0
−20
−40
Poynting flux
Poynting flux
satellite E/B field measurements
MSTID
MSTID
F layer
E layer
E·F FAI
E·F FAI
imager / FPI
IS radar / VHF radar
GPS receivers
ionosondes
imager / FPI
IS radar / VHF radar
GPS receivers
ionosondes

First ground-satellite measurement of MSTID to find out E-field and density variation in the magnetosphere.

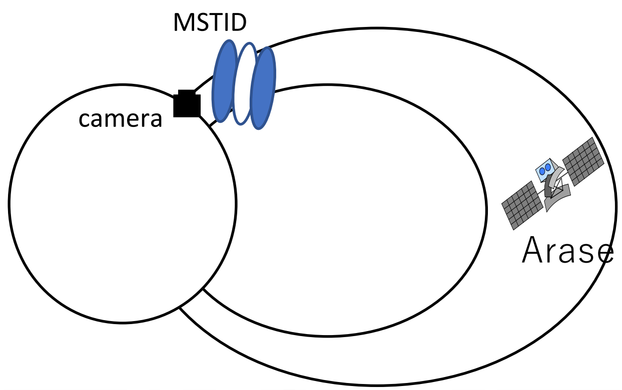

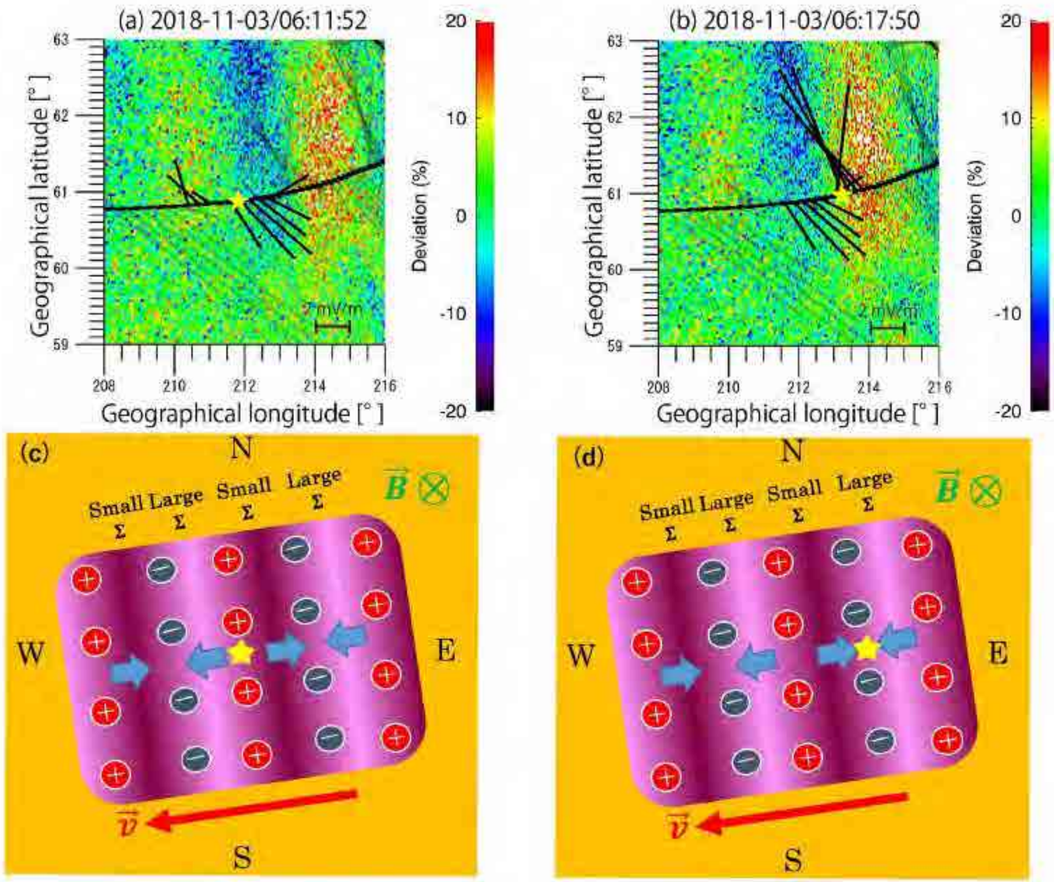

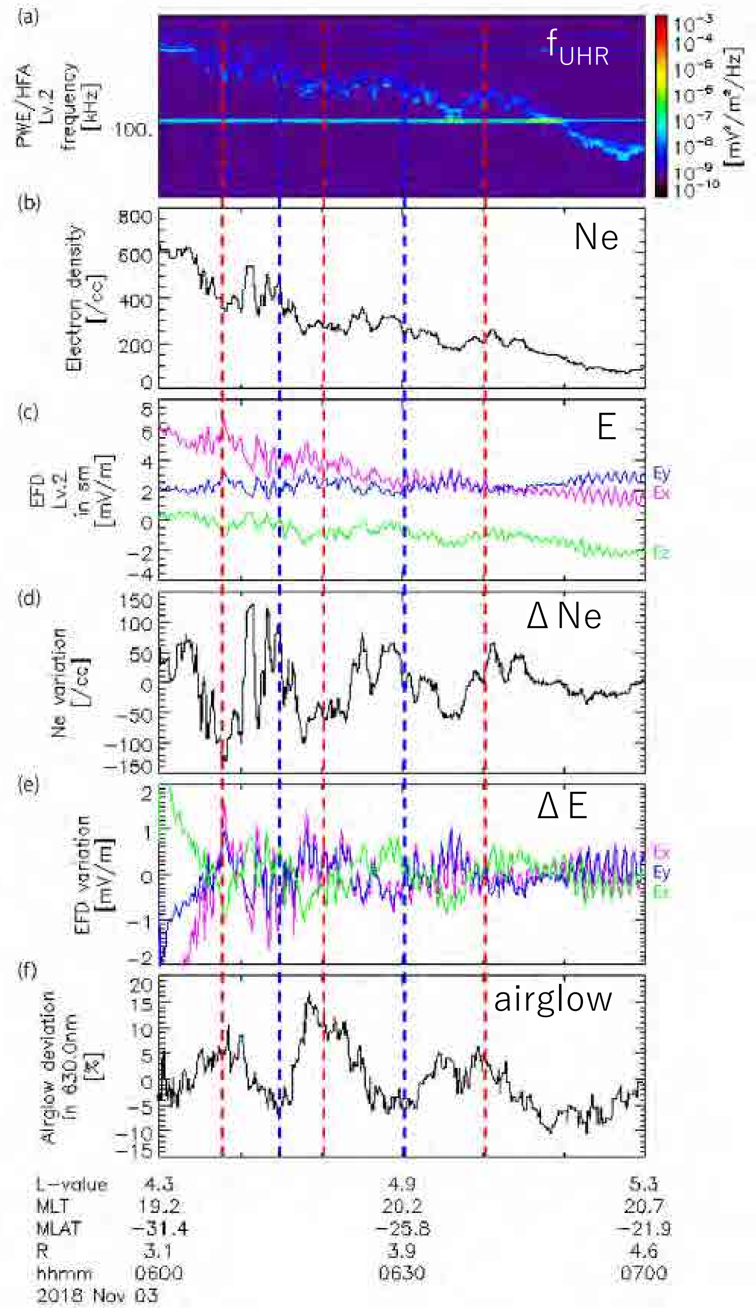

Kawai et al., JGR, 2021, https://doi.org/10.1029/2020JA0290862021

MSTID signatures in the electric field fluctuations observed by DE-2

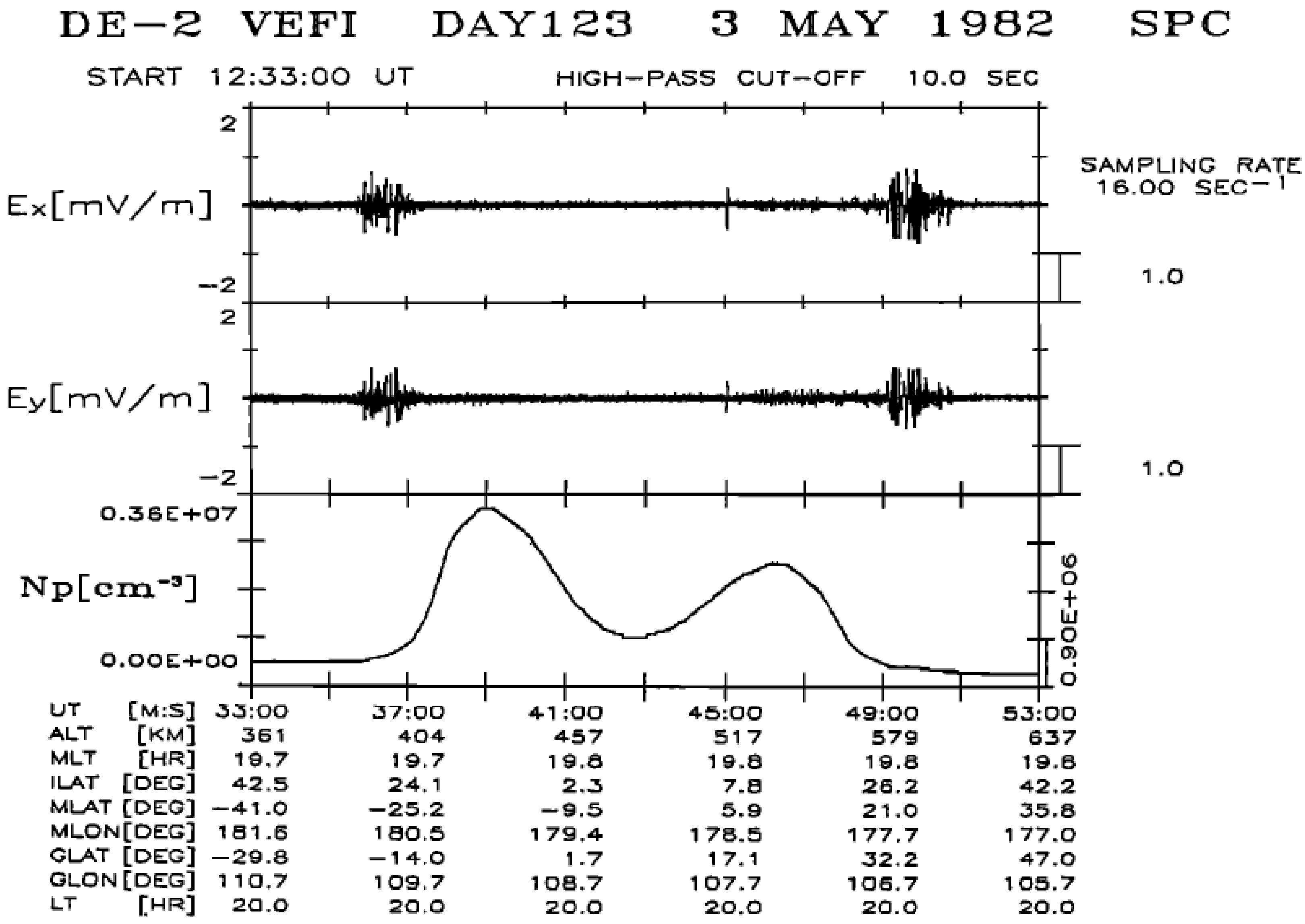

Saito et al. (JGR, 1995)

MSTID signatures in the magnetic field fluctuations observed by CHAMP

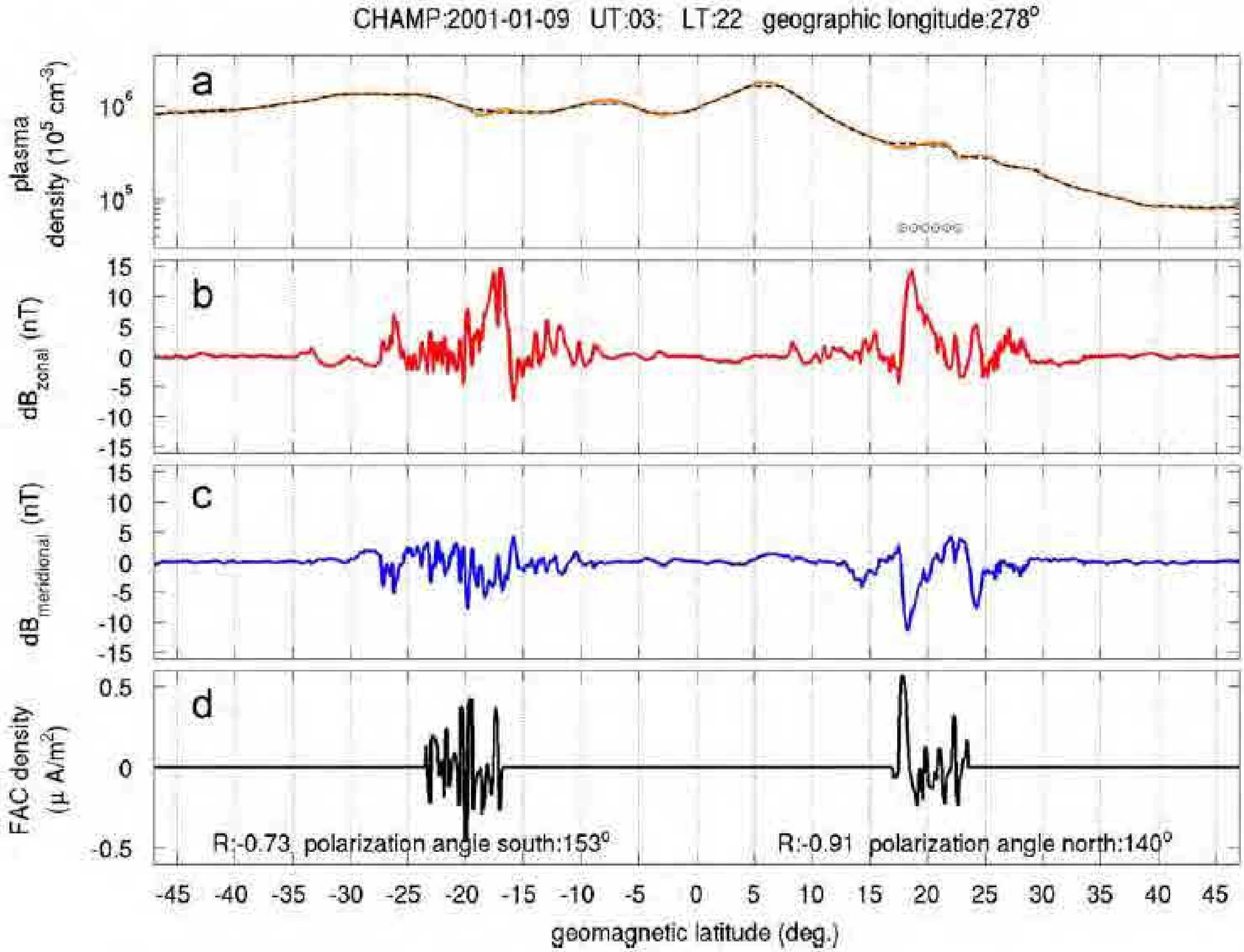

Park et al. (JASTP, 2010)

MSTID signatures in the magnetic field fluctuations observed by CHAMP

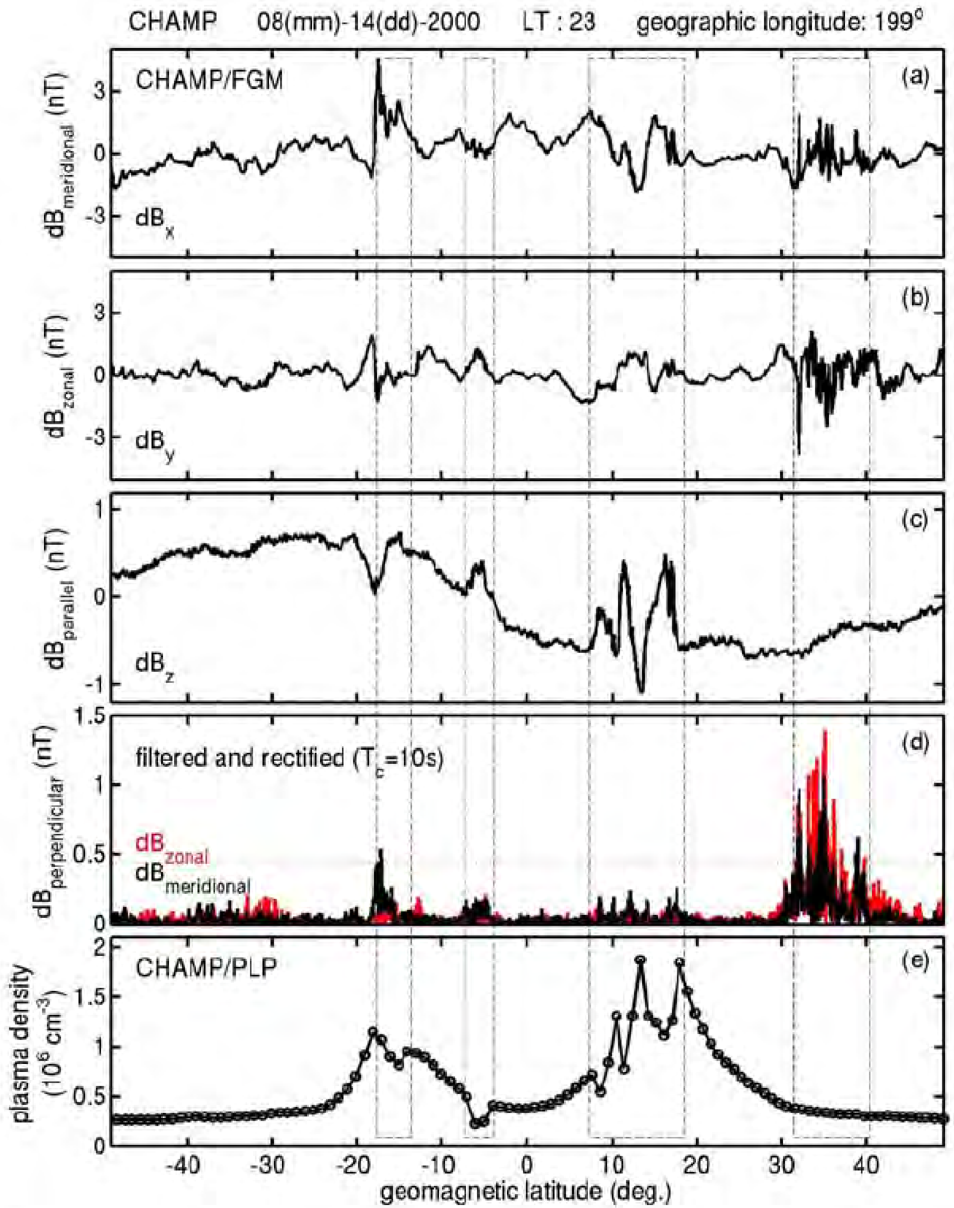

typical example of midlatitude magnetic field fluctuation (MMF) at ~32°–42° latitude. respective components of residual magnetic field in mean-field-aligned coordinates. meridional components which have been high-pass filtered with a cutoff period of 10 s and (e) Plasma density measured by CHAMP/PLP.

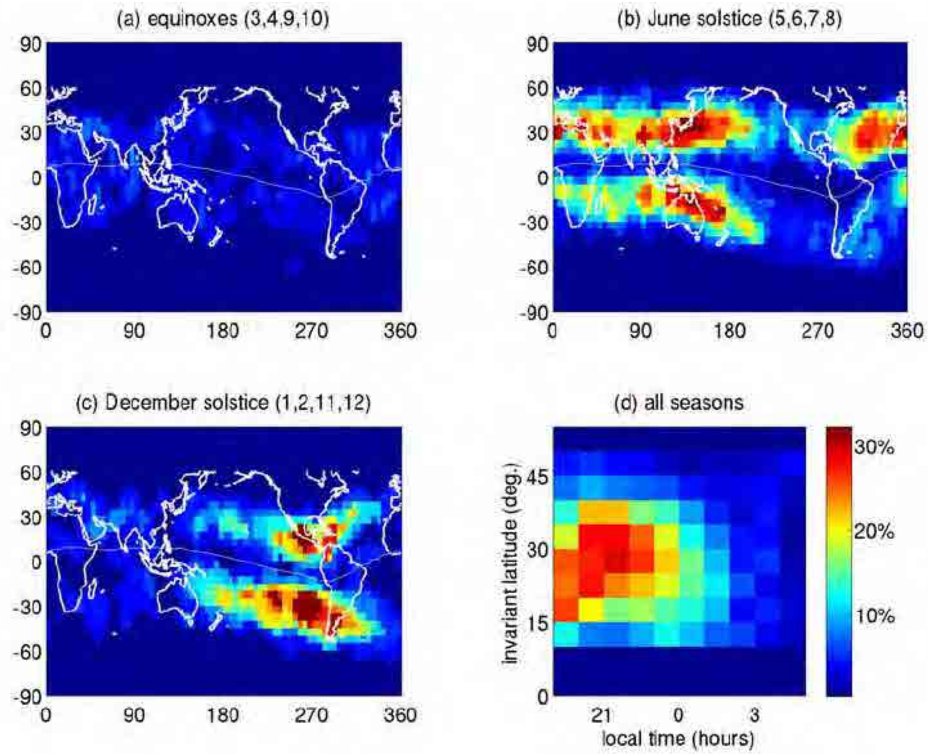

Park et al. (JGR, 2009)

Clear anti-correlation between solar activity and nighttime MSTIDs

Shigaraki

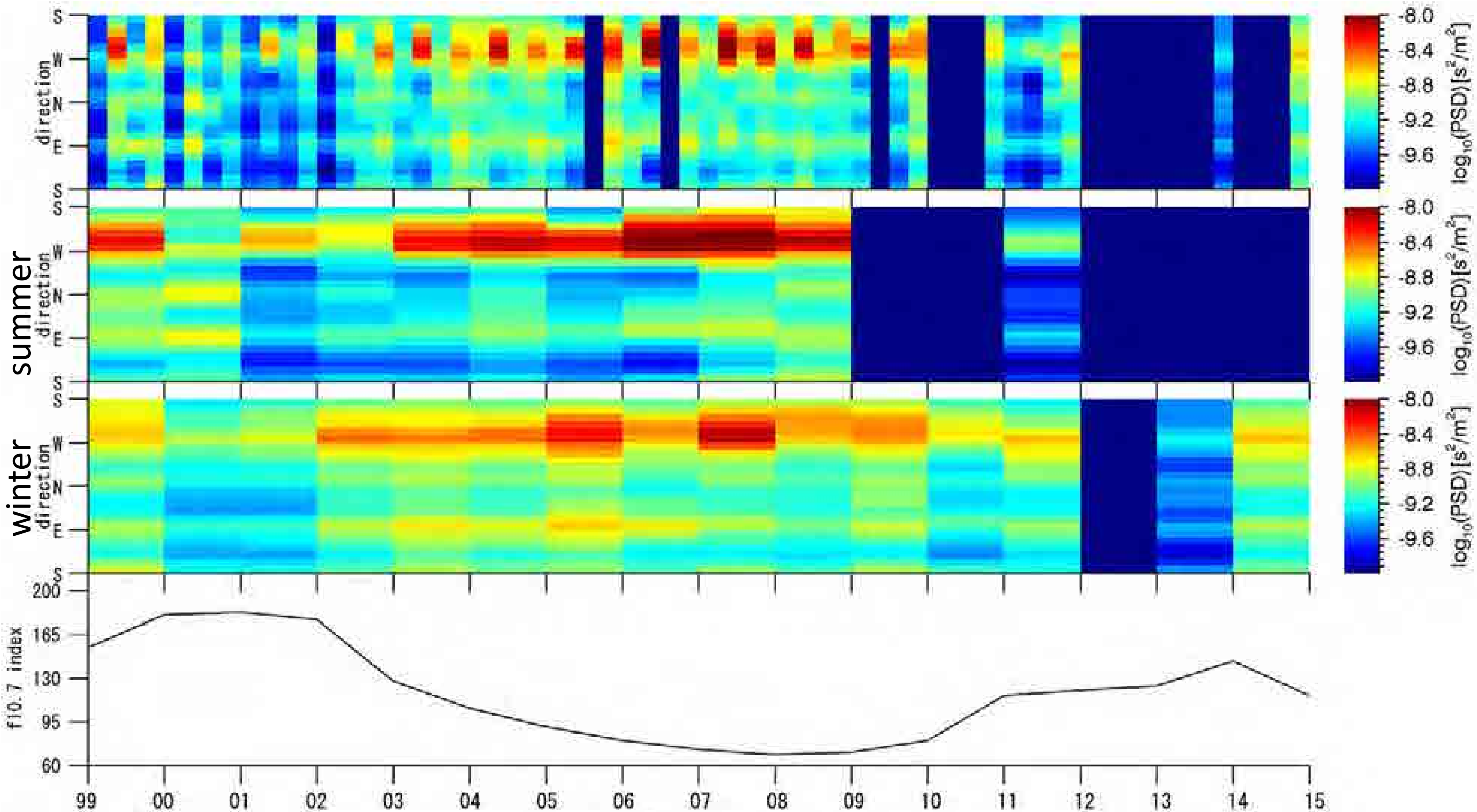

Takeo et al. (JGR, 2017)

Growth rate of Perkins Instability $\gamma = \frac{g \sin^2 I}{\langle \nu_{in} \rangle H_n} \frac{\sin \alpha \sin(\theta^* - \alpha)}{\cos \theta^*}$

ν_{in} is large at high solar activity

Global distribution of nighttime MSTIDs - equatorial side -

Nighttime MSTID direction (summary)

summer
winter

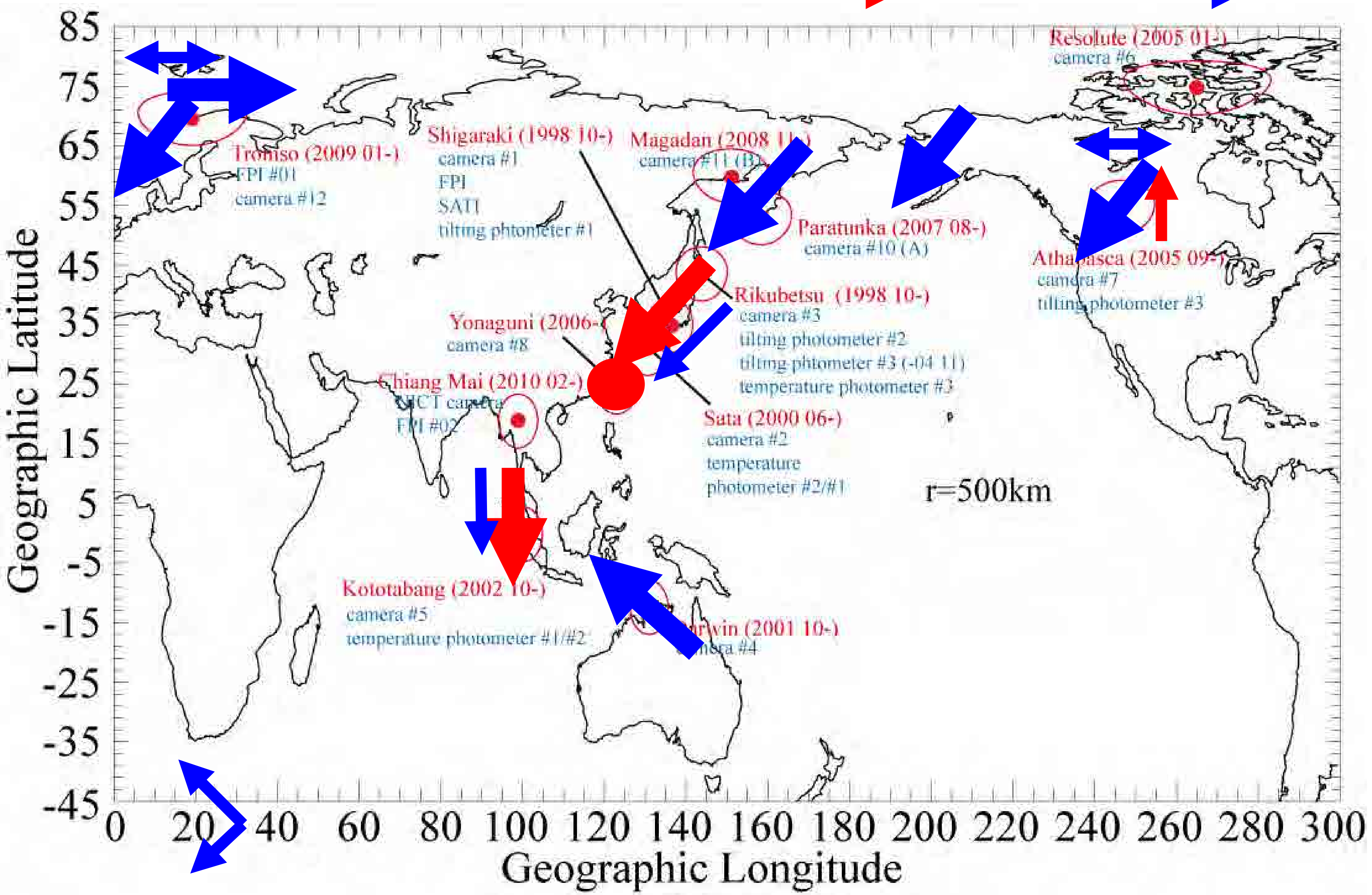

Low-latitude boundary of mid-latitude MSTIDs

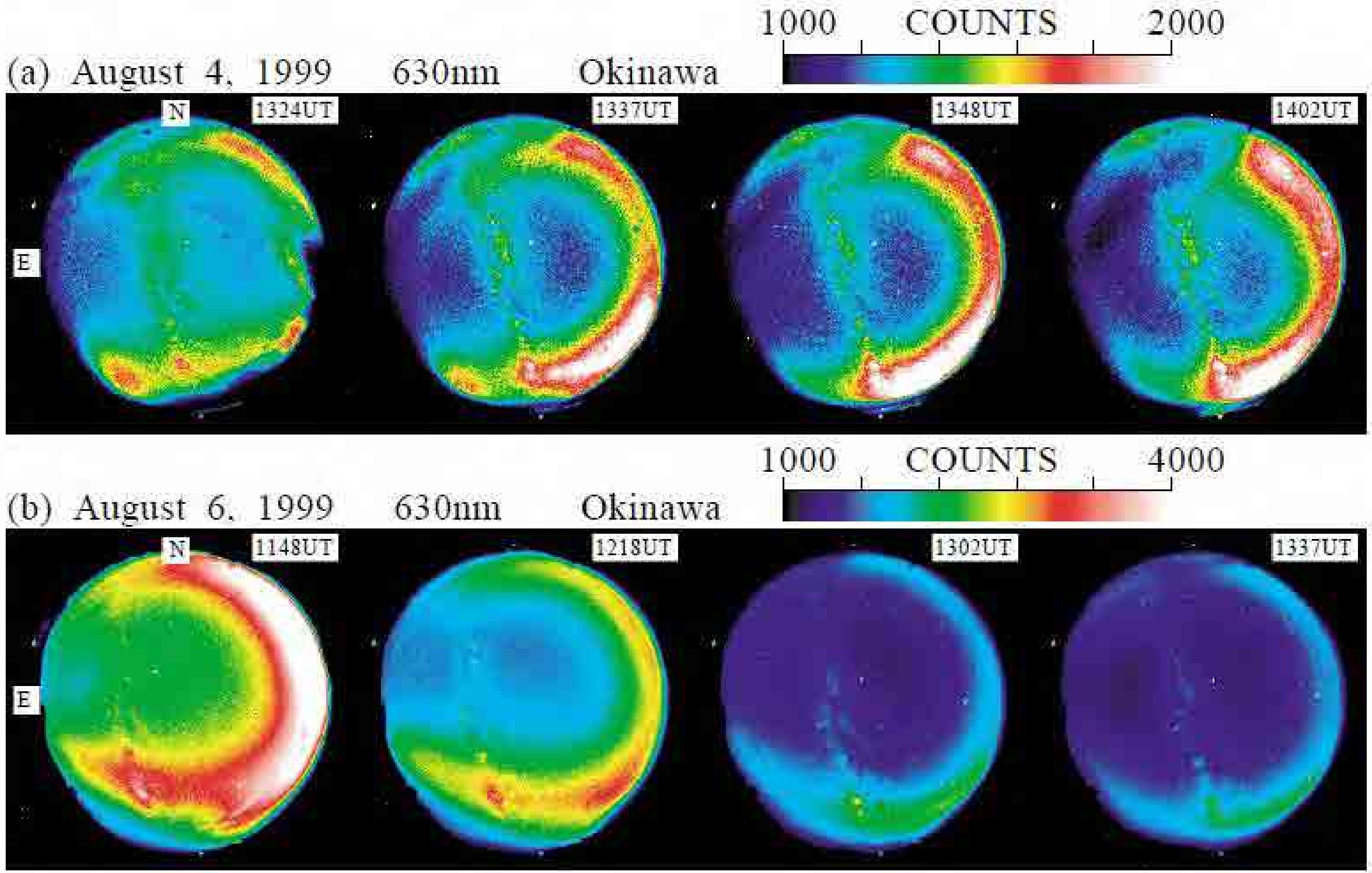

MSTIDs observed (top) and not observed (bottom) at Okinawa (MLAT=18N) . For the bottom case, the equatorial anomaly was observed in the south.
→ Equatorial anomaly crest can be a boundary of mid-latitutde nighttime MSTIDs.

Shiokawa et al. (EPS, 2002)

Low-latitude boundary of mid-latitude MSTIDs

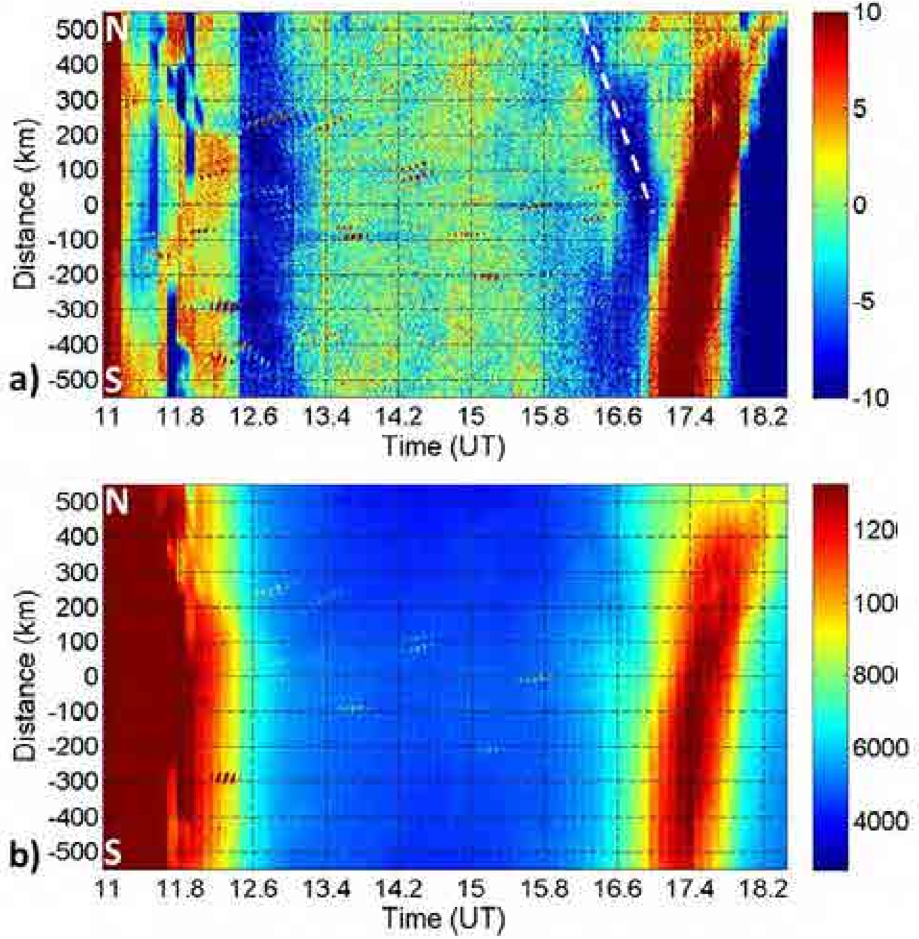

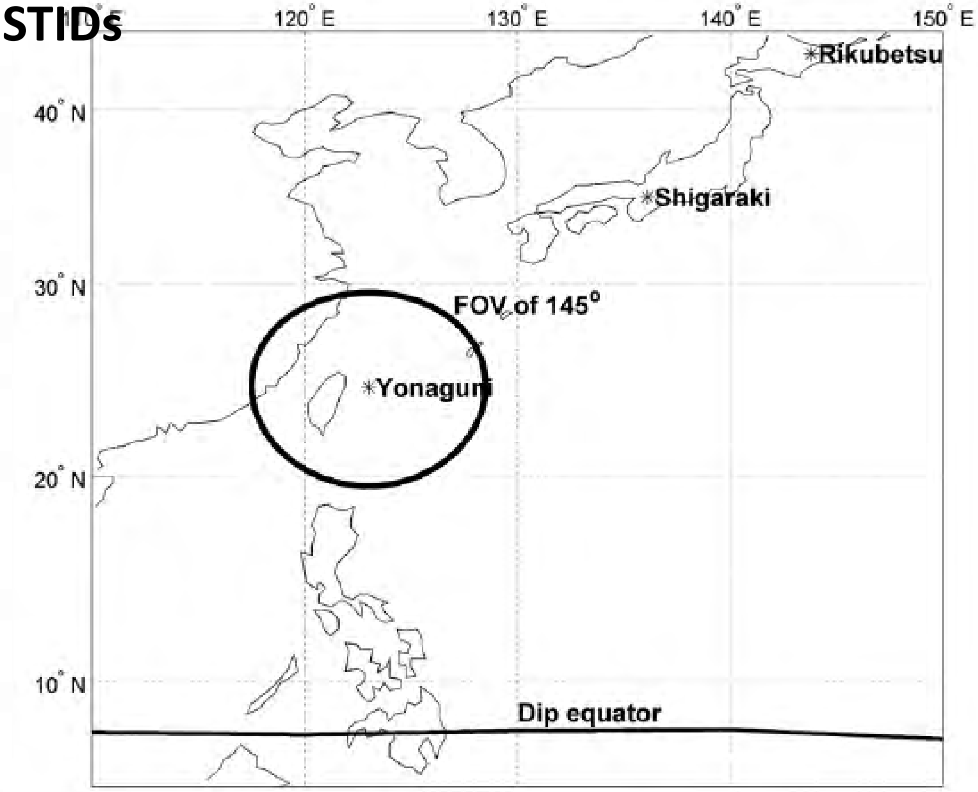

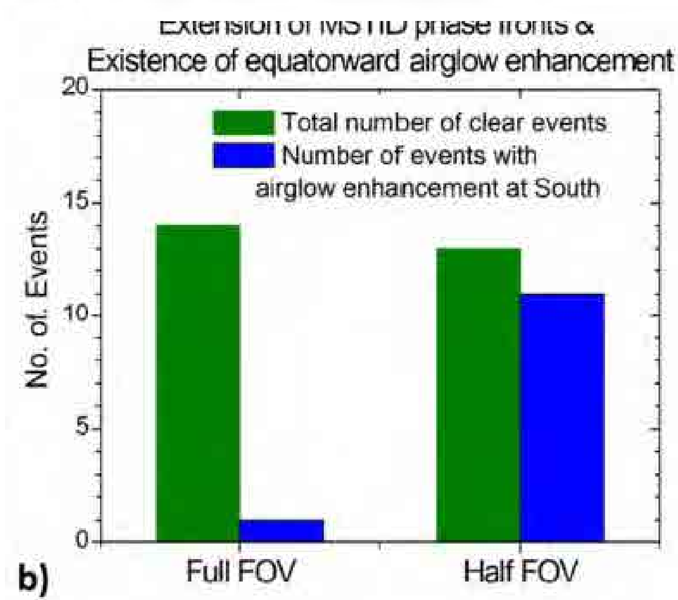

Equatorward boundary of nighttime middle-latitude MSTIDs by equatorial airglow enhancement.

Narayanan et al. (JGR, 2015)

Low-latitude boundary of mid-latitude MSTIDs

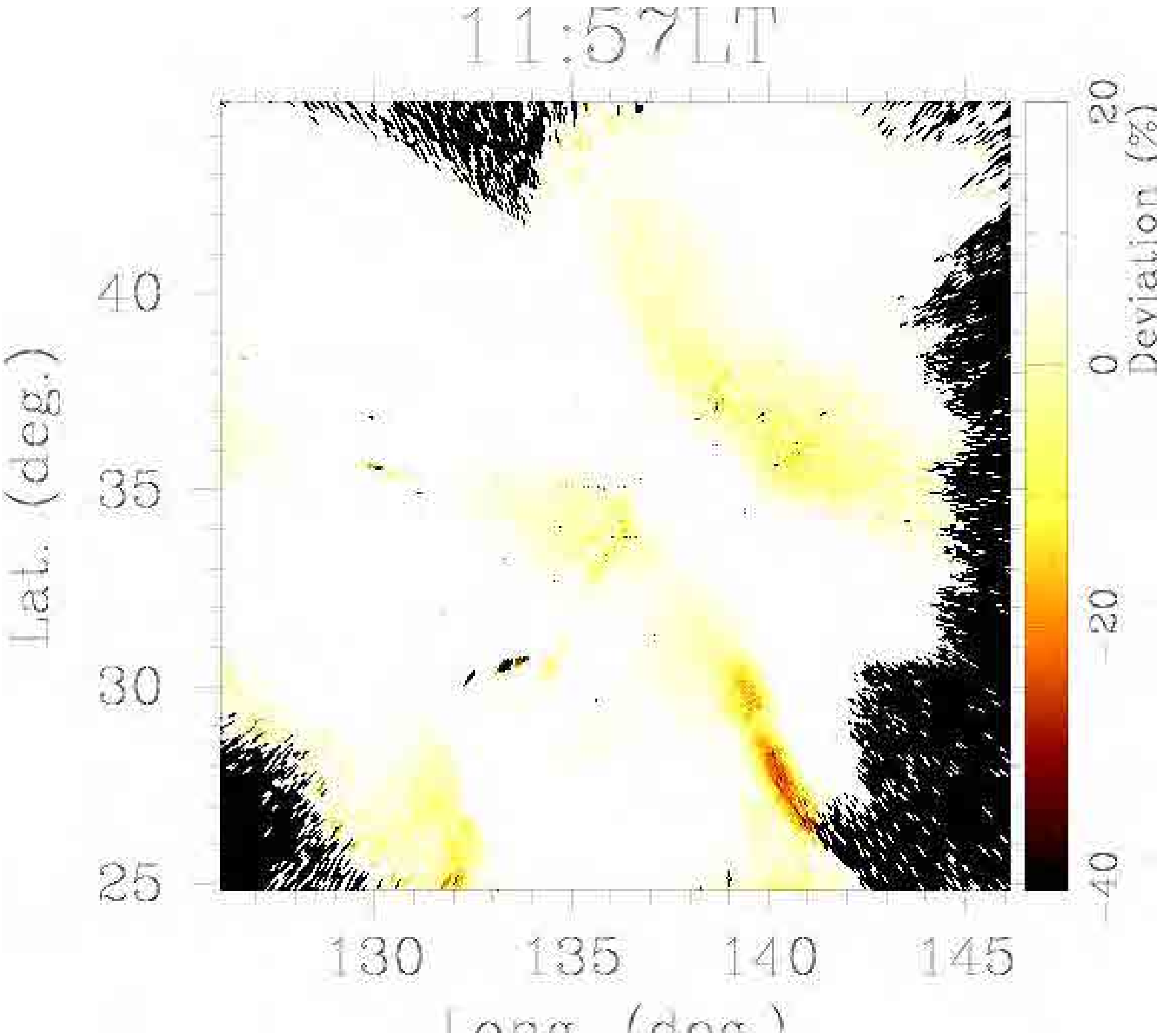

Collision between a nighttime MSTID and a plasma bubble

Otsuka et al. (GRL, 2012)

Nighttime MSTID direction (summary)

summer winter

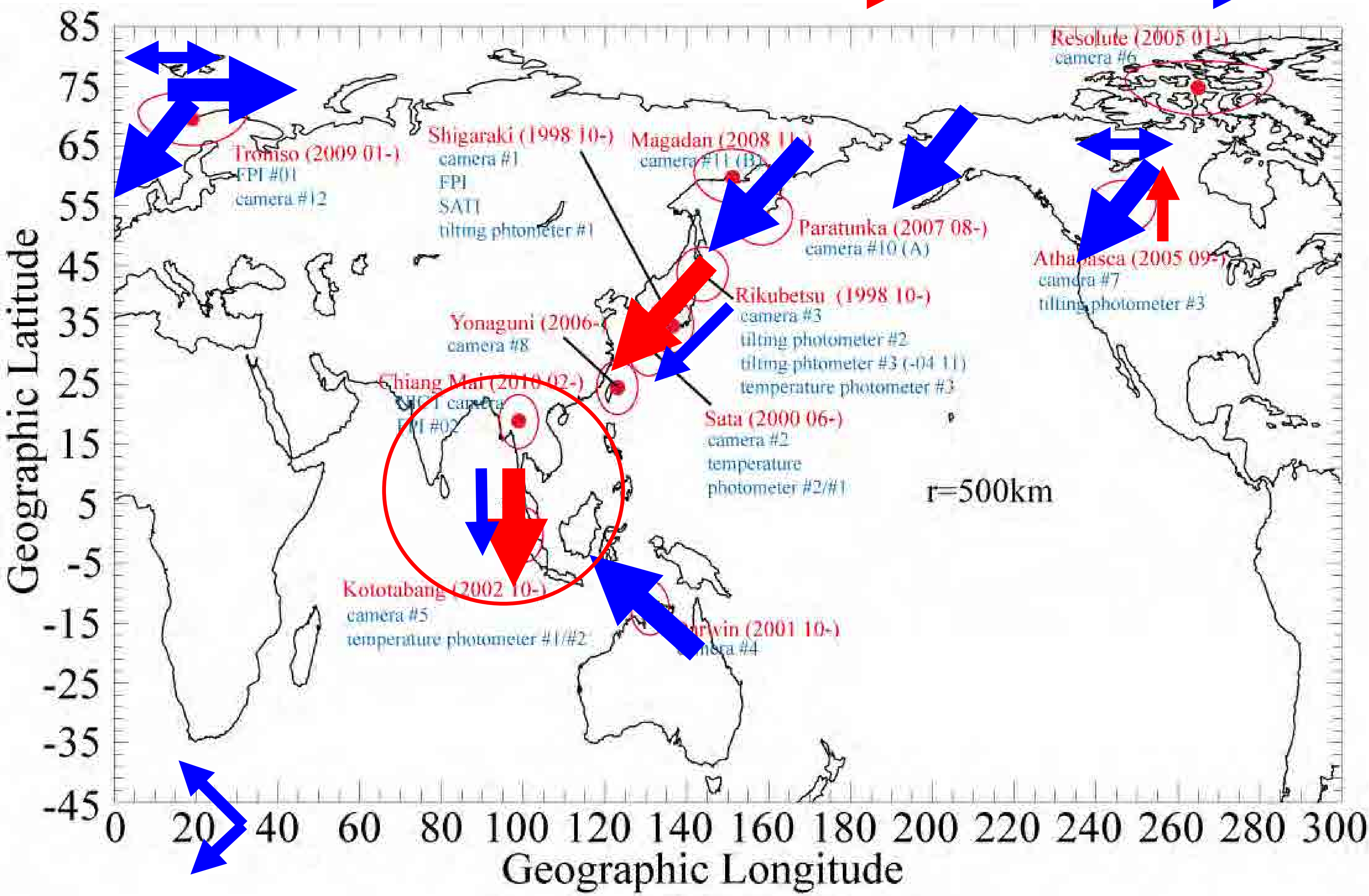

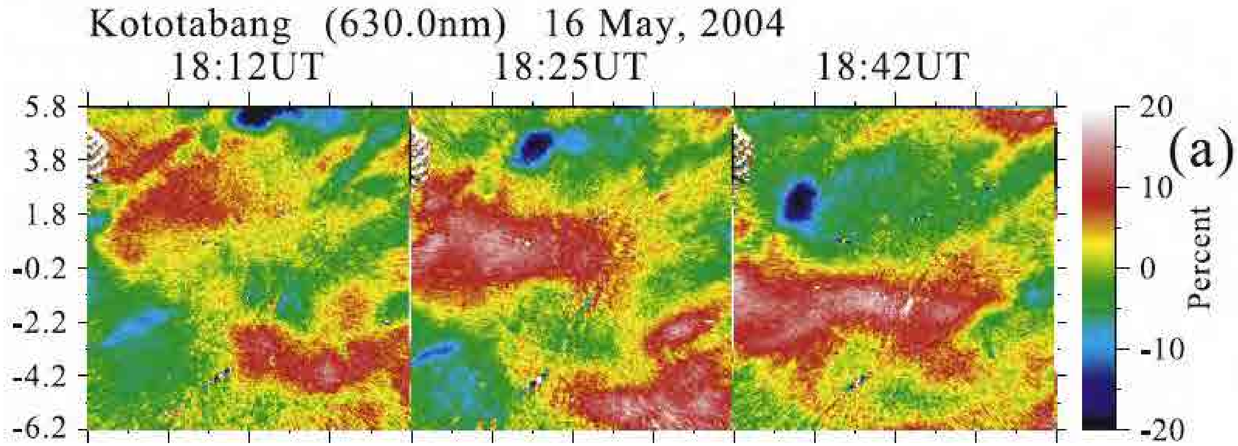

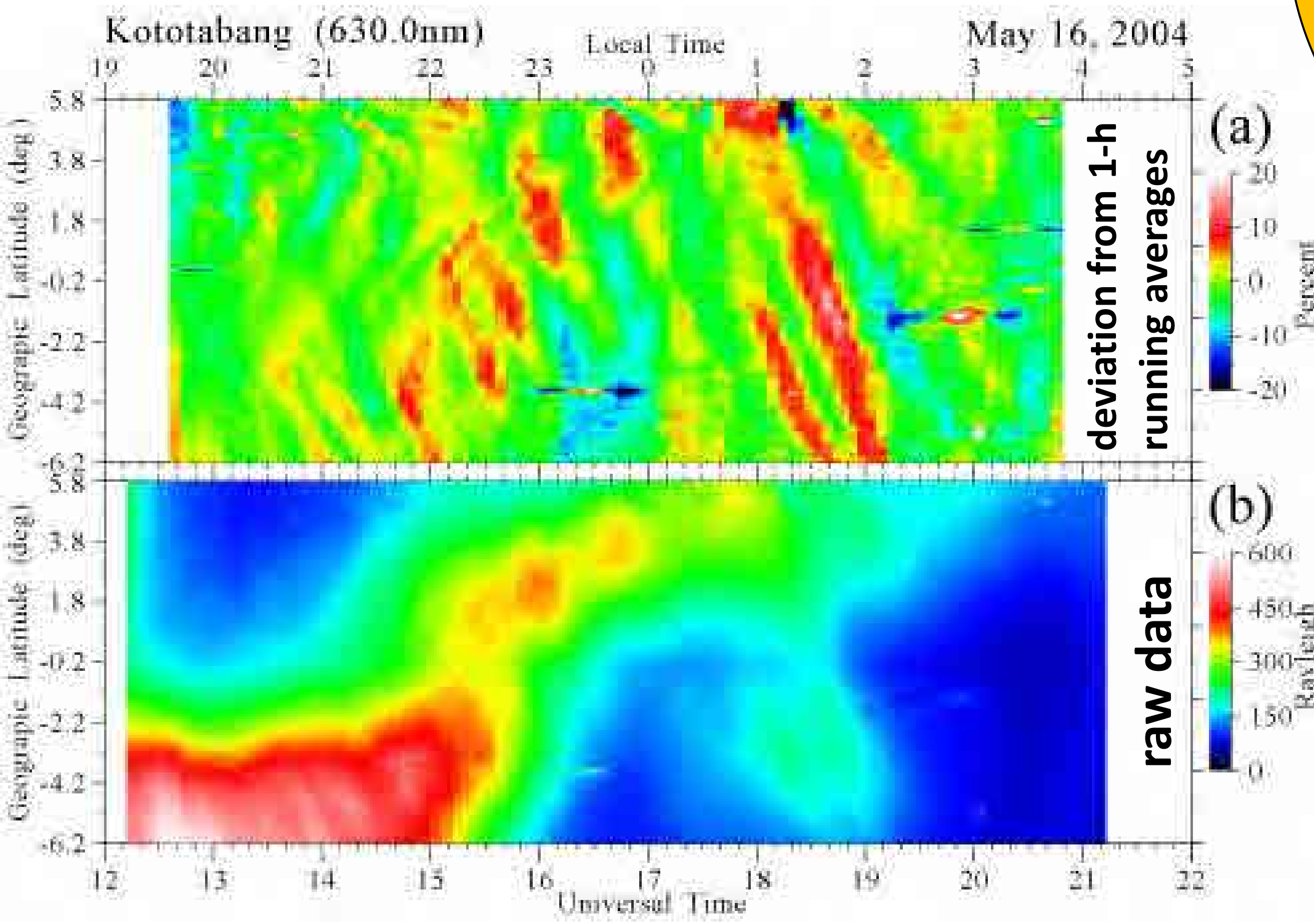

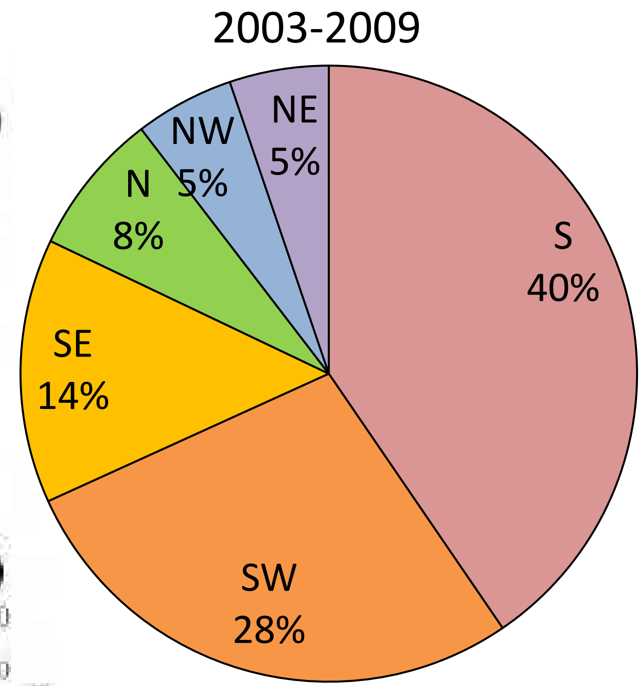

Fukushima et al. (JGR, 2012)

period: ~40min,
phase velocity: ~300m/s
→evanescent in the mesopause region
→ secondary gravity wave?

Shiokawa et al.
(JGR, 2006)

Occurrence of southward-moving MSTIDs at Indonesia (MLAT=10S) → GW-like features

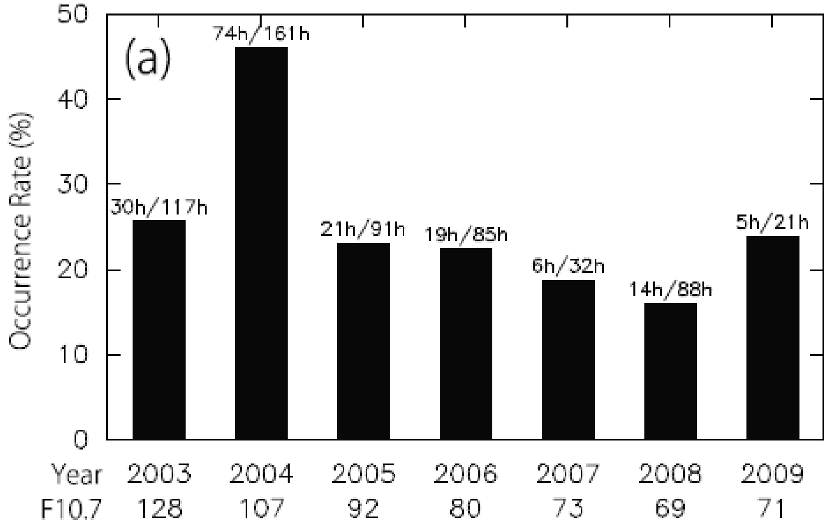

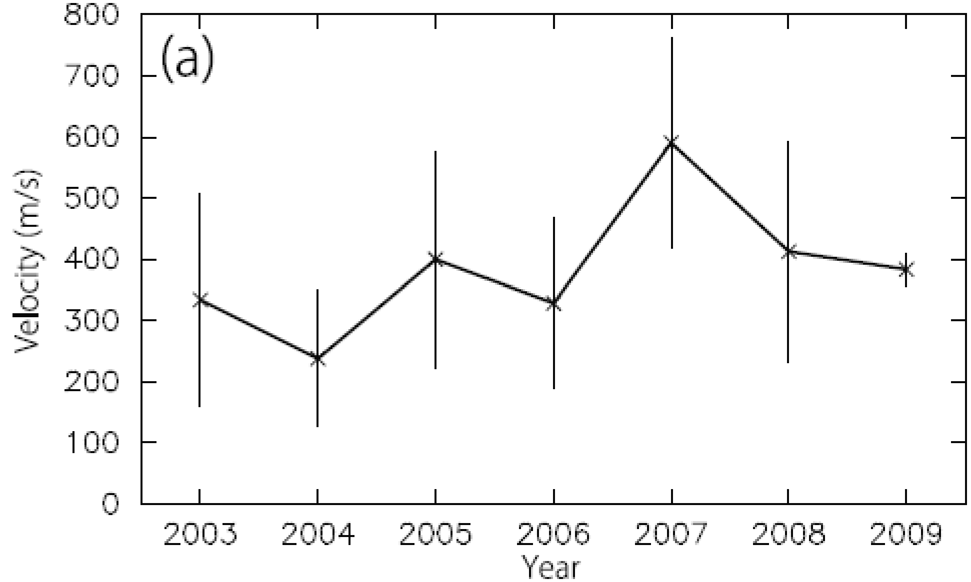

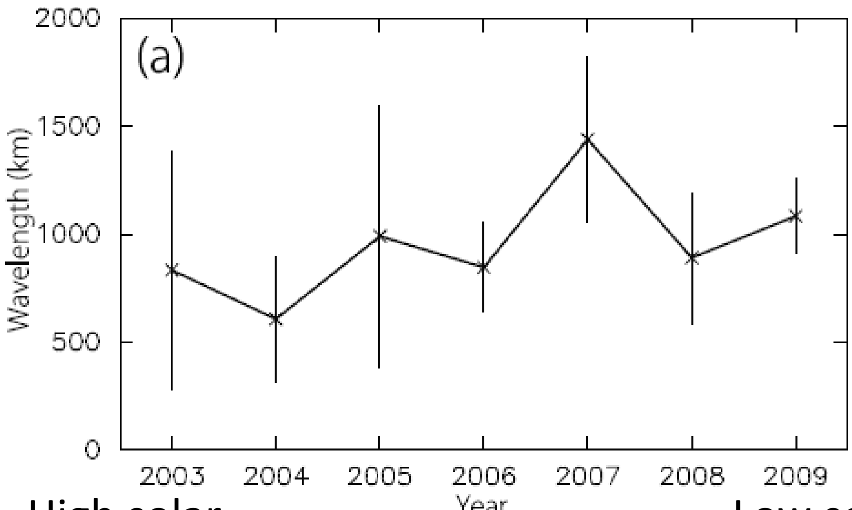

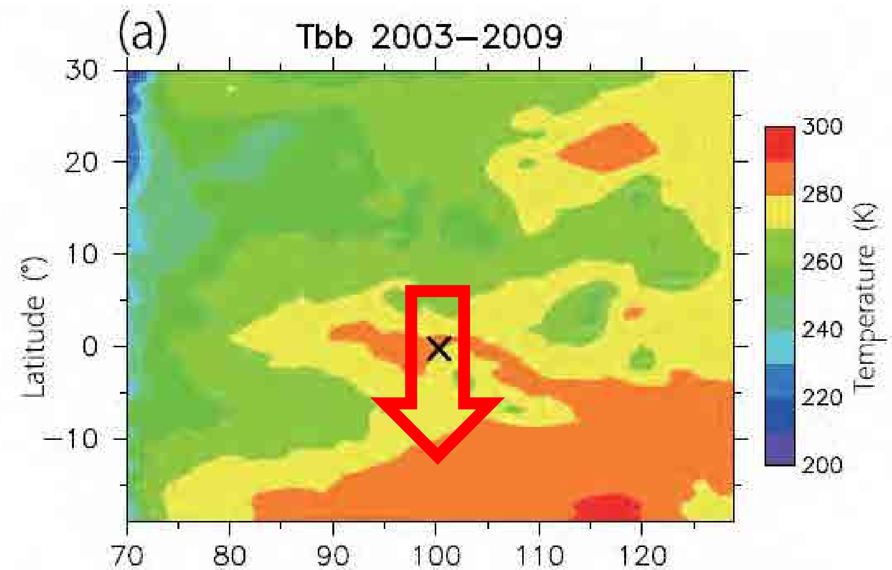

High solar activity

Low solar activity

Fukushima et al. (JGR, 2012)

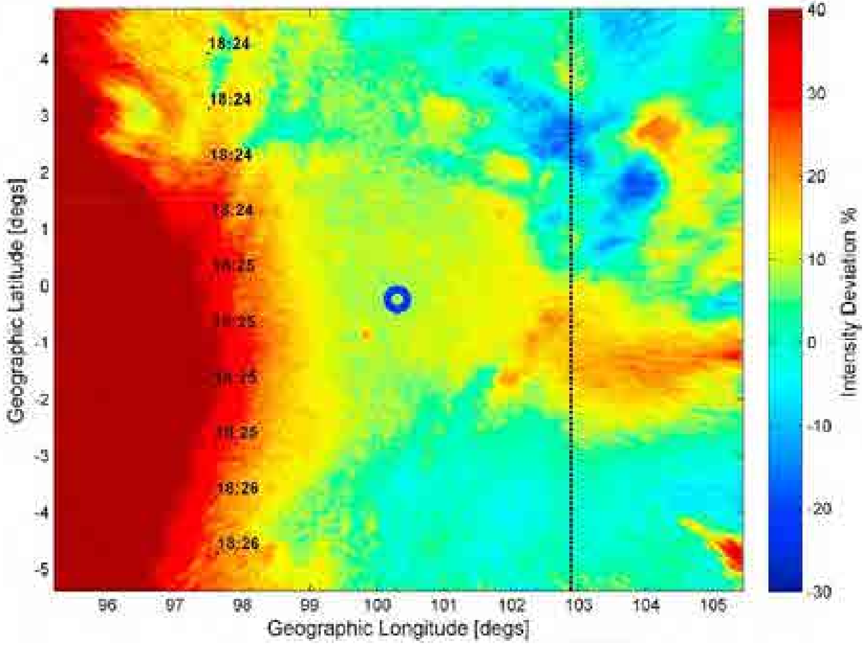

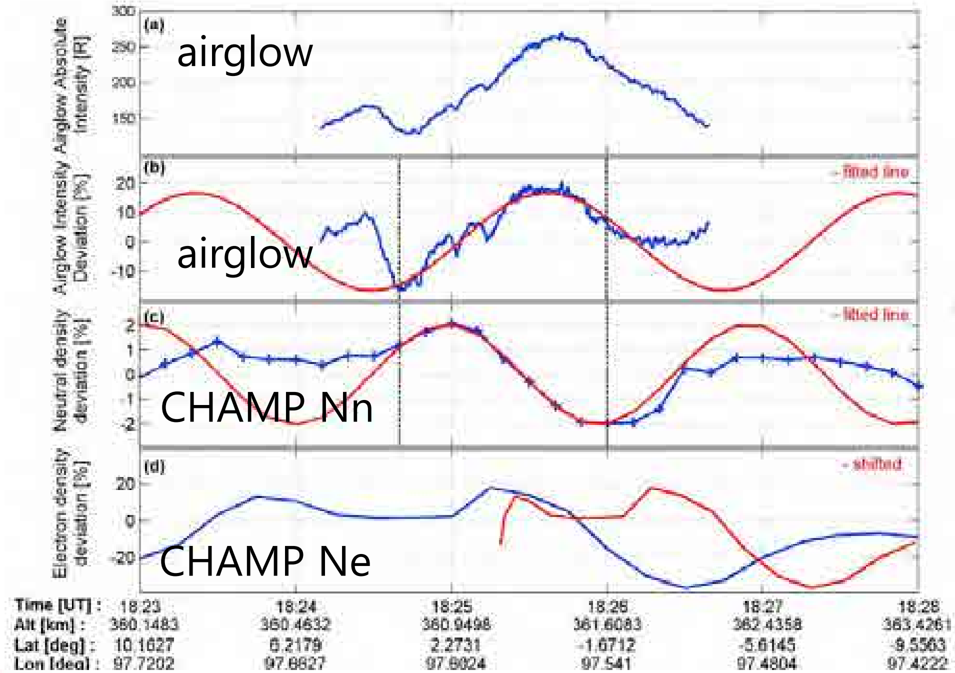

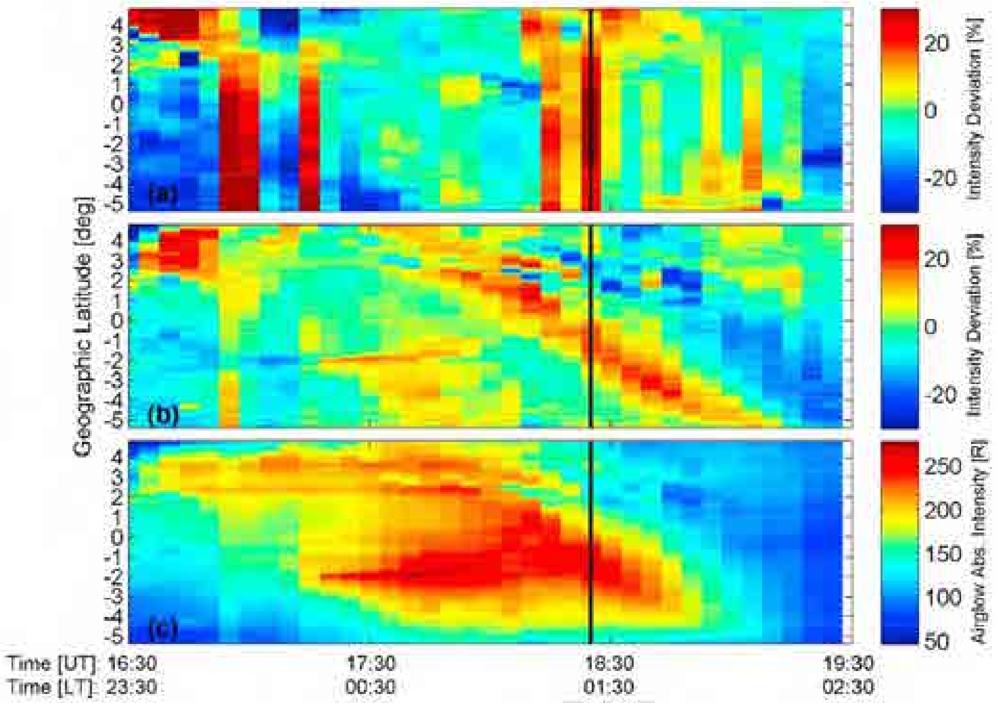

TID observation by airglow imager and CHAMP neutral density

Moral et al. (JGR, 2019)

Global distribution of nighttime MSTIDs - poleward side -

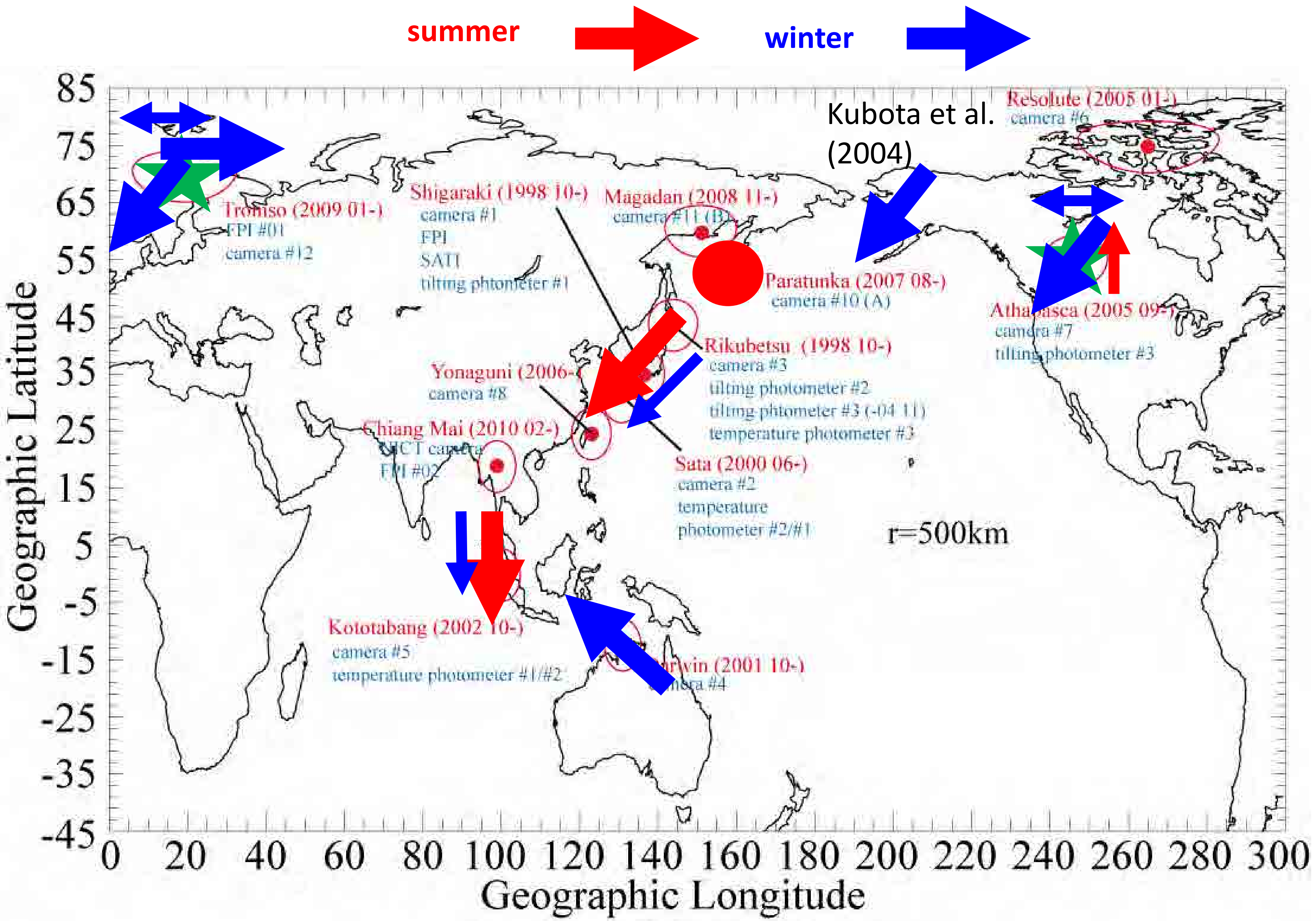

summer
winter
Kubota et al. (2004)
Resolute (2005 01-)
camera #6
Tromso (2009 01-)
FPI #01
camera #12
Shigaraki (1998 10-)
camera #1
FPI
SATI
tilting phtometer #1
Magadan (2008 11-)
camera #11 (B)
Paratunka (2007 08-)
camera #10 (A)
Athabasca (2005 09-)
camera #7
tilting photometer #3
Rikubetsu (1998 10-)
camera #3
tilting photometer #2
tilting phtometer #3 (-04 11)
temperature photometer #3
Yonaguni (2006-)
camera #8
Chiang Mai (2010 02-)
NICT camera
FPI #02
Sata (2000 06-)
camera #2
temperature photometer #2/#1
r=500km
Kototabang (2002 10-)
camera #5
temperature photometer #1/#2
Darwin (2001 10-)
camera #4
Geographic Latitude
Geographic Longitude

Aug.19, 2007
1010-1636UT
(1910-0236LT)

630nm (ch.2)

Paratunka,
Kamchatka

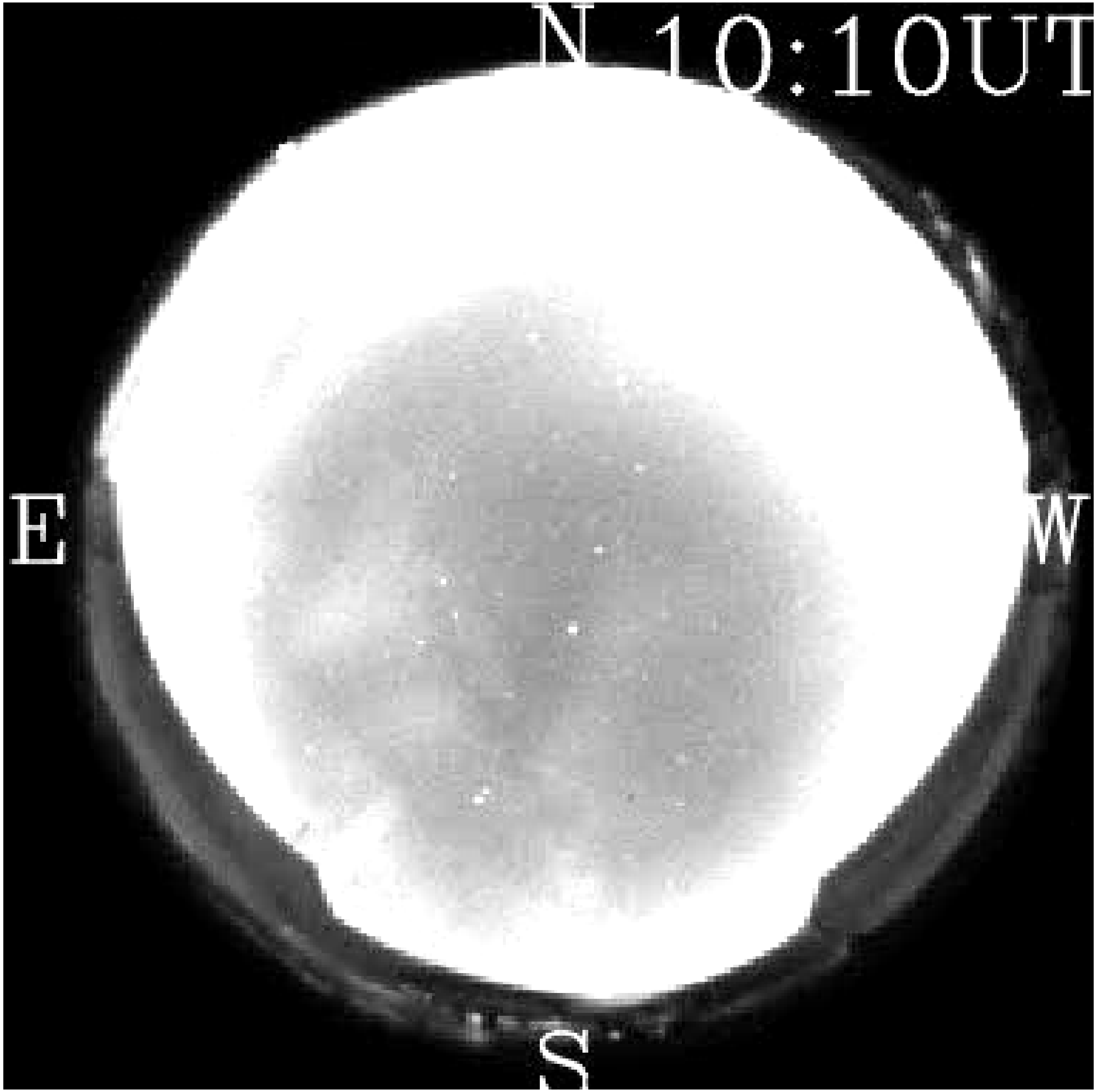

Shiokawa et al. (JGR, 2008)

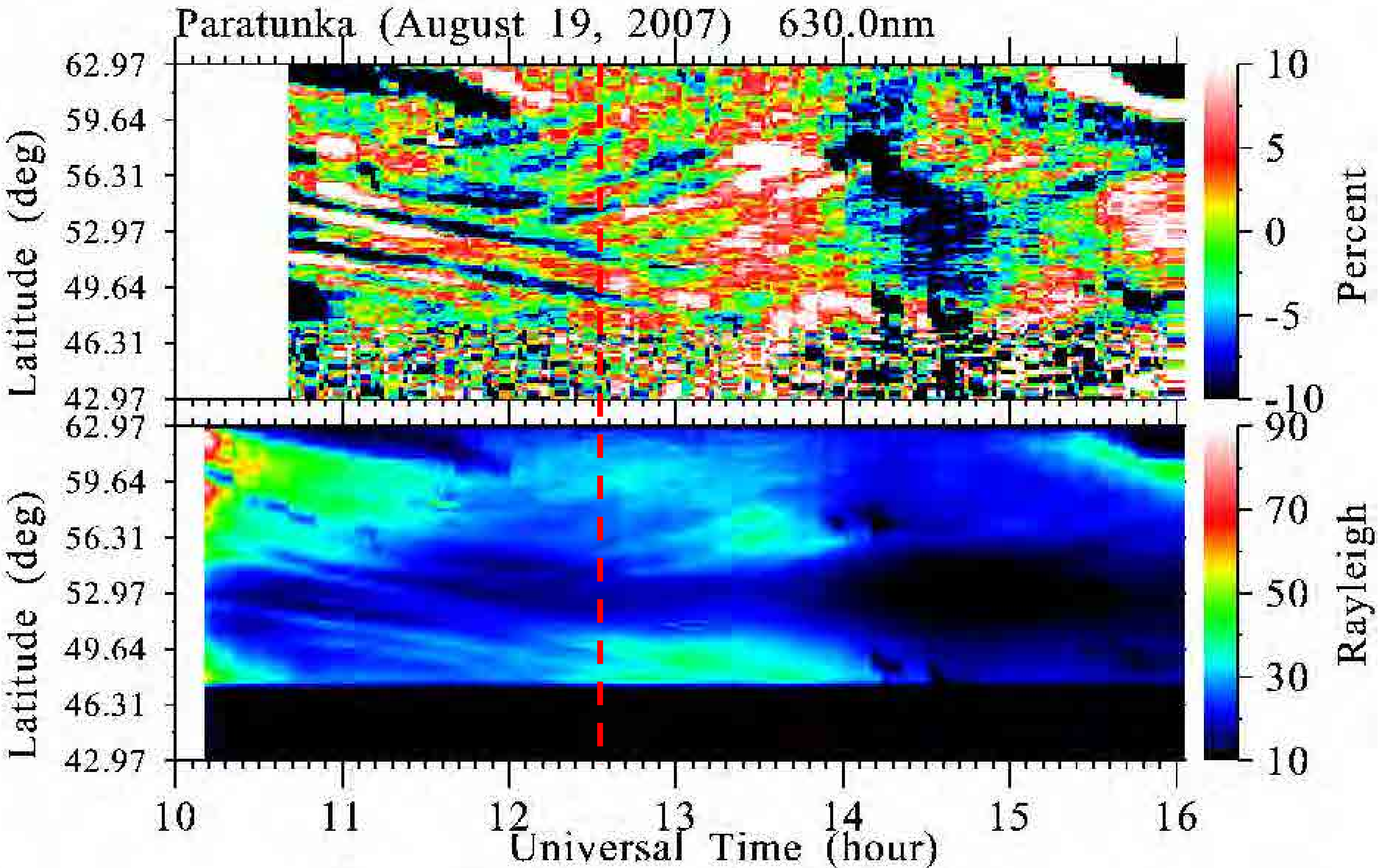

Shiokawa et al. (JGR, 2008)

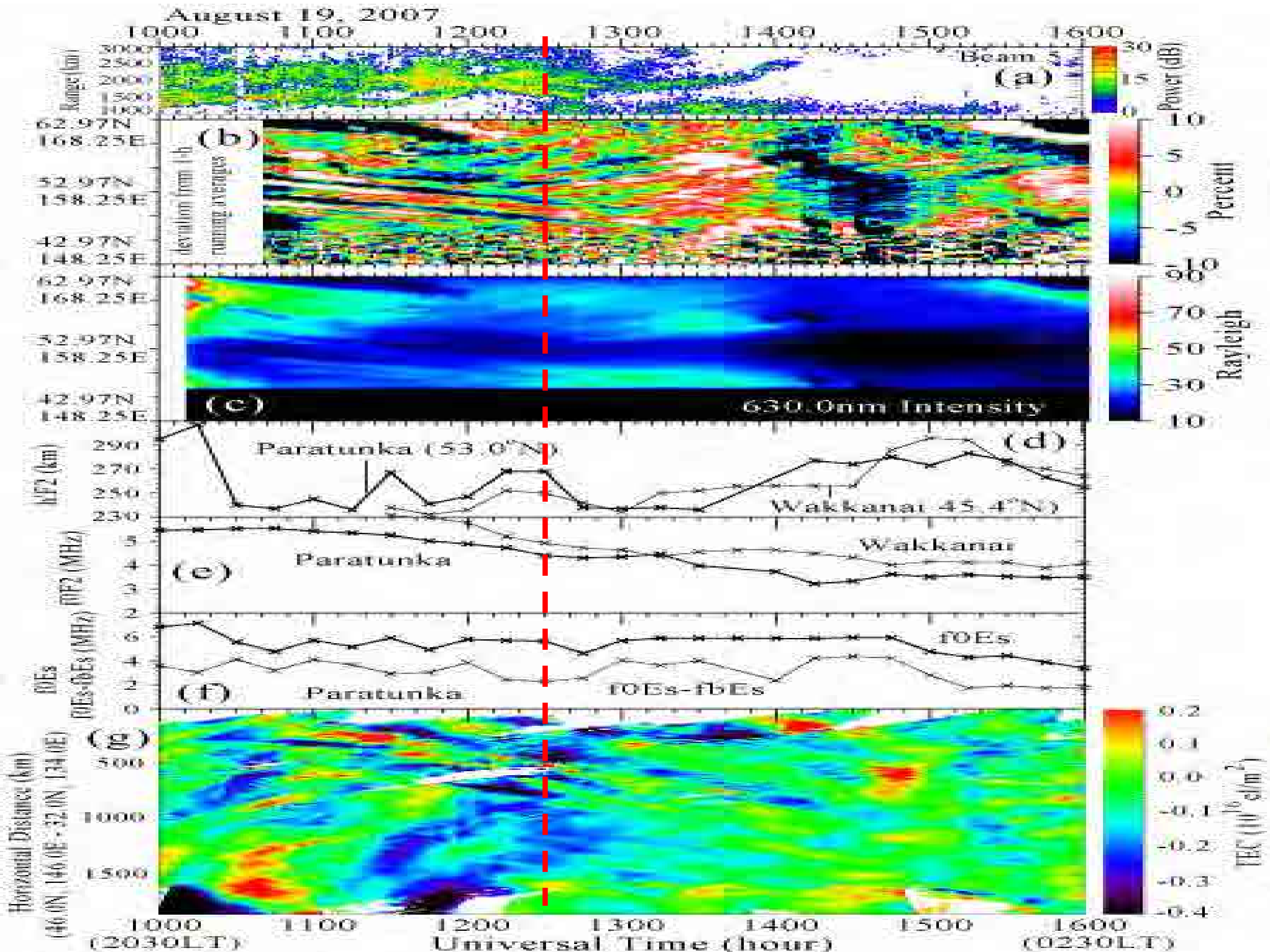

August 19, 2007
1000 1100 1200 1300 1400 1500 1600
Ranges (km)
Beam 5
(a)
Power (dB)
(b)
deviation from 1-h running averages
Percent
62.97N 168.25E
52.97N 158.25E
42.97N 148.25E
(c)
630.0nm Intensity
Rayleigh
hF2 (km)
Paratunka (53.0°N)
Wakkanai 45.4°N)
(d)
foF2 (MHz)
Paratunka
Wakkanai
(e)
fOEs fOEs-fbEs (MHz)
fOEs
Paratunka
fOEs-fbEs
(f)
(g)
Horizontal Distance (km) (46.0N, 146.0E - 32.0N, 134.0E)
TEC (10^16 el/m^2)
1000 (2030LT)
1600 (0230LT)
Universal Time (hour)

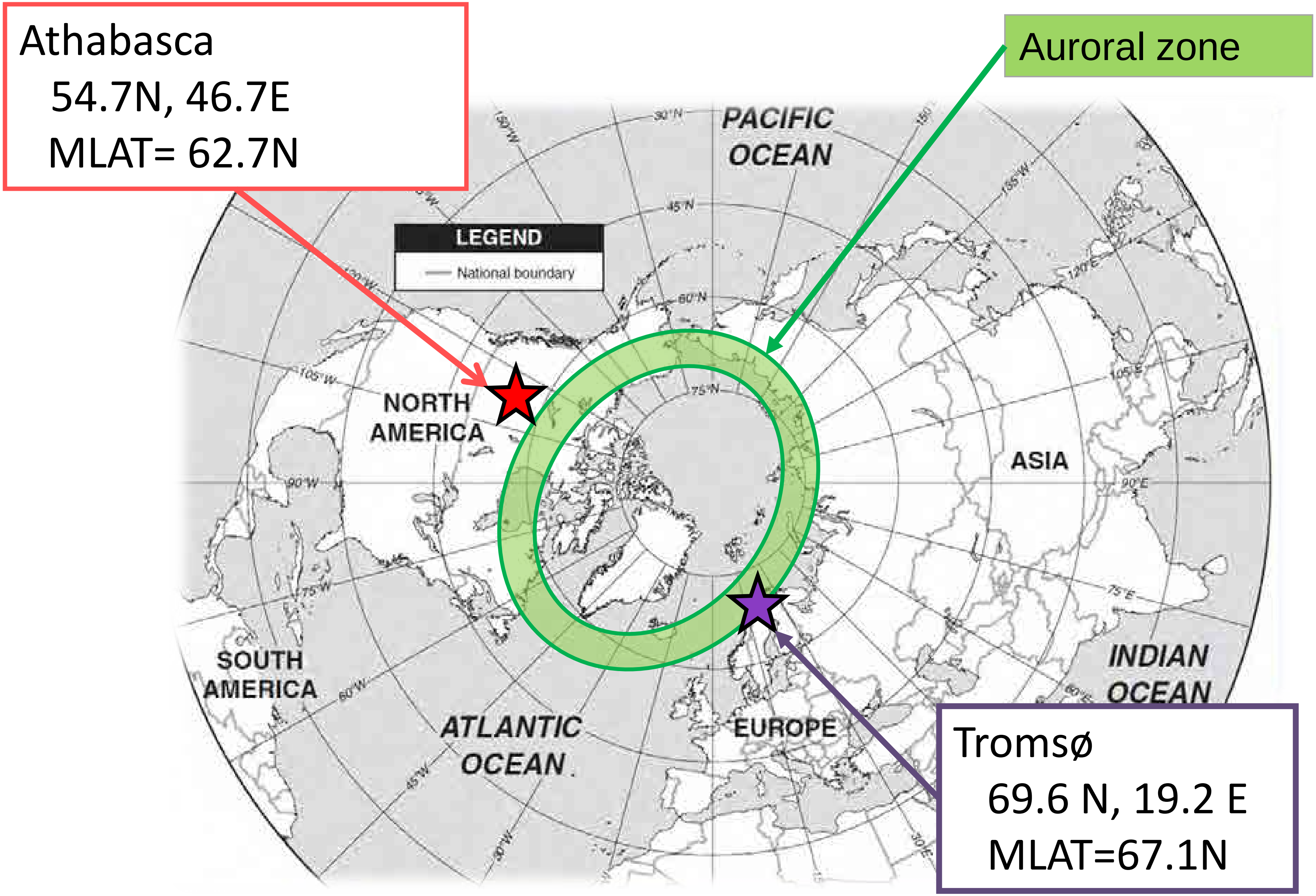

Athabasca
54.7N, 46.7E
MLAT= 62.7N
Auroral zone
PACIFIC OCEAN
LEGEND
National boundary
NORTH AMERICA
ASIA
SOUTH AMERICA
ATLANTIC OCEAN
EUROPE
INDIAN OCEAN
Tromsø
69.6 N, 19.2 E
MLAT=67.1N

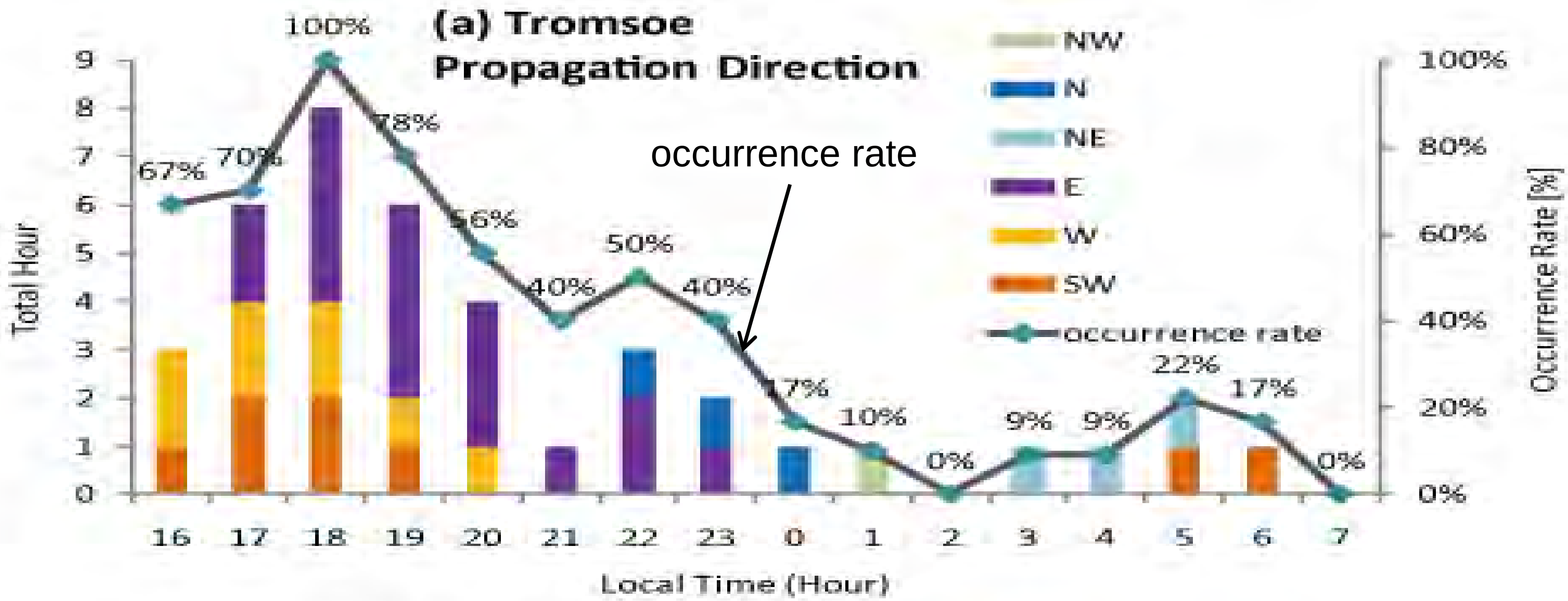

Half MSTIDs are SWward. The other half are eastward!

fossil after instability?

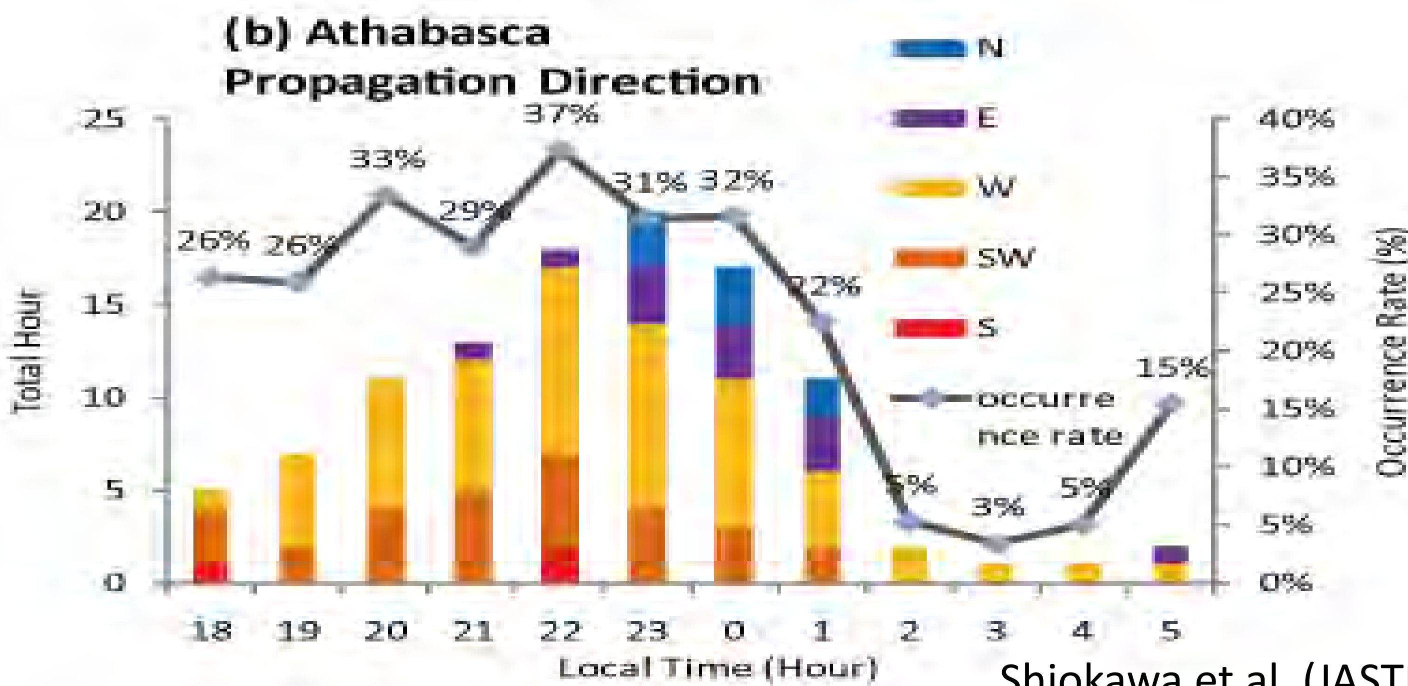

Shiokawa et al. (JASTP, 2013)

MSTID oscillation associated with auroral disturbance
December 8, 2009 15-19 UT (16-20LT)

- ✓NE-SW phase surface
- ✓Phase velocity： 42m/s, Wavelength: ~178km
- ✓Oscillation at 1730UT
- ✓Velocity at the oscillation can be 170m/s

Shiokawa et al. (JGR, 2012)

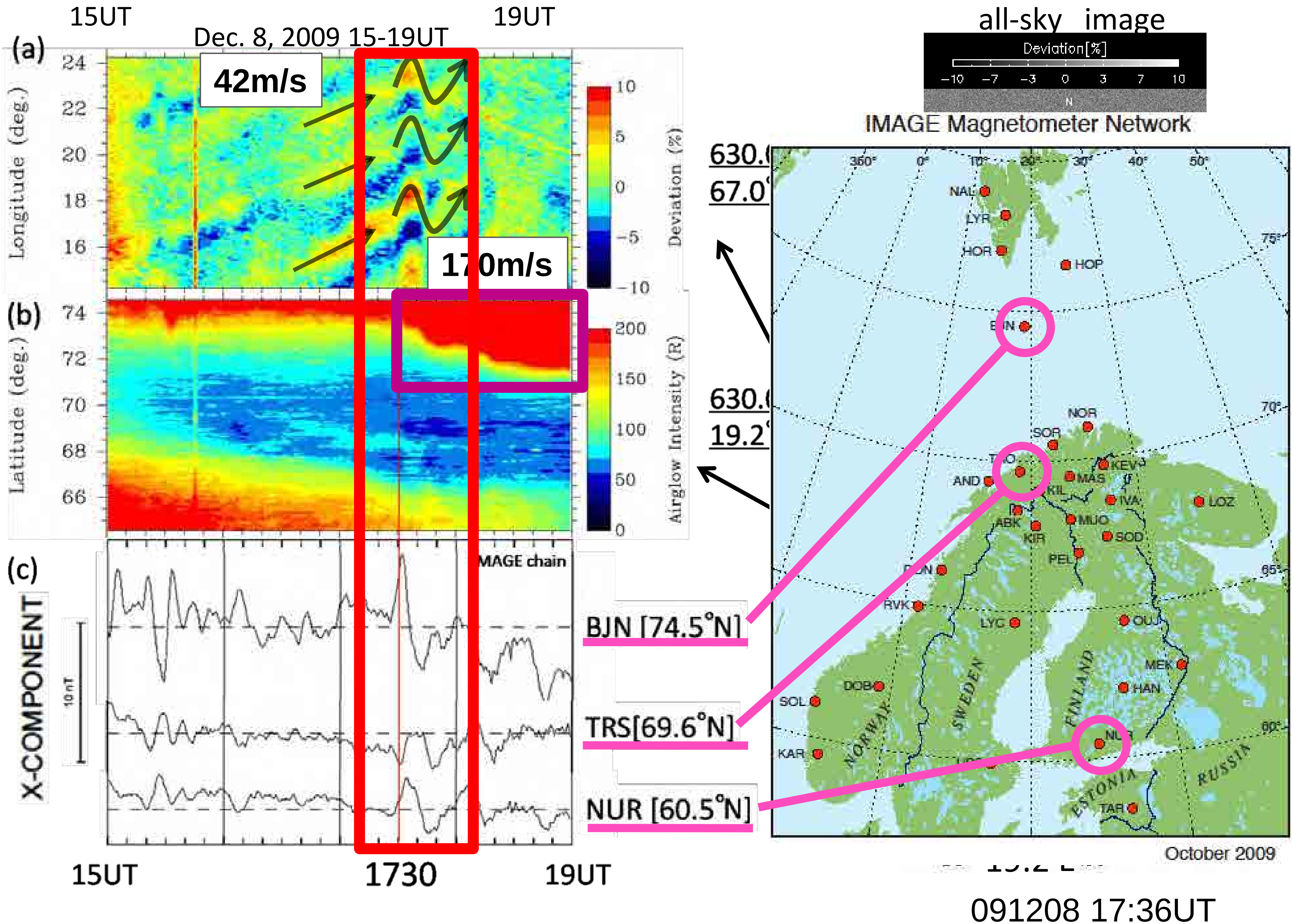

MSTID oscillation associated with auroral disturbance

Shiokawa et al. (JGR, 2012)

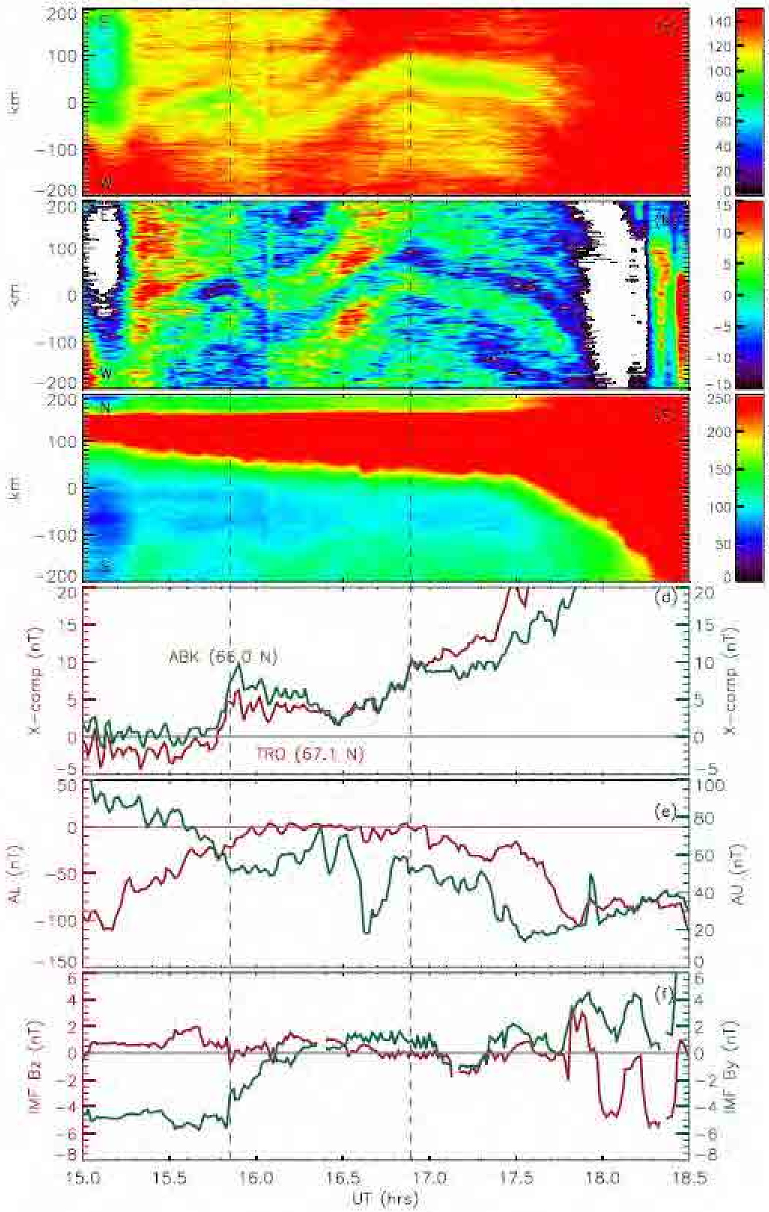

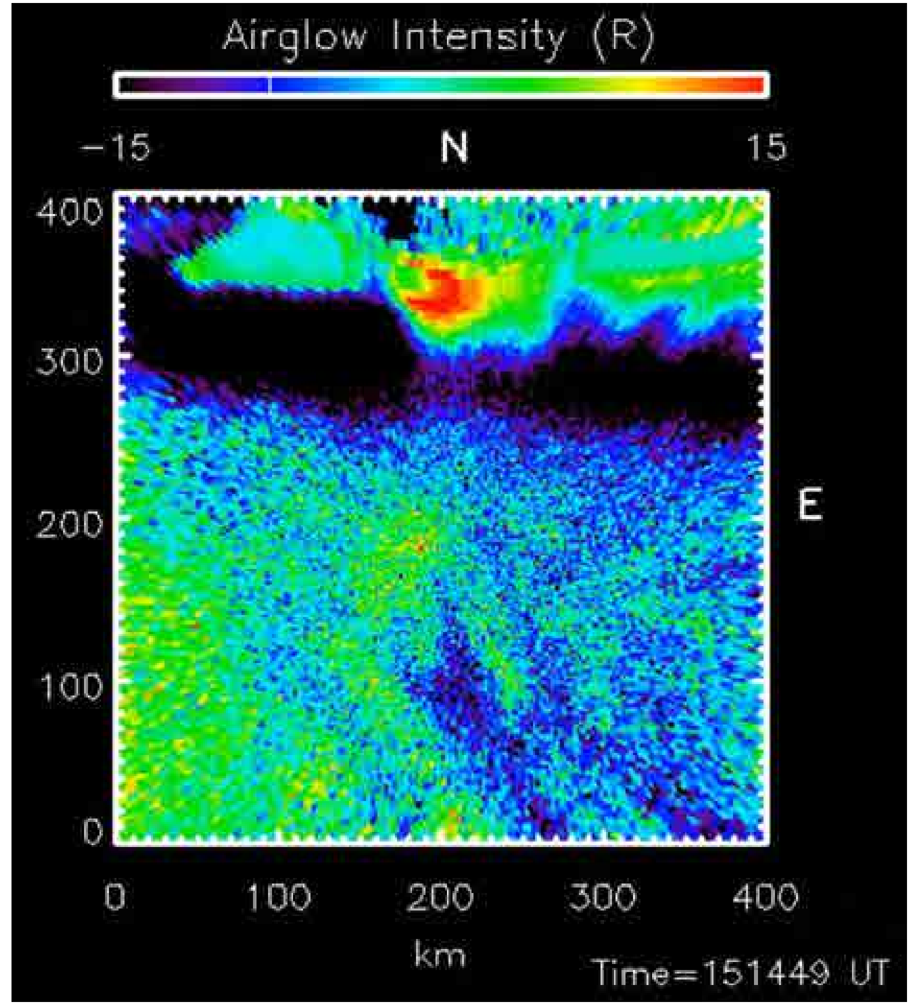

Multi-event analysis of oscillatory motion of medium-scale traveling ionospheric disturbances observed by a 630-nm airglow imager over Tromsoe (Yadav et al., JGR, 2020, https://doi.org/10.1029/2019JA027598).

Summary on MSTIDs

- Nighttime MSTIDs are a prevailing feature of the ionosphere at middle and subauroral latitudes at 20-60 MLAT.
- Nightime MSTIDs with NW-SE phase surface (northern hemisphere) is probably caused by E-F coupling and Perkins instability.
- Nighttime MSTIDs at middle latitudes seem to be bounded by the equatorial anomaly at the equatorial boundary (~10-20 MLAT).
- Nighttime MSTIDs observed near the equator (~10 MLAT) show gravity wave features, propagating away from the highly convective tropospheric region
- At subauroral latitudes, some nighttime MSTIDs show effect of penetrating electric field and gravity waves generated by auroral energy input.

--> Study to be continued.